AN ABSTRACT OF THE DISSERTATION OF

Aurélie J. Moulin for the degree of Doctor of Philosophy in
Ocean, Earth, and Atmospheric Sciences presented on March 25, 2016.
Title: Evolution of Turbulence, Heat Content, and Freshwater Lenses
in the Diurnal Warm Layer

Abstract approved: _____
James N. Moum Emily L. Shroyer

Thorough understanding of the mechanisms controlling the temperature structure in the surface mixed layer of the ocean and, in particular, accurate values of sea surface temperature are critical for properly parameterizing air-sea heat exchange and quantifying the amount of heat redistributed below the surface. It is however difficult to obtain routine in-situ measurements of the sea surface temperature from oceanographic moorings or research vessels, and even more difficult to measure the detailed evolution of the temperature structure. Oceanographers instead rely on parameterizations of a diurnal warm layer forced by temperature profiles or time series to estimate the time-varying surface temperature structure.

For the first time, the time-varying near-surface temperature structure, turbulence and surface heat fluxes were measured at the same time in the Indian Ocean during the DYNAMO field experiment. These measurements showed the abrupt termination of nighttime mixing at sunrise and subsequent decay during approximately one hour, they showed a rapid growth of turbulence thereafter as a balance of shear and buoyancy production and turbulent kinetic energy dissipation, and they showed an equilibrium state in the afternoon. Elevated turbulence were attributed to shear instabilities from the observation of temperature ramps in low-moderate wind conditions, but could not

be distinguished from Langmuir circulations in higher winds. Distinct relationships of the vertical temperature gradient, wind speed and turbulence dissipation emerged when classifying data by presence of temperature ramps.

These measurements also permitted a re-assessment of the vertical structure and physics of the diurnal warm layer with implications for heat budget assessment, therefore helping to identify weaknesses in current parameterizations. The shape of temperature profiles results from the ability of turbulence to export downward the heat deposited near the surface by exponentially attenuated subsurface solar radiation. When stratification was weak in the early morning surface heat was distributed over the top eight meters resulting in heat in excess of local solar radiation divergence. After complete restratification, surface heat was trapped above the mixed layer depth where it was both input from local divergence of the absorbed solar radiation and from the downwelling of surface heat through mixing. Below the mixed layer, the divergence of attenuated solar radiations was the only heat source.

Shear instabilities at the base of the mixed layer entrain cooler fluid from below thereby deepening the mixed layer depth and distributing heat and momentum over a thicker layer. In late afternoon when net surface cooling exceeded the net heating from the divergence of penetrating solar radiation, the temperature structure was destabilized from above, mixing heat downward. The heat accumulated over the previous hours and stored in the mixed layer was then eroded both from above through convection and from below through shear instabilities.

Our observations also permitted a detailed look at freshwater lenses deposited by strong localized precipitation, which can affect the heat content directly from the addition of cooler rainwater, but also indirectly by modifying the stratification of the upper ocean. Twenty-six lenses were identified, ten of which propagated at the internal wave speed and featured buoyant gravity current characteristics. The temperature and

salinity anomalies of lenses were related to their age and rain volume precipitated, and they were either cooler or warmer than ambient water. This propensity to retain heat created a patchy temperature environment both at the surface and in the near-surface as pockets of warm and cool water were observed within lenses. Thermohaline anomalies were estimated to dissipate in three days on average, but up to 25 days, if the turbulent mixing of ambient water was the only source of heat and salt.

Evolution of Turbulence, Heat Content, and Freshwater Lenses in the Diurnal Warm Layer

by

Aurélie J. Moulin

A DISSERTATION

submitted to

Oregon State University

in partial fulfillment of
the requirements for the
degree of

Doctor of Philosophy

Presented March 25, 2016
Commencement June 2016

Doctor of Philosophy dissertation of Aurélie J. Moulin presented on March 25, 2016

APPROVED:

Co-Major Professor, representing Ocean, Earth, and Atmospheric Sciences

---

Co-Major Professor, representing Ocean, Earth, and Atmospheric Sciences

---

Dean of the College of Earth, Ocean, and Atmospheric Sciences

---

Dean of the Graduate School

I understand that my dissertation will become part of the permanent collection of Oregon State University libraries. My signature below authorizes release of my dissertation to any reader upon request.

Aurélie J. Moulin, Author

ACKNOWLEDGEMENTS

Academic

What an enormous challenge to rightly express gratitude to those who helped turn a passion into a career. Jim Moum, my advisor for 7+ years, made it possible by patiently standing by as I tried, and failed, until the day I failed a little less. Beyond the meticulous and rigorous scientific method, beyond international hotel reservations and tourist visas debacles, I truly learned the meaning of utmost dedication. The experiences and learning opportunities he offered were beyond spectacular. I am thankful, fortunate, and humbled to have been part of his group which often felt just like a family.

I am equally indebted to Emily Shroyer, my co-advisor for the last 4 years. Emily's natural gift to turn the most arduous challenges and self doubts into curious possibilities eased the never-ending feelings of inadequacy. Always available, always calm and positive, always realistic, a true powerhouse and a formidable inspiration, she made me doubt less and less every week and empowered my abilities.

My committee members Ricardo Matano, Bill Smyth, and Eric Skyllingstad all provided valuable help and advice at opportune times contributing to the success of this thesis.

The Ocean Mixing Group is the family of individual geniuses that makes piercing turbulence secrets possible. Sasha Perlin with his sometimes necessary and often comical bluntness provided much needed guidance and aspirations. Ray Kreth' legacy in the building and deployment of instruments used in my thesis was incommensurable. Craig Van Appledorn was always very discreet from his 6'4" (+?) but incredibly funny and unmistakably available to help accomplish any mission (Party on Wayne). Martín Hoecker-Martínez, provided bottomless help throughout the years from homeworks to research ideas. Mike Neeley-Brown, Pavan Vukutur, Sally Warner, and Kandaga Pujiana made data collection and processing possible.

Personal

To the family that stuck by me through ebbs and flows, floods and droughts, and the occasional tsunami or beach party, Thank You.

First, to my parents. They're awesome. I thought they were just ok for a while, probably about the first 20 years of my life. Then I realized they were actually pretty outstanding (C'est pas faux). Merci de votre soutien permanent, constant, et sans équivoque. Then to my brother Sébastien who provided numerous laughs and face-palms (Seb, c'est bien). Finally my uncle Michel and grandma Manou who always believed in me and never asked why I wasn't done with this already.

To Neptune, my blue Doberman buddy of 8 years who kept me loved, entertained, and frustrated any given day. Always faithful. Always wagging. Always by my side.

To my brothers and sisters from other mothers, they all brightened my days with their smiles, their jokes, their hugs, and their hearts. Rachel Crowhurst kept me sane, happy, highly entertained and everything in between over the years and for that I shall guard and protect her heart forever; Carole Berini, my partner in crime through college and beyond, and Géraldine Jacob, my friend of 23 years and mother of my godson Alexandre, were my rocks in any circumstances; Suzanna Stoike, my travel and shenanigans sister, provided hugs, wine, infinite laughters, reason, appreciation and a few liferings; Yvan and Ariene Alleau endured my laughs and my tears with attention and generosity; and Peter Gaube tried to protect my soul from my impulsive and terrible ideas and was always there to pickup the pieces. You are all family.

And to the individuals who inspired, supported, and comforted me, Angela Rowe, Langley DeWitt, Kate Adams, and Shera Eshmade my role and soul models, Derek Coffman and Randy Zúñiga. An honorable mention goes to MacGyver, Beethoven, Björnson Vineyard, Central America, and Jacques Cousteau. Thank you all for making me feel relevant.

TABLE OF CONTENTS

TABLE OF CONTENTS (Continued)

TABLE OF CONTENTS (Continued)

TABLE OF CONTENTS (Continued)

TABLE OF CONTENTS (Continued)

LIST OF FIGURES

LIST OF FIGURES (Continued)

LIST OF TABLES

EVOLUTION OF TURBULENCE, HEAT CONTENT, AND FRESHWATER LENSES IN THE DIURNAL WARM LAYER

1. OVERVIEW OF CONTEXT AND MOTIVATIONS

1.1. Introduction

The equatorial open ocean is a fascinating blend of large scale zonal currents and vertical gradients of heat, salt, and momentum. It is a tremendously dynamic environment from synoptic to micro scales. El Niño, one of the most familiar equatorial phenomenon, exhibits a signature spanning the entire Pacific zonal extent with teleconnections worldwide (McPhaden et al., 2006), from maize yield in Uruguay (Baethgen et al., 2009) to wine quality in Spain (Rodó and Comín, 2000). The Madden-Julian Oscillation (MJO) is lesser known but also has repercussions worldwide (Zhang, 2013; Giannini et al., 2001). This eastward traveling atmospheric disturbance intensifies over the central equatorial Indian Ocean and affects precipitation patterns over the entire Indian Ocean basin and western Pacific (Donald et al., 2006) and as far as the American Pacific Northwest (Bond and Vecchi, 2003). The reliance of portions of southern Asia on subsistence agriculture brings greater significance to the physical understanding of changes in precipitations patterns (Dewar, 2003; Morton, 2007).

At the other end of the scale spectrum small scale mixing processes distort fluid, stretch contact surfaces between parcels or layers of water of different density, thereby increasing the potential for molecular diffusion. This nestling of infinitely smaller scales down to molecularly relevant scales, where heat, salt, and momentum are dissipated,

follows an energy cascade first described by Richardson (1920).

If we ignore the minute sources of heat or freshwater from bottom boundaries, the atmosphere is the main driving force in the open ocean. Air-sea interactions alter surface water properties and constantly sustain exchanges of heat and freshwater (sources or sinks) with the atmosphere (Wang and Xie, 1998). The energy thus gained by the atmosphere and modulated by sea surface temperature fuels storms, small or large, with important consequences for populations downstream. This dissertation aims at contributing to our understanding of upper ocean processes by detailing the small scale details of controls on the sea surface temperature.

1.2. Air-sea interaction in the Equatorial Indian Ocean

The Indian Ocean is often described as an oddity: its land boundary to the North limits the exchange of water with other basins. Unlike the Atlantic or Pacific oceans, the Indian ocean is warmer to the east than to the west in the equatorial band and features no cold tongue. Here we describe air-sea interaction phenomenon on global and basin scales which originate in the Indian Ocean.

1.2.1 Basin scale: Monsoon circulation and Indian Ocean Dipole

The equatorial current system is modulated by the annual Monsoons, often described in terms of the north - south meanders in the intertropical convergence zone. During summer, the scorching heat over the Indian subcontinent enhances atmospheric convection thus driving sustained south-westerly. The warm and humid air mass generates about 70% of India's annual precipitation as it hits the Himalayas, rises, and condenses into rainfall. During this time the South Equatorial Counter-Current (SECC) and the

Southwest Monsoon Current (SMC) straddling the equator both flow east. In winter, when the ocean is warmer than the landmass to the north, the winds are predominantly north-easterly. The SECC is unaffected but the SMC flows westward and becomes the Northwest Monsoon Current. In between these two regimes, twice a year, Wyrtki jets (Wyrtki, 1973) carry warm surface water eastward, a result from the seasonal westerly winds.

The equatorial Indian Ocean is typically warmer offshore Indonesia than it is offshore Africa which implies a prevalence of convective storms in the east compared to the west of the ocean basin. The thicker and warmer upper ocean in the east is a result of the eastward transport of warm water by Wyrtki jets. Trade winds are typically mild and from the west (Schott and McCreary, 2001), and the thermocline leveled. But some years anomalous easterly Trades shoal the thermocline off Sumatra, producing a cold sea surface temperature anomaly and damping atmospheric convection (Vinayachandran et al., 2009).

The western equatorial Indian Ocean sees a positive sea surface temperature anomaly with increased atmospheric convection. This see-saw pattern in zonal equatorial temperature is commonly called the Indian Ocean Dipole (IOD). There is a marked tendency for droughts in Indonesia and flooding in eastern Africa during years featuring IOD characteristics (Saji et al., 1999).

1.2.2 Global scale: Madden-Julian Oscillation

The Madden-Julian Oscillation (MJO, Madden and Julian (1971, 1972)) is an atmospheric disturbance propagating eastward around the globe in the equatorial regions. It is thought to initialize over the African continent and intensify over the Indian Ocean where it encounters warmer water and generates heavy precipitations over the Maritime continent and western Pacific Oceans. Then, weakened by cooler sea surface temperature in the eastern Pacific ocean, the MJO somewhat vanishes over the South American

continent. MJOs circle the globe in 30 - 90 days (Zhang, 2005) and are associated with wind bursts, decreased outgoing longwave radiations due to increased cloud cover, and increased precipitations from deep convection.

They affect local rainfall from the Maritime continent to the Americas and Africa, affect the formation of tropical cyclones as far away as the Caribbeans and also affect winds in the equatorial Atlantic (Zhang, 2005). They are organized with a zone of deep atmospheric convection surrounded by areas of intense insolation, weak winds and weak convection. Although they occur in successions, there is only one disturbance present on the globe at any one time. Because of its ability to affect a large array of spatial and temporal scales, the MJO is a unique phenomenon bridging weather and climate (Zhang, 2013).

1.3. Dynamics of the Madden-Julian Oscillation Field Experiment - DYNAMO

The DYNAMO field campaign took place during the boreal fall of 2011 with the particular goal to collect observations of the MJO convective initiation processes (Gottschalck et al., 2013). In particular, the feedback between the atmosphere and ocean remain unknown (Moum et al., 2014). DYNAMO was motivated by three hypotheses (Yoneyama et al., 2013):

- "Hypothesis I: Deep convection can be organized into an MJO convective envelope only when the lower-tropospheric moist layer has become sufficiently deep over a region of the MJO scale; the pace at which this moistening occurs determines the duration of the pre-onset stage.

- Hypothesis II: Specific convective populations at different stages are essential for MJO initiation.

- Hypothesis III: The barrier layer, wind- and shear-driven mixing, shallow thermocline, and mixing layer entrainment all play essential roles in MJO initiation over the Indian Ocean by controlling the upper ocean heat content and sea surface temperature and thereby surface flux feedback."

Hypothesis III is the motivation behind the present work. A complete description of the scope of DYNAMO is provided in Yoneyama et al. (2013).

1.4. Motivation

Reconciling the heat budget is key to tracking the fate of the oceanic heat content. Heat deposited at the ocean's surface by the sun may be mixed deep in the ocean's interior, may linger relatively close to the surface, or may return to the atmosphere through air-sea interactions. The one-dimensional heat content is expressed as

$$\rho C_p \int \frac{\partial T}{\partial t} dz = J_q^0 - I_h - J_q^h \tag{1.1}$$

where ρ is water density (kg m^{-3}), C_p the heat capacity of sea water (J kg^{-1} ℃$^{-1}$), J_q^0 the net surface heat flux (W m^{-2}), I_h the absorbed solar radiation (W m^{-2}), and J_q^h the turbulent heat flux (W m^{-2}).

The net surface heat flux is a balance between the downwelling shortwave and longwave solar radiations, against the latent, sensible, and radiative cooling fluxes. A portion of the radiation hitting the surface, the albedo, is reflected to the atmosphere. The remaining absorbed solar radiation (ASR) follows an exponential profile governed by the transmission of solar radiation. Lastly, the turbulent heat flux is the result of turbulent mixing working to dissipate heat.

These elements are known to various degrees of accuracy. Incoming solar radiation and net surface cooling are deemed accurate, and so is the measured heat content since

it relies on direct observations. One-dimensional heat budgets ignore lateral advection, a residual source of error thought to be small over the time scales of observations. Two terms are known to be inaccurate, leading to a path toward improved understanding and parameterizations. The profile of solar attenuation is difficult to measure, especially in the top five meters (C. Ohlmann, pers. communication). Yet this is the depth range where 50% of shortwave radiation is absorbed. Studies have shown the impact of subtle variations in albedo and attenuation (Ohlmann et al., 2000; Lewis et al., 1990). But this is out of the scope of this dissertation. What we can address however is the turbulent heat flux by measuring and understanding the daytime cycle of turbulence near the surface. Heat content is also affected by salt stratification. Storms in the tropics are known to deposit large quantities of freshwater thus affecting the density structure. Storms are also patchy, generating scattered parcels of rainwater commonly termed freshwater lenses.

The specific questions addressed in this work are

- what is the daily cycle of turbulence in the upper 10 meters of the ocean?
- what controls the spatial and temporal evolution of the temperature structure in the upper 10 meters? and,
- what do freshwater lenses look like, how do they evolve, what is their heat and freshwater budget?

2. DATA AND METHODS

2.1. Indian Ocean data

Data were gathered during the Dynamics of the Madden-Julian Oscillation (DYNAMO) experiment in the equatorial Indian Ocean using the R/V Roger Revelle as a stationary platform at 80°E over two separate cruises, 08 - 26 October 2011 and 12 - 24 November 2011 (Figure 2.1). Each deployment is referred to as Leg2 and Leg3, respectively, after the phases of the DYNAMO intense observation periods. Local time was GMT+6.

2.1.1 In-situ oceanic and atmospheric data

A conductivity - temperature chain (T-chain) deployed at the bow of the ship was equipped with 10 units distributed between 1.5 - 7.5 meters depth (Table 2.1, Figure 2.2). The T-chain was weighted to remain taught and vertical (Figure 2.3). Two SBE-11 CTDs sampling at 3-second were deployed at an average depth of 4.2 and 7.5 m and measured temperature (T4.2, T7.5), salinity (S4.2, S7.5), density (R4.2, R7.5) and pressure. The remaining eight units were FP07 fast thermistors (Tpods) sampling temperature at 10 Hz and spread in between the surface and the CTDs (T1.5, T2.0, T2.5, T3.1, T4.7, T5.4, T6.0, and T6.6). This set-up provided high resolution measurement of the incoming, undisturbed flow as the ship was stationary and pointing into the eastward-flowing Southern Equatorial Current, with a mean speed of 0.8 m s^{-1}. An additional thermistor (T0.1) floating at $\backsim$0.10 m alongside the ship recorded sea surface temperature averaged at 1-min. Temperature (T_0), salinity (S_0) and density (ρ_0) were also measured by the ship's flow-through thermosalinograph representing an integrated measurement from the surface to the intake depth around 3 m.

Profiles of temperature, salinity, density, and shear microstructure were collected

using the free-falling Chameleon profiler (Moum, 1990) down to 200 m, every $\backsim$10 minutes. The upper 5 to 10 meters of profiles were in the ship's wake since the profiler was deployed from the stern (Figure 2.6). The addition of the bow T-chain therefore provided a complete temperature profile from the surface to 200 m when combined with Chameleon profiles. The current velocity was measured from the ship's ADCP and the top two bins (12-16 m) were averaged as an estimate for the surface current.

Short- and long-wave radiation, wind velocity, heat fluxes, and standard meteorological observations were measured on a mast located at the bow (Figure 2.3).

2.1.2 Remotely sensed data

Surface convergent features could be observed using X-Band radar images of 15-second averages of sea surface roughness. Series of radar frames (examples on Figure 2.2) were used to track propagating fronts (Appendix A), estimate propagation speed, identify arrival time at the R/V Revelle, and collocate with the arrival of salinity anomalies. These images are used in Section 5..

Precipitations were measured via a C-Band Doppler radar in a 150 km radius around the ship with a blanking distance of 2.0 km. They are gridded (2-km resolution) and averaged to estimate the hourly accumulation of precipitation. These hourly maps were combined with ocean velocity to infer the precipitation history of parcels of water passing by the ship (Appendix B).

2.2. Complementary Pacific Ocean data

Data were also sourced from an experiment in the equatorial Pacific Ocean (EQ14, Figure 2.4) with similar meteorological measurements but with slightly different T-chain configurations (Table 2.1, Figure 2.5). EQ14 took place from 15 November - 03 December

2014 at 110°W onboard the R/V Oceanus. For this experiment the ship maintained a slow, constant speed faster than the current velocity so as to measure the diurnal warm layer structure before it was disrupted by the ship. The core difference between the DYNAMO and EQ14 datasets lies in the water column overall structure. DYNAMO was an alternation of strong diurnal warming with weak winds and stormy conditions. EQ14 featured windier conditions with a weak upper layer temperature gradient. Together, these sets offer a large dynamic range of conditions to test the validity of our methods to derive temperature gradients and mixing estimates from bow-thermistor chains. Local time was GMT-7 and to easily compare the DYNAMO and EQ14 datasets, EQ14 was time-translated to GMT+6.

2.3. Motivation for thermistor chain deployments and Calibration of temperature sensors

The unsuitability of tethered profilers for measuring the detailed structure of the upper ocean by fantail deployment during the day is highlighted on Figure 2.7. The diurnal warm layer during intense insolation and low winds can be as shallow as 1 meter and have a sharp thermocline at its base. This feature is annihilated by the ship's wake, rendering Chameleon profiler measurements inaccurate in the upper water column due to their fantail deployment. The R/Vs Roger Revelle and Oceanus both having a draft of approximately 5.3 m, Chameleon data above 6 m are distorted. The T-chain provided a unique time series of the diurnal warm layer evolution.

Constant offsets were applied to individual thermistors in order to ensure sensor biases did not influence temperature gradient estimates. These offsets were calculated using time periods during each deployment when the upper water column was determined to be well-mixed with temperature difference between selected sensors $<| 0.0007 |$ °C. For DYNAMO (EQ14) deployments, all SBE37 (RBR Solo) sensors were used to determine

well-mixed time periods. Offsets were calculated and applied for each instrument during each deployment independently. An offset was similarly calculated and applied to T0.1.

2.4. Derivation of temperature gradient from discrete locations

Mixing estimates are sensitive to the accuracy of the vertical temperature gradient. (This can be compared to the resolution limiting the calculation of gradients for a single profiling sensor.) Even after calibration with constant offsets, biases of individual sensors limited the quality of the temperature gradient estimates, particularly at times of weak stratification. To remove biases in accuracy between sensors, observed temperature profiles were regressed onto a profile obtained by solving the heat equation with the following initial and boundary conditions:

$$\frac{dT}{dt} = \alpha \frac{\partial^2 T}{\partial z^2} + \frac{\eta(1-\beta)}{\rho C_p}\ \phi_o\ e^{-\eta z} \tag{2.1}$$

$$\rho C_p \alpha \frac{dT(0,t)}{dt} = \beta \phi_o (1 - \frac{\phi_L}{\beta \phi_o}) \tag{2.2}$$

$$T(z,0) = 0; \tag{2.3}$$

where the second term on the right hand side of equation (2.1) is the penetrating sunlight heat source, (2.2) is the surface heat source, and where

α : temperature diffusivity, $\mathrm{m}^2\ \mathrm{s}^{-1}$,

η : absorption coefficient,

β : albedo,

ρ : density, $\mathrm{kg\ m}^{-3}$,

C_p : thermal capacity of sea water, J ℃$^{-1}$ kg^{-1},

ϕ_o : net surface heating, W m^{-2}, > 0, and

ϕ_L : net surface cooling, W m^{-2}, < 0.

The complete solution of this boundary value problem with surface heat flux and internal heating is

$$
\begin{aligned}
T = T_0 &+ \frac{2\beta\phi_o}{\rho C_p \alpha\sqrt{\pi)}} \left(\frac{\sqrt{\pi}}{2} \left(\frac{\alpha}{\omega}\right)^{1/2} e^{-z\left(\frac{\omega}{2\alpha}\right)^{1/2}} sin\left(\omega t - \frac{\pi}{4} - z\left(\frac{\omega}{2\alpha}\right)^{1/2}\right)\right) \\
&- \frac{2\beta\phi_o}{\rho C_p \alpha\sqrt{\pi}} \left(\left(\frac{\alpha}{\omega}\right)^{1/2} \sum_{n=1}^{\infty} e^{-z\left(\frac{n\omega}{2\alpha}\right)^{1/2}} sin\left(n\omega t - \frac{\pi}{4} - z\left(\frac{n\omega}{2\alpha}\right)^{1/2}\right) \frac{1}{\sqrt{n}(4n^2-1)}\right) \\
&- \frac{\phi_L}{\rho C_p \alpha}\, erfc\left(\frac{z}{2\sqrt{\alpha t}}\right) \\
&+ \frac{A_o}{\left(\eta^4 + \frac{\omega^2}{\alpha^2}\right)^{1/2}}\, e^{-(\eta z)}\, sin(\omega t + \theta) \\
&+ \frac{A_o}{\left(\eta^4 + \frac{\omega^2}{\alpha^2}\right)^{1/2}}\, e^{-z\left(\frac{\omega}{2\alpha}\right)^{1/2}} sin\left(\omega t - z\left(\frac{\omega}{2\alpha}\right)^{1/2}\right) \\
&- \frac{2A_o}{\sqrt{\pi}\left(\eta^4 + \frac{\omega^2}{\alpha^2}\right)^{1/2}} \sum_{n=1}^{\infty} \left(\frac{\alpha}{\omega}\right)^{1/2} \frac{e^{-z\left(\frac{n\omega}{2\alpha}\right)^{1/2}}}{\sqrt{n}}\, sin\left(n\omega t - z\left(\frac{n\omega}{2\alpha}\right)^{1/2}\right) \frac{1}{4n^2-1} \\
&- \frac{2A_o\, sin(\theta)}{\pi\left(\eta^4 + \frac{\omega^2}{\alpha^2}\right)^{1/2}} \int_0^{\infty} \frac{\lambda}{\eta^2 + \lambda^2}\, sin(\lambda z)\, e^{-\lambda^2 \alpha t} d\lambda
\end{aligned}
\tag{2.4}
$$

where $A_o = \dfrac{\eta(1-\beta)\phi_o}{\rho C_p \alpha}$, $\theta = atan\left(\dfrac{\omega}{\eta^2\alpha}\right)$, and λ is a dummy variable.

The three terms we were interested in to represent the subsurface temperature structure were the surface heating, internal heating from penetrating sunlight, and cooling from above. Equation (2.4) gave the exact contribution of each of these components to

a profile and therefore we aim at using a combination of the simplest form of these three terms to fit to the observations. The following model, based solely on surface and internal heating, was then used to non-linearly fit the data:

$$T_{heq}(z) = \beta_5 + \beta_1 e^{-z\sqrt{\frac{\omega}{2\beta_2}}} + \beta_3 e^{-\beta_4 z} \tag{2.5}$$

The initial fit parameters were set as follows:

$\beta_1 = 0.2$;

$\beta_2 = \alpha$;

$\beta_3 = 1$;

$\beta_4 = \eta$;

$\beta_5 = T_{bottom}$;

Because of the lack of measurements between T0.1 and T1.5, this gap often lacked sampling density to verify the modeled profile. Inspired from Dake and Harleman (1969), we created a piecewise form of equation (2.5) to better model discrete observations which often were distorted from traditional exponential shapes due to the top few sensors. This led to the form:

$$T_{pw}(z \leq \beta_6) = \beta_7(z(z \leq \beta_6) - \beta_6) + T_{fit}(z \leq \beta_6) \tag{2.6}$$

$$T_{pw}(z > \beta_6) = \beta_5 + \beta_1 e^{-z\sqrt{\frac{\omega}{2\beta_2}}} + \beta_3 e^{-\beta_4 z} \tag{2.7}$$

The initial fit parameters were set as follows:

$\beta_1 = 0.2$;

$\beta_2 = \alpha$;

$\beta_3 = 1$;

$\beta_4 = \eta$;

$\beta_5 = T_{bottom}$;
$\beta_6 = z(max(\frac{\Delta T}{\Delta z}))$ for z≥1.6 m, the first sensor on the T-chain;
$\beta_7 = \frac{T1.5 - T0.1}{z1.5 - z0.1}$;

Since this temperature model solution was based on the solution of the heat equation we compared the output fit parameters to the physical quantities they were meant to represent (Figure 2.8). We were pleased to see that the fit coefficients did follow their respective measured quantities fairly well.The coefficients modulating surface and internal heat were about equal and opposite (Figure 2.8c). We believe that this was a byproduct of a nonlinear regression performed by a software which did not know the laws of physics, and where the fit parameters were not constrained. The software modulated these coefficients to obtain the best fit ignoring what they theoretically should look like. The coefficient for heat diffusivity, β_2, underestimated observations during the first part of the day but reproduced fairly well the evening increase. The absorption coefficient fell in the right range and matched observation best in conditions of low wind.

Lastly, the analytical solution of the heat equation contained the function erfc to model cooling. Including this function in the non-linear fit did not produce realistic profiles. The function erfc(z) would have needed to be offset by some depth to best fit the observation, which would have changed the form of the solution derived from the heat equation. To keep the heat equation solution as intact as possible, a hyperbolic tangent functional form was rather used when cooling dominated profile shapes. The shape of a hyperbolic tangent function resembles that of an erfc with a depth offset and therefore motivated our choice. The fit had the form

$$T_{tanh} = \beta_1 * tanh(\beta_2(z + \beta_3)) + \beta_4; \tag{2.8}$$

with initial parameters

$\beta_1 = \frac{T7.5 - T0.1}{2}$;

$\beta_2 = max(\frac{\Delta T}{\Delta z})$;

$\beta_3 =$ average depth of the largest three T_z;

$\beta_4 =$ average Temperature of the largest three T_z;

Due to the motivation behind each of the temperature form, they were each adequate under a particular set of conditions. The general rule followed (expressed here in local standard time LST)

1. From 0800 LST to 1100 LST, default to T_{pw} unless MSE(T_{tanh})<MSE(T_{pw})/2
2. From 1100 LST to 1500 LST, select the fit with the smallest MSE between T_{tanh} and T_{pw}
3. From 1500 LST to 2000 LST, select the fit with the smallest MSE between T_{tanh}, T_{pw}, and T_{heq}
4. From 2000 LST to 0200 LST, default to T_{tanh} unless MSE(T_{pw})<MSE(T_{tanh})/2
5. After a selection from these filters was made, if T_{tanh} or T_{pw} was selected but was not defined, then the fit defaulted to T_{heq} which was defined at all times.

The motivation behind these filters was to select the piecewise form at times of heating and the hyperbolic tangent form at times of cooling or within fresh water lenses (FWL), bearing in mind that a FWL can advect passed sensors at any time, and that the onset of evening cooling varied based on wind speed, stratification, and net surface heat flux. Upon inspection of the time distribution of temperature fit selected by the filter, the majority of the T_{tanh} were at night or in FWL, and T_{pw} was used most of other times. T_{heq} was selected exclusively during late night when fits of tanh and piecewise did not work

and in one FWL. Examples of original data and their fits and a summary of occurence of each temperature fit form is provided on Figures 2.9 and 2.10.

The non-linear regression of observation onto an adequate temperature model eliminated anomalies caused by sensor biases and resulted in a smoother temperature product (Figure 2.11). The goodness of fit evaluated as mean square error (MSE) were time-dependent although remained below the threshold of 0.0017°C used by Matthews et al. (2014) 99% of the time during Leg2, 95% during Leg3, and 97% during EQ14. Errors were larger during the day, which was expected given the stronger gradient during that time and in freshwater lenses (Figures 2.12 and 2.13).

Temperature gradients were then derived from a centered difference on a 0.10-meter resolution profile interpolated from the original resolution and used to estimate mixing. Since the sensors were profiling the water due to wave motion, a centered difference was a mean to consider a background gradient. This method was preferred to the analytically derived gradient.

2.5. Mixing estimates

2.5.1 Limitations in comparison of T-chain and Chameleon mixing estimates

Measurements from T-chain sensors ahead of the ship (Figure 2.3) preserved the diurnal warm layer structure but were contaminated by both swell and wind waves. The ship responded strongly to swell causing displacement of the T-chain through the water. In contrast, wind waves were minimally felt by the ship and displaced water around the sensors. The subsequent relative vertical motion of stratified water past the sensors created fictitious contributions to the temporal derivative of temperature, T_t, which was created through the product of vertical water velocity and temperature gradient, wT_z. To

bypass this contamination, we evaluated T-chain mixing estimates in the inertial range of turbulence in a frequency (wavenumber) band outside the wind wave and swell range.

Near-surface stratification, shear, and the characteristic turbulence scales will result in natural variability between the T-chain and profiler. This was particularly true in the morning as the diurnal warm layer was building and in early evening as nocturnal convection started. For these reasons there was a depth-related progression of turbulence that was reflected between the T-chain and Chameleon data. Here we compared the lowest T-chain mixing measurements at 6.6 m to Chameleon data averaged between 10-12 m. This depth range was a compromise between staying close to the T-chain range to remain closely in phase with the daily cycle of turbulence, and to be sufficiently deep below the ship wake to avoid contamination.

Other known limitations involved the inaccuracy of the fluid velocity at the tip of T-chain sensors. We used the shallowest ADCP velocity which was unable to measure the wind-induced velocity shear nearer the surface. The inaccuracies in flow speed passed sensors also resulted from the motion of the T-chain relative to the water.

2.5.2 Mixing estimates in the inertial subrange

For isotropic turbulence,

$$\chi_T = \langle 6 D_T \rangle \int_0^\infty \Phi_{T_x}(k) dk \tag{2.9}$$

where D_T is the thermal diffusivity, $\Phi_{T_x}(k)$ the power spectrum of T_x, the horizontal derivative of temperature, and k the wavenumber. This gradient of temperature was derived from $(1/\mathrm{u})T_t$ assuming Taylor's frozen flow hypothesis, where u is the lateral velocity relative to the T-chain and subscript t designates a time derivative.

The Batchelor spectrum in the inertial range satisfies (Batchelor, 1959; Dillon and

Caldwell, 1980)

$$\Phi_{T_x}(k) = C_T \chi_T \epsilon_\chi^{-1/3} k^{1/3} \tag{2.10}$$

where C_T is the Obukhov-Corrsin constant ($C_T = 0.4$, Sreenivasan (1996)), χ is the dissipation of temperature variance and ϵ the dissipation of turbulent kinetic energy (TKE). If we assume stable conditions where the temperature diffusivity $K_T = \chi/2T_z^2$ can be equated to momentum diffusivity $K_\rho = \Gamma\epsilon/N^2$ (Osborn and Cox, 1972), and expressing the spectrum as a function of frequency rather than wavenumber, the spectrum becomes

$$\Phi_{T_x}(f) = (2\pi)^{4/3}\ C_T \left(\frac{2\Gamma T z^2}{N^2}\right)^{1/3} \chi_T^{2/3}\ u^{-4/3}\ f^{1/3} \tag{2.11}$$

The observed spectrum of temperature gradient is expected to have a slope of 1/3 in the inertial subrange. Therefore we multiplied the spectrum by $f^{-1/3}$ to give it a slope closer to 0 before regressing it onto 1s. We could then solve for χ and ϵ:

$$\epsilon_\chi = \frac{\chi N^2}{2\Gamma T_z^2} \tag{2.12}$$

where ϵ_χ denotes TKE dissipation derived from the dissipation of temperature variance rather than from the shear spectrum.

Confidence limits on mixing estimates were obtained from the 90% confidence interval [b^+, b^-] of the regression coefficient. This method was applied to T-chain spatial gradients derived using Taylor's frozen flow hypothesis and the depth-averaged measured horizontal current velocity at z=12-16 m from the ship's ADCP. A constant mixing efficiency, Γ, was used (0.2, Osborn (1980)).

Example fits of observed temperature fluctuation spectrum to the Batchelor spectrum for cases of high and low χ are shown in Figure 2.14 together with confidence limits derived as above. Scaling was done over the frequency band 0.0183 - 0.0660 Hz to avoid the wave frequency band (Figure 2.14). Turbulence quantities have been evaluated

in the inertial subrange before using an error minimization routine between the integral of observed and Batchelor spectra in logarithmic space (Zhang and Moum, 2010). Our fits were however performed in linear space, explaining the perceived high bias compared to the fits of Zhang and Moum (2010). Our mixing quantities were a factor of 5 higher on average when regressed in linear space compared to the Zhang and Moum (2010) method.

2.5.3 Comparison of χ and ϵ from Chameleon and T-chain

Figure 2.15a-c shows time series of χ_T, ϵ_{Sh} derived from Chameleon profiling instruments via shear probe (Moum et al., 1995), ϵ_χ derived from T-chain and Chameleon, and T_z from three calm days with winds less than 5 m s^{-1}. Times during which the temperature gradient was $> -10^{-3.1}$ ℃ m^{-1} were removed as we considered this value a threshold for well mixed conditions. Generally the phase and amplitude of χ_T and ϵ agreed well between both instruments. High spikes in Chameleon χ_T were evident but were likely related to wake and bow thrusters contamination by the ship. The phase of the temperature gradient presented no significant lag but the amplitude nearer the surface was naturally higher. Histograms of χ show similar mean and median values (Figure 2.15d).

T-chain ϵ_χ was also similar to Chameleon ϵ_{Sh} and much weaker than ϵ_χ. Since ϵ_χ is inversely proportional to T_z and since the gradient is much stronger at the depth of the T-chain, ϵ_χ was naturally higher. ϵ_{Sh} derived from the Nasmyth spectrum also was higher and statistically different.

We can see on Figure 2.16e,k that even though χ_T and T_Z compare well between both T-chain instruments and the Chameleon, ϵ from the profiler was significantly higher than T-chain during EQ14. Winds during EQ14 were sustained and considerably stronger than during DYNAMO (wind speed during DYNAMO was 3.1±1.9 m s^{-1} and 6.9±1.3 m s^{-1} during EQ14). ϵ_χ was computed from Chameleon data and added to the histogram on

Figure 2.16k. The distribution, mean, and median of ϵ_χ were in better agreement with T-chain estimates of ϵ_χ. This signal was somewhat surprising as the pattern persisted during both stratified and unstratified conditions. Offsets between ϵ_χ and ϵ tended to be largest for weaker stratification. Given the strong wind forcing (and presumably upper layer shear that was not directly measured) during EQ14, the discrepancy may reflect the variable upper ocean shear and stratification differences measured during the two experiments. Mixing estimates between Tpods, Solos, and Chameleon show good agreement when the comparison is made between the respective χ_T and ϵ_χ estimates.

A final comparison to nighttime scalings from Lombardo and Gregg (1989) after sundown and while the temperature gradient remained below -$10^{-3.1}$ °Cs^{-1} shows hourly depth averages over the T-chain range scale within a factor of 2 during three nights (Figure 2.17).

We have demonstrated that:

1. We can derive mixing estimates using linear regression of a temperature gradient spectrum with an assumed slope of 0 onto 1s and solve for χ using the theoretical form of the Batchelor spectrum in the inertial subrange.

2. Comparison of histogram shape, mean, and median of chi and epsilon were generally consistent across platforms. This suggests that we were capable of estimating near-surface mixing from a thermistor chain that was subject to ship motion and wind wave using the inertial subrange of turbulence.

3. In situations of nighttime convection mixing estimates corroborated similarity scaling.

This justified and validated our use of thermistors mounted on a T-chain deployed from the bow of a stationary ship steered into the current to estimate the dissipation rate of temperature variance and TKE in the top 7 m of the ocean, an area where it is typically

hard to measure mixing.

2.6. Nomenclature and definition

The chosen nomenclature to label subsurface quantities throughout this dissertation is X<depth>, where X is either T for temperature, S for salinity, z for depth, or ϵ, and <depth> refers to the depth where it was measured (e.g., T1.5 is the temperature measured at 1.5 m, ϵ2.0 is turbulent kinetic energy dissipation estimated from T2.0, etc...) Throughout the manuscript we defined the diurnal warm layer (DWL) as the region above the isotherm of the average temperature at T0.1 for 30 minutes between sunrise and positive net surface heat flux. This is the depth above which most of the diurnal heat was confined regardless of stratification. It is shallowest at sunrise and deepest around sunset. The mixed layer depth (MLD) was defined as the depth where temperature is greater than at T0.1 by 0.25℃. It is deepest at sunrise and shallowest around local noon. Tmie is in GMT unless otherwise noted.

TABLE 2.1: Details of T-chain setup and mixing estimates calculation for DYNAMO and EQ14

	DYNAMO		EQ14	
	Tpods	CTD	Tpods	Solos
Number of sensors	8	2	12	9
Sampling frequency	10 Hz	3 sec	100 Hz	2 Hz
Depth range	$1.5 - 7.5$ m	$4.2, 7.6$ m	$0.8 - 9.2$ m	$1.2 - 10.7$ m
Sensor Separation	$0.2 - 0.7$ m		$0.2 - 1.5$ m	
Deployments	$08 - 26$ Oct 2011 (Leg2) $12 - 24$ Nov 2011 (Leg3)		15Nov $-$ 03Dec 2014	
Location	0°$-$ 80°E		0°$-$ 110°W	
Frequency range	$0.0183 - 0.066$ Hz	NA	$0.001 - 0.01$ Hz	
Spectra length	10 min	NA	20 min	

2.7. Tables and Figures

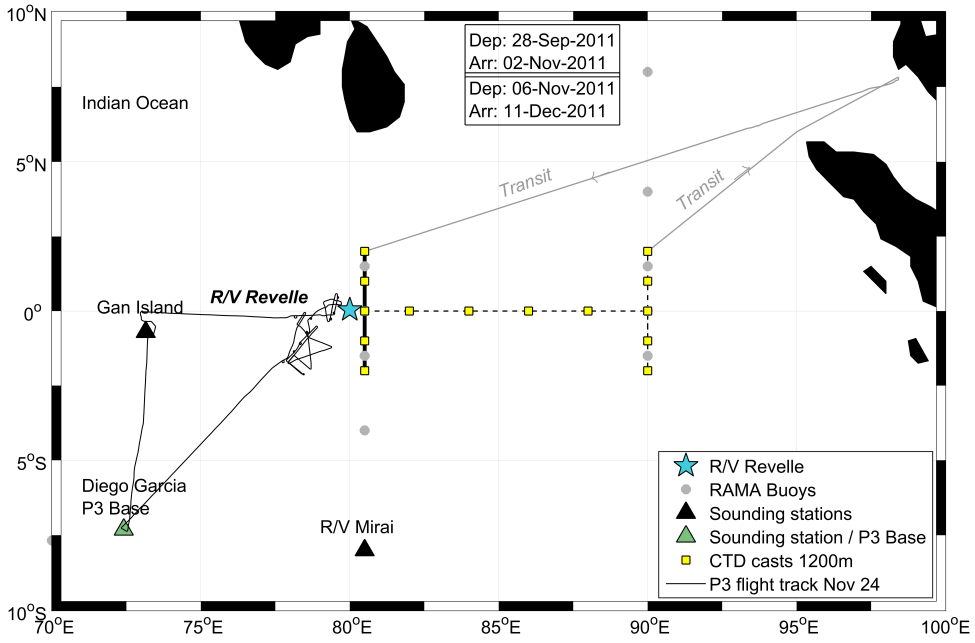

FIGURE 2.1: Map of the location of the R/V Revelle during DYNAMO with cruise dates and some additional data collection.

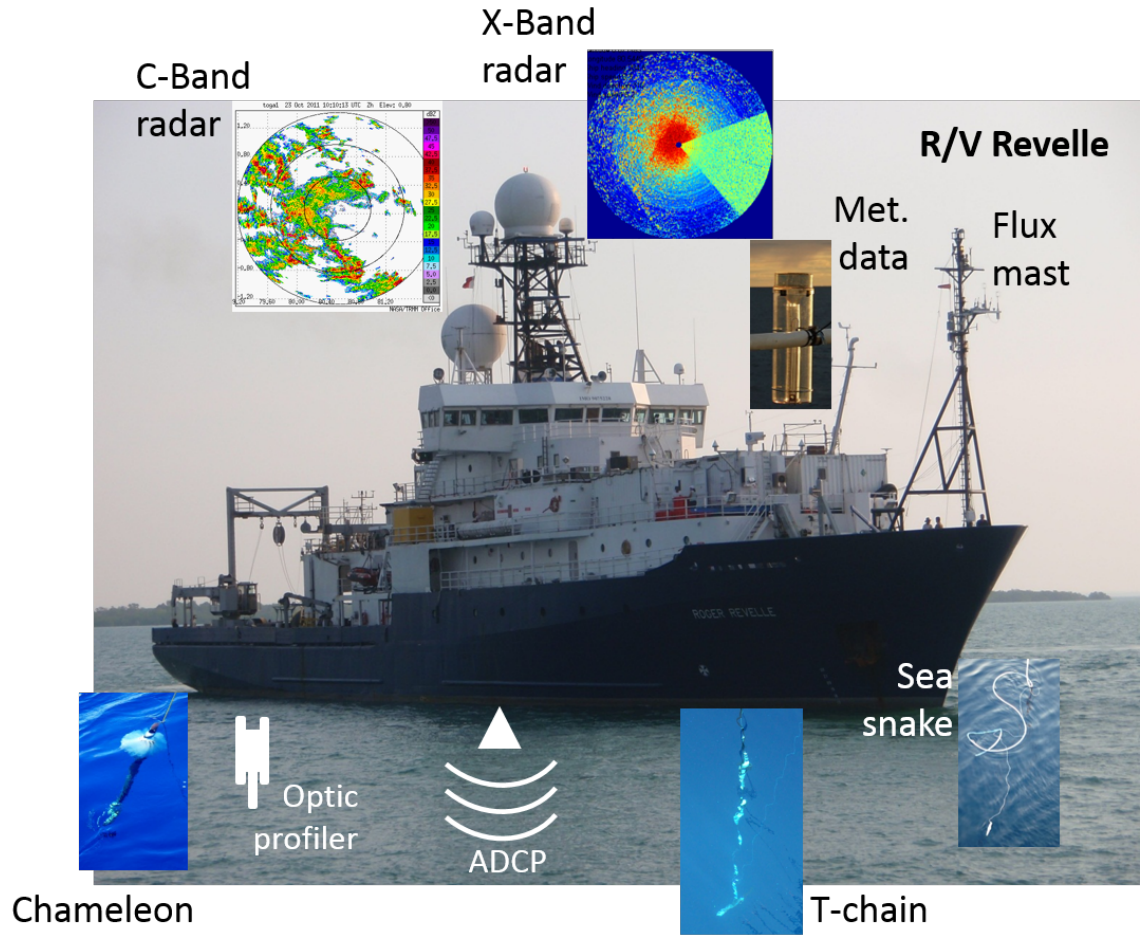

FIGURE 2.2: R/V Revelle and schematic or photos of instruments used during DYNAMO, as well as example maps produced by the C-band and X-band radars. (Photo credits: Derek Coffman (rain gauge), Simon DeSzoeke (sea snake), Alexander Perlin (Chameleon), Jim Moum (R/V Revelle), and Aurélie Moulin (T-chain)).

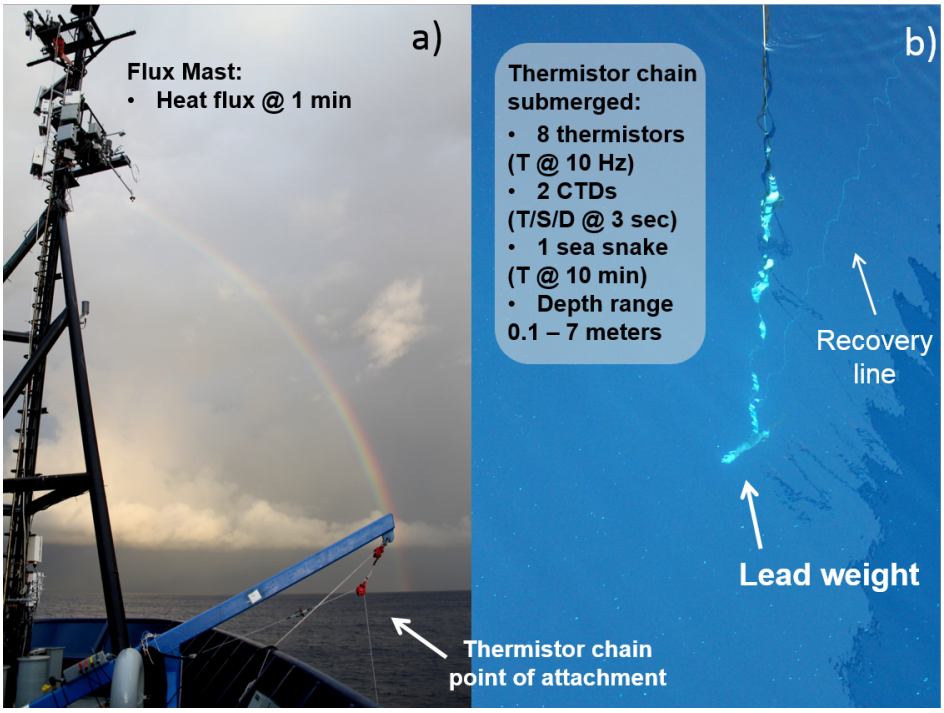

FIGURE 2.3: Deployment setup of the T-chain during DYNAMO. (a) beam mounted on starboard bow besides the flux mast, (b) T-chain deployed seen from the deck (Photo credits: Aurélie Moulin)

.

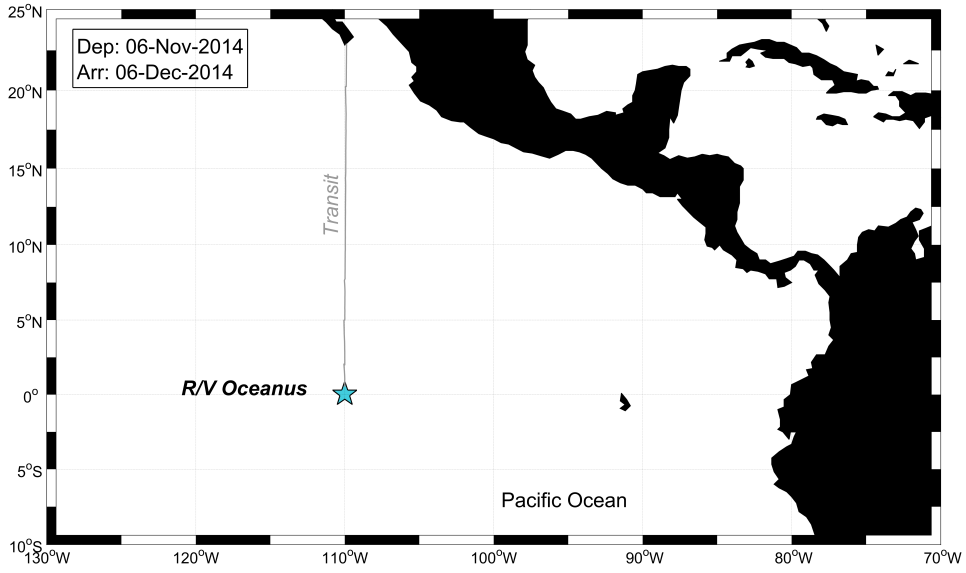

FIGURE 2.4: Map of the location of the R/V Oceanus during EQ14 with cruise dates.

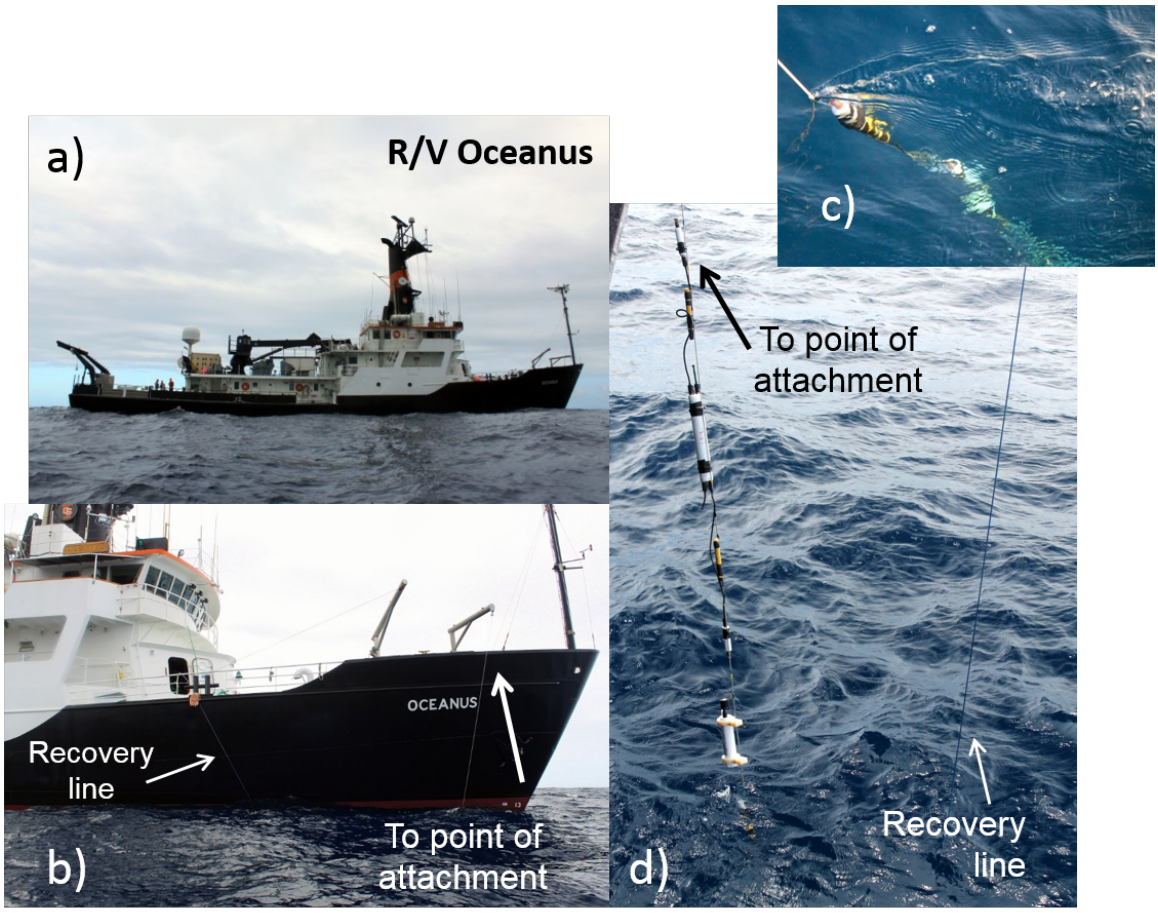

FIGURE 2.5: R/V Oceanus setup of T-chain deployment. (a) Starboard view of the ship, (b) point of attachment of the T-chain and its recovery line while deployed, (c) deck view of top most sensor, and (d) Deck view of the T-chain during deployment showing the sequence of sensors (Photo credits: Aurélie Moulin)

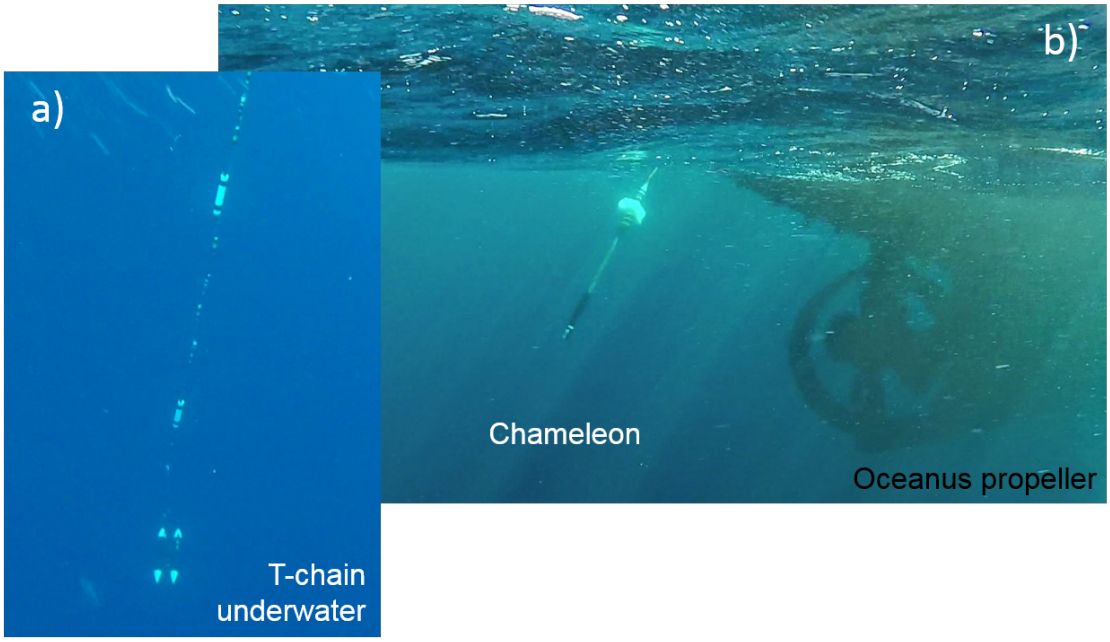

FIGURE 2.6: Underwater view of the T-chain (a) and Chameleon (b). (Photo credits: Aurélie Moulin)

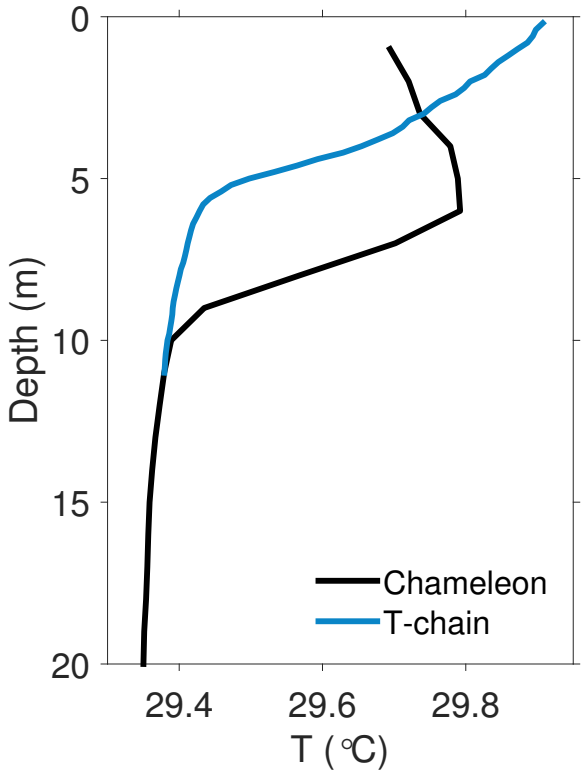

FIGURE 2.7: Simultaneous temperature profiles in the upper ocean from the Chameleon profiler (black) and from the T-chain (blue) illustrate the complementarity of these instruments. Three extra CTDs were installed at 8.6 m, 9.7 m, and 10.7 m during the second half of the deployment which explains the deeper extent of the T-chain profile than discussed in the main paper.

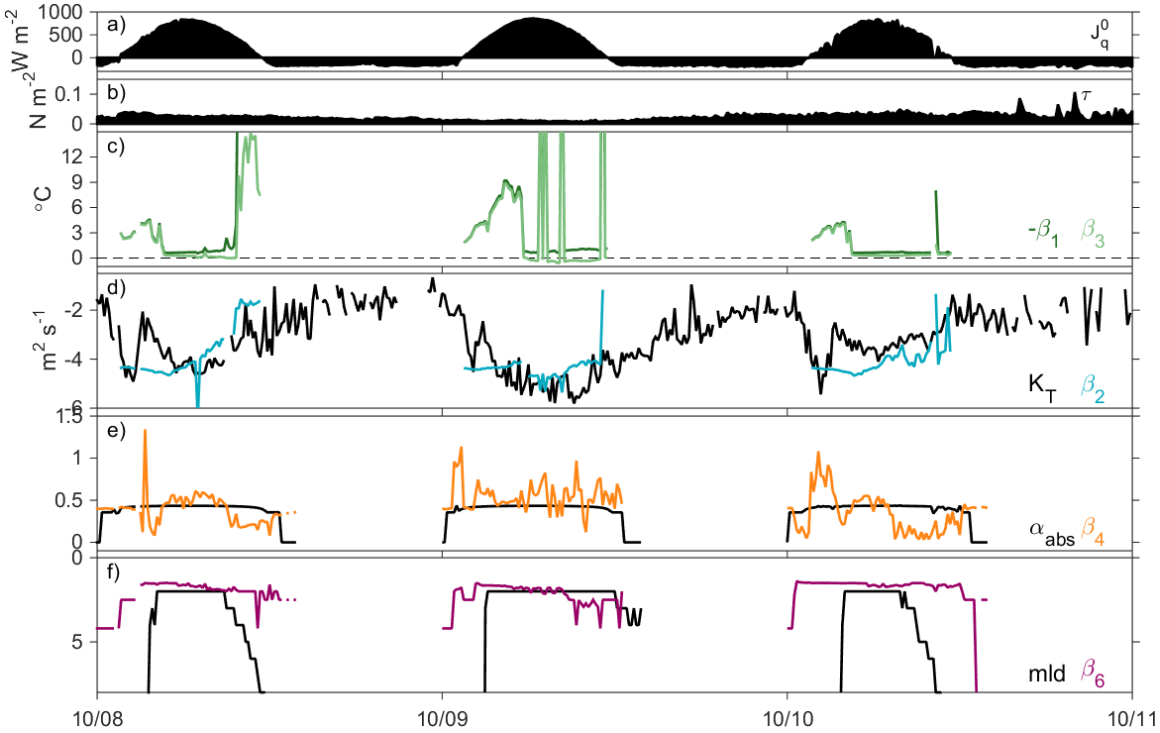

FIGURE 2.8: Fit parameters output from nonlinear regression compared to the physical quantities they are meant to represent when the heat equation solution is applied. (a) Net surface heat flux, (b) wind stress, (c) coefficient modulating the external heat forcing (β_1) and internal heat (β_3), (d) heat diffusivity averaged over the top 3 Tpods and β_2, (e) solar absorption and β_4, and (f) mixed layer depth when the piecewise fit form is selected and β_6

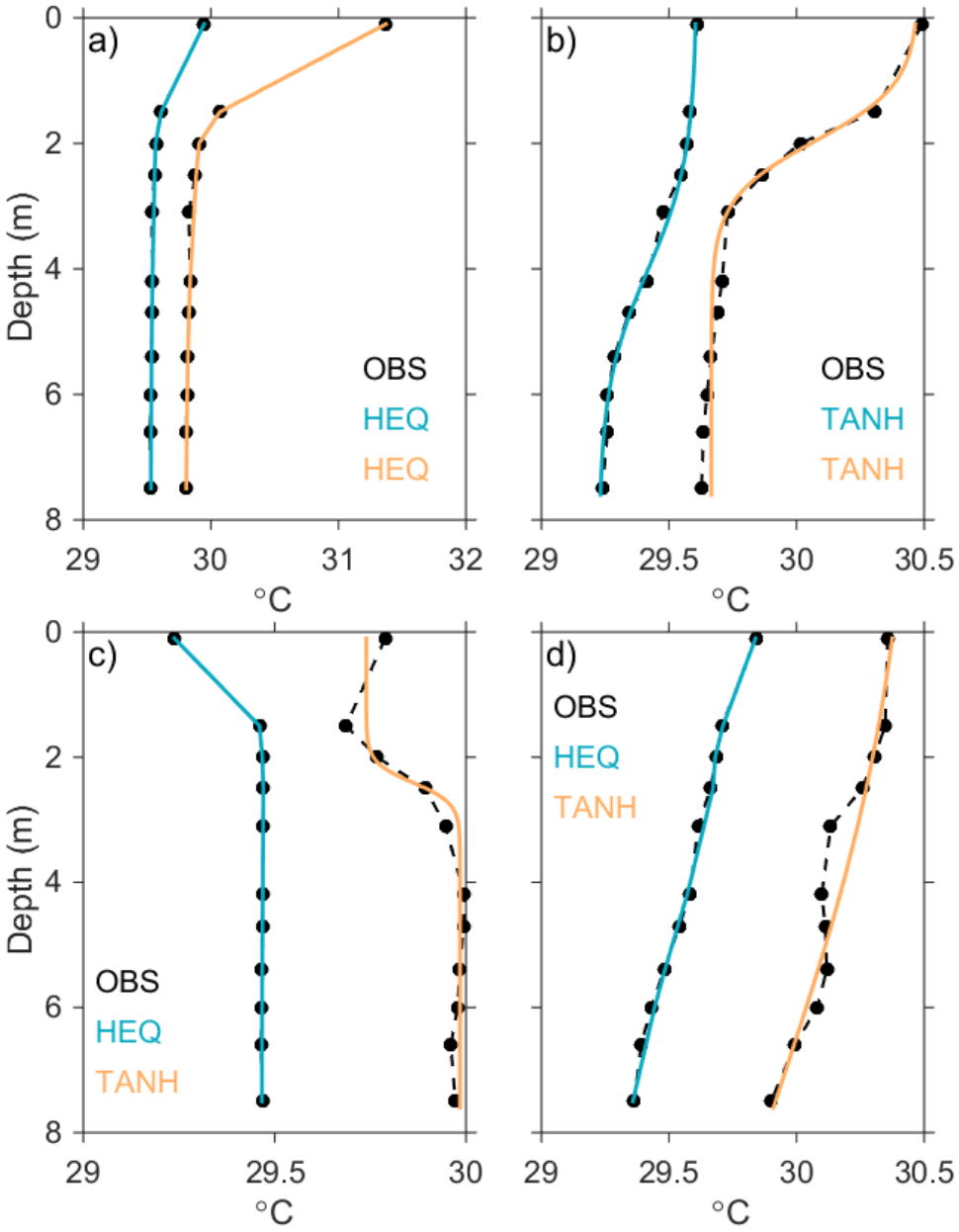

FIGURE 2.9: Examples of observed temperature profiles and their selected fit in various stratification conditions. (a) Intense solar heating and weak wind, (b) early evening cooling, (c) freshwater lenses, (d) windy conditions.

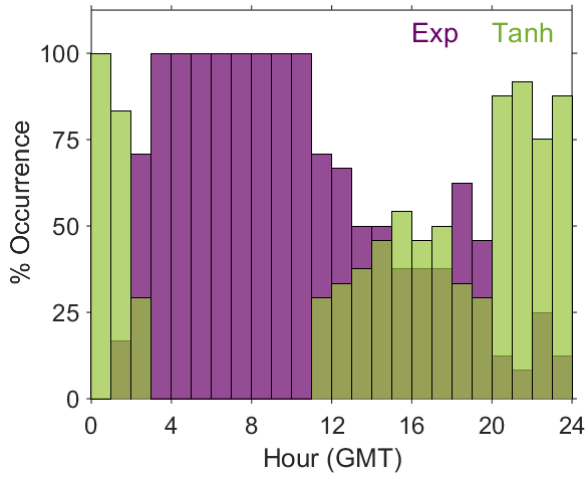

FIGURE 2.10: Histogram of occurrence of exponential temperature fit from either the heat equation or its piecewise form versus the tanh form. This illustrates the need for exponential shape midday and tanh in the early evening.

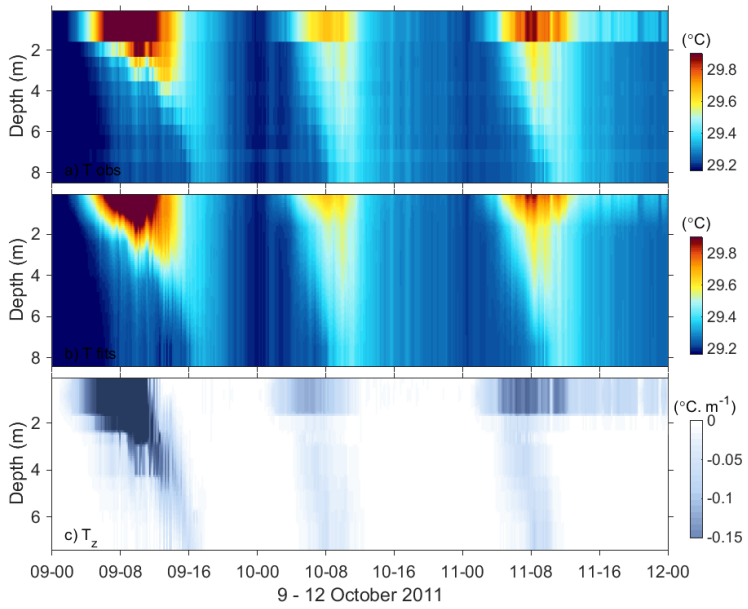

FIGURE 2.11: Comparison of original and fitted temperature products. (a) Observed temperature, (b) fitted temperature, and (c) vertical temperature gradient.

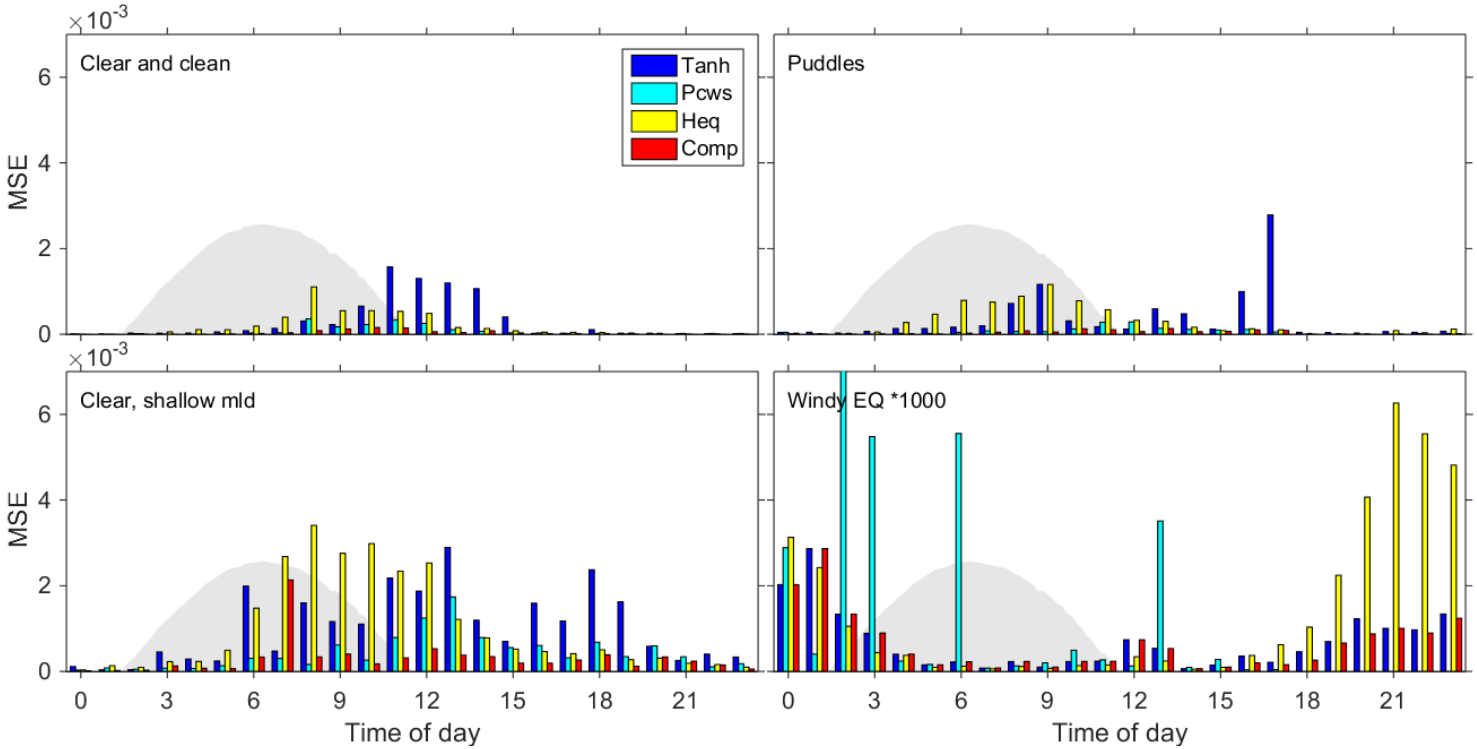

FIGURE 2.12: Mean squared error (MSE) of three temperature profile models non-linearly fit to observed profiles. The models were based on a hyperbolic tangent function (Tanh), piecewise heat equation form (Pcws), the solution to the heat equation (Heq), the composite from these three fit forms (Comp). MSEs were composited into days that were calm and free of freshwater lenses, days with a strong diurnal warm layer or a barrier layer resulting in a shallow mixed layer depth, days with lenses and windy days (essentially EQ14). Solar radiation is shaded as a reference of the time of day.

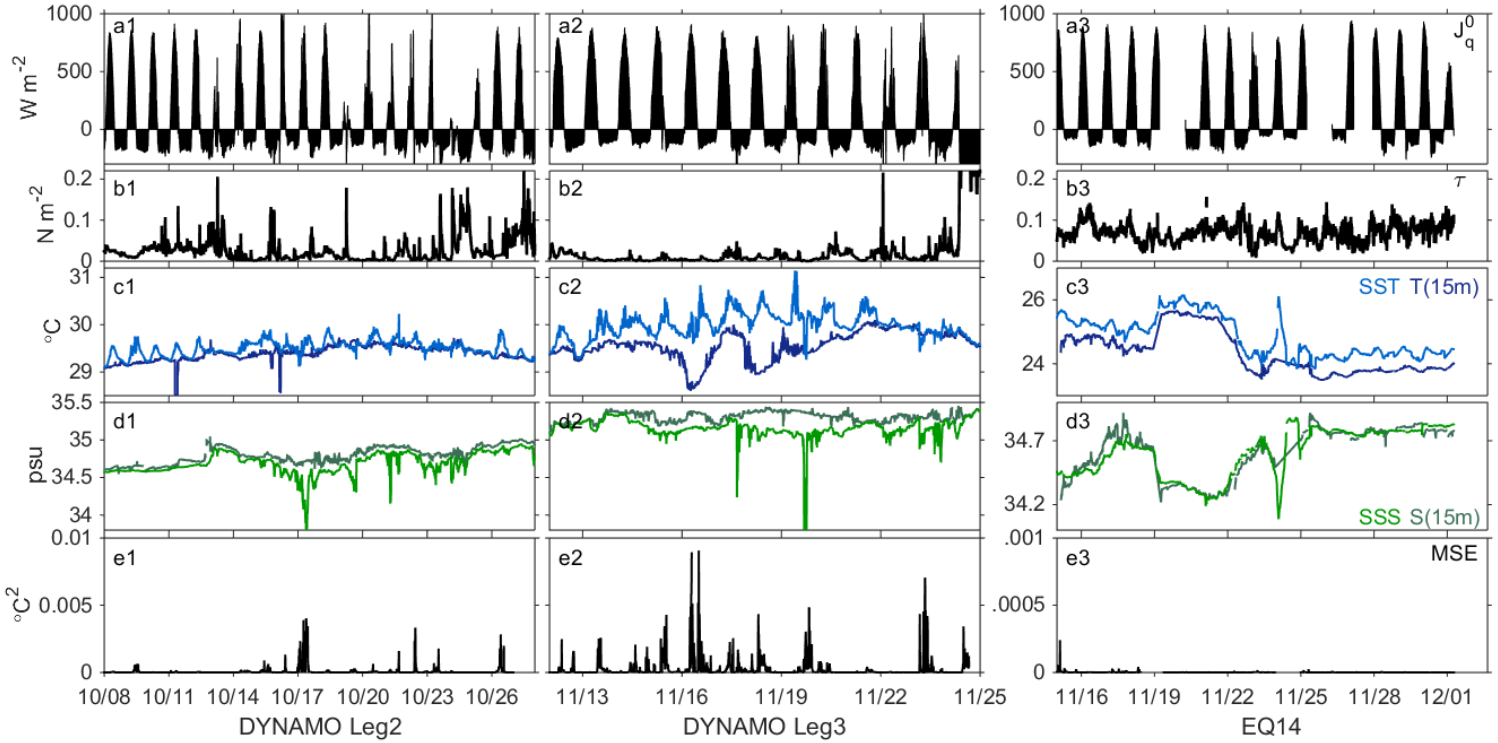

FIGURE 2.13: Net surface heat flux (a1-3, Wm^{-2}), wind stress (b1-3, Nm^{-2}), water temperature at the surface and at 15 m (c1-3, ℃), salinity at the surface and at 15 m (d1-3, psu), mean square error (e1-3, $℃^{-2}$).

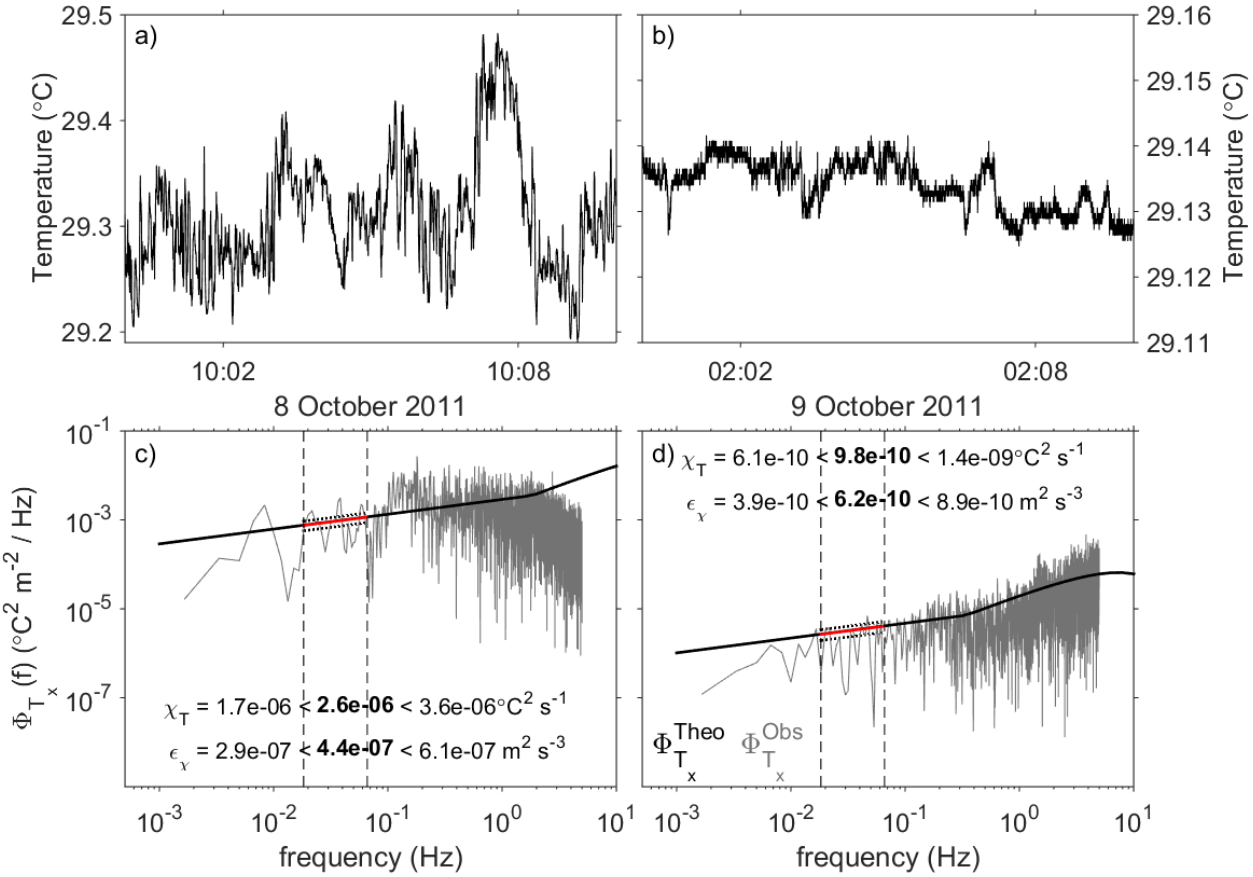

FIGURE 2.14: Temperature timeseries and their derived turbulence quantities from spectrum fitting. (a,b) Ten minutes of fast temperature data from T6.6 deployed during DYNAMO Leg2; (c,d) spectra of T_x (grey) fit to the Batchelor spectrum (black) between frequencies 0.0183-0.066 Hz (dashed). The resulting χ_T and ϵ_χ estimates are printed on panels (c,d). Panels (a,c) on the left represent an example of high temperature variance dissipation, panels (b,d) represent an example of low temperature variance dissipation.

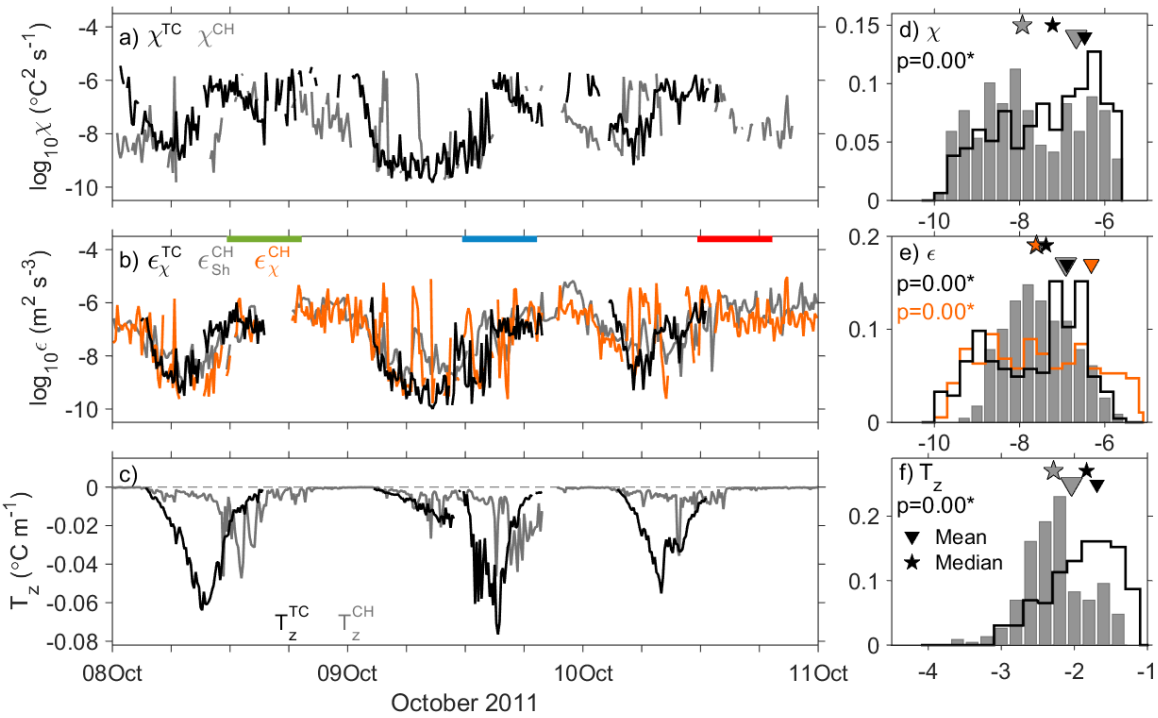

FIGURE 2.15: Comparison of turbulence quantities and temperature gradient between Tpods and Chameleon profiler over three days. (a,d) Dissipation of temperature variance, χ_T, from Chameleon (CH, 10 - 12 m) and Tpod (TC, 6.5 m) during DYNAMO Leg2 with their respective histograms, mean and median. (b,e) Time series and histograms of the dissipation of turbulent kinetic energy evaluated from the Chameleon shear probes, ϵ_{Sh}^{CH}, Tpods ϵ_χ^{TC}, and ϵ_χ^{CH}. (c,f) T_z and their histograms. p-values of Kolmogorov-Smirnov tests between T-chain and Chameleon variables are marked by an asterisk if there is a significant difference. The green, blue, and red bars atop panel (b) reflect the time period used in Figure 2.17.

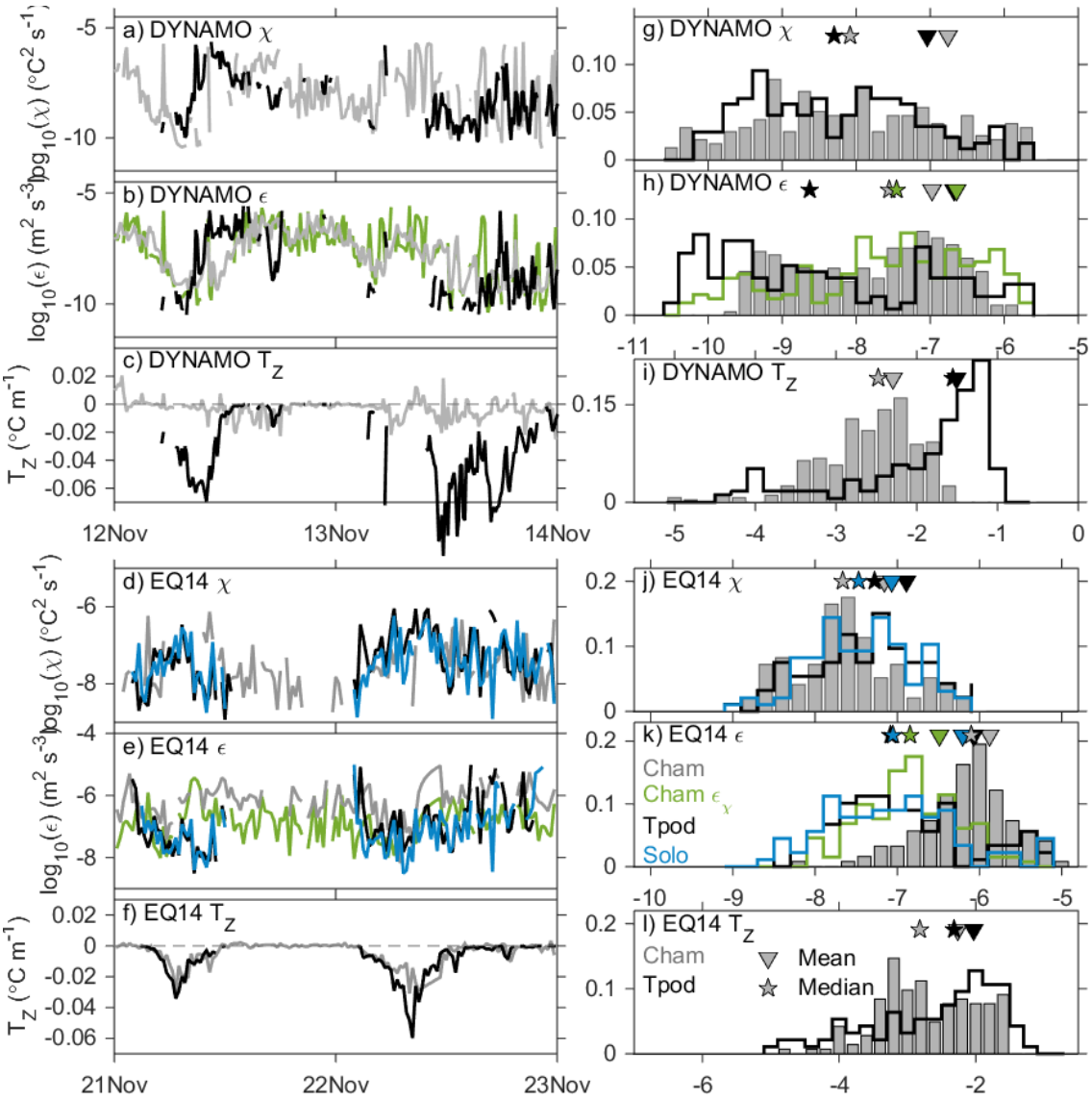

FIGURE 2.16: Dissipation of temperature variance (a), and of TKE (b), and temperature gradient (c) for DYNAMO Leg3 measured by Chameleon and Tpods. Their respective histograms, means, and medians are presented on panels g-i). The same set of variables and histograms for EQ14 is presented on panels d-f and j-l for Chameleon, Tpod and Solo sensors.

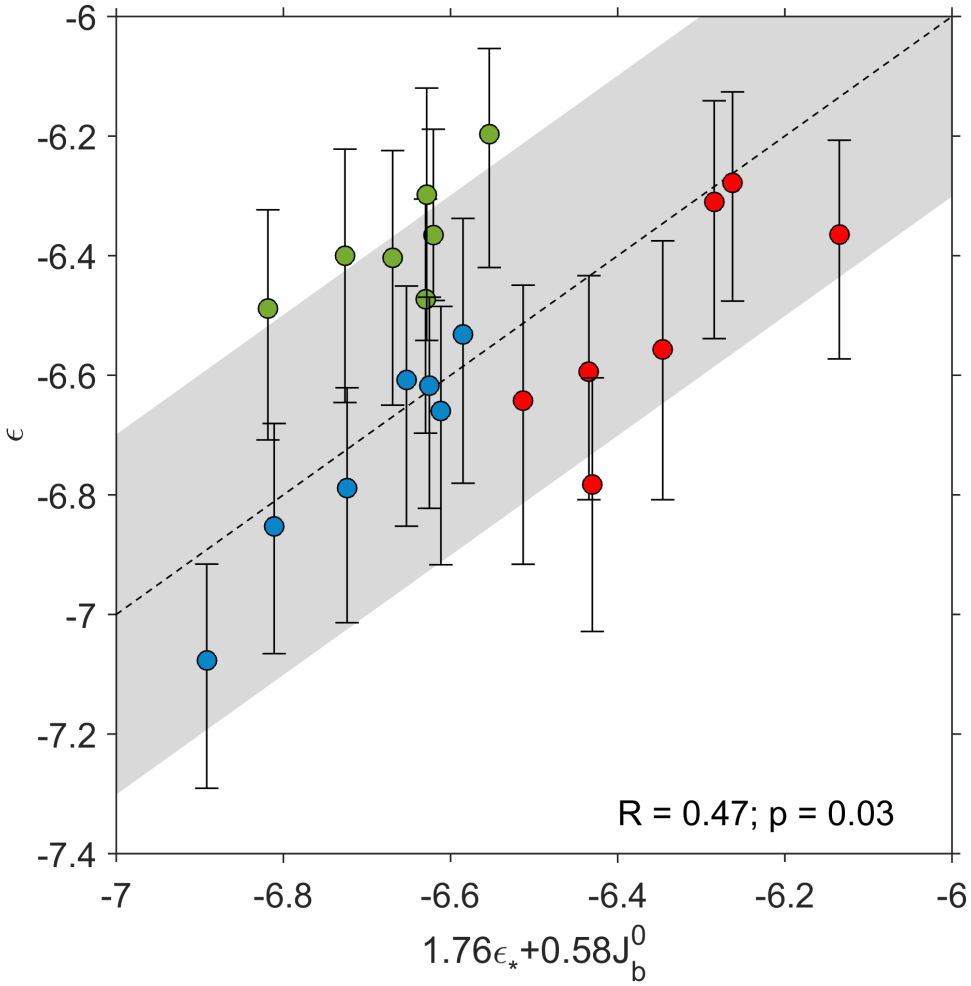

FIGURE 2.17: Scatter plot of nighttime scaling 1.76 ϵ_* + 0.58 J_b^0 from Lombardo and Gregg (1989) vs. depth average of observed mixing estimates in green, blue, and red for 08 - 09 - 10 October 2011, respectively, also referenced on Figure 2.15. $\epsilon_* = u_*^3/\kappa z$, $u_* = \sqrt{\tau/\rho}$, where κ=0.4 is the Obukhov-Corrsin constant (0.4, Sreenivasan (1996)), u_* the friction velocity, τ the wind stress, ρ the water density, and J_b^0 the surface buoyancy flux. The correlation coefficient R = 0.47 with a p-value of 0.03 (R_{crit}=0.45, N=21, 95% confidence interval). The grey shading indicates a factor 2.

Evolution of turbulence dissipation in the surface mixed layer in low wind speed conditions

Aurélie J. Moulin, James N. Moum, and Emily L. Shroyer

3. EVOLUTION OF TURBULENCE DISSIPATION IN THE SURFACE MIXED LAYER IN LOW WIND SPEED CONDITIONS

3.1. Abstract

Upper ocean measurements of temperature and turbulence within the diurnal warm layer showed the daily evolution of mixing under low to moderate wind forcing and strong insolation in the equatorial Indian Ocean. Nighttime convective mixing abruptly decreased by two orders of magnitude in the few hours after sunrise with a decay rate inversely proportional to stratification. This period of attenuated mixing was followed by a rapid increase, in which the turbulent kinetic energy (TKE) dissipation, ϵ, grew several orders of magnitude in few hours at a rate proportional to a combination of the local shear and stratification. During this time, skewed temperature ramps developed and grew supporting the interpretation that enhanced mixing was a shear-driven response to the trapping of momentum within the nascent diurnal warm layer. After the period of growth, turbulent mixing approached an equilibrium determined by the balance of shear and buoyancy production. Nighttime levels compared to similarity scaling.

TKE dissipation in low wind conditions exceeded law-of-the-wall scaling within the mixed layer but matched the scaling well in windy conditions. We found particular relationships between ϵ and temperature gradient in the presence or absence of temperature ramps, hinting at possible different parameterizations based on background conditions.

3.2. Introduction

Heat and momentum are transferred to the ocean interior through a shallow transition zone between the atmosphere and the seasonal thermocline. Within this transition

zone, heat is accumulated and released on a daily basis from strong insolation in the diurnal warm layer (DWL), a thin region which warms significantly relative to the deeper mixed layer temperature (Fairall et al., 1996a). The DWL thickness grows throughout the day encapsulating most of the heat added during daytime, and decays at night as convective plume from surface cooling enhance mixing and dissipate the accumulated heat. The DWL resets in the shallows every morning when a new diurnal cycle begins. The representation of the DWL and its heat content in ocean models is necessary for improved accuracy of computer simulations as evidenced in Seo et al. (2009). Limitations to our understanding nevertheless persist and large scale parameterization still do not resolve the necessary physical processes. This study presents new observations of turbulent kinetic energy (TKE) dissipation, ϵ, in the upper equatorial Indian Ocean during the daytime in weak to moderate wind conditions, providing the opportunity to detail the daily evolution of turbulence near the surface under variable stratification regimes.

Previous work has shown that turbulence decays by an order of magnitude in the two hours following sunrise as the surface layer restratified from surface heating (Brainerd and Gregg, 1993a,b). As heat accumulates in the increasingly stably stratified DWL, so does momentum imparted from the wind to form a diurnal jet (Thorpe, 1978; Price et al., 1986) with velocity anomalies up to 0.19 m s^{-1} (Kudryavtsev and Soloviev, 1990). This diurnal jet is thought to create shear instabilities at the DWL base, which grow and break from accumulated shear (Smyth et al., 2013), entraining cool fluid from below into the DWL, thereby deepening it and enhancing turbulent dissipation (Thorpe, 1978). Concurrently, observations of vertically coherent tilted temperature oscillations, often called "ramps", have been reported in the ocean since the late 1970s in both stable and convective conditions. They feature a sudden rise or fall of temperature of a few tens of milli-degrees and were estimated being 20 - 23 meters apart in wind speeds approximately 5 - 12 m s^{-1}, a length scale similar to the mixed layer depth (Thorpe et al., 2003). Their skewness

changes sign based on the sign of the net surface heat flux and the relative direction of the wind (Thorpe et al., 1991; Wijesekera et al., 2004) from positive into the wind during surface heating conditions to negative during surface cooling (or the opposite when measured downwind) (Wijesekera et al., 2004; Thorpe et al., 2003; Thorpe and Osborn, 2005). These ramps are thought to signify Kelvin-Helmholtz billows (Thorpe, 1978; Thorpe and Osborn, 2005).

The causality between ramps and TKE dissipation was first suggested by Thorpe (1978) based on ϵ scalings. To the best of our knowledge, no simultaneous observations of temperature ramps and turbulence in the DWL have been reported. Our study is unique in that it provides time series of both temperature ramps and ϵ in the top seven meters of the equatorial ocean in varying wind and background stratification conditions. These observations offer a new look into the detailed evolution of daytime dissipation rates (Section 3.4.), and allow a first order scaling of ϵ (Section 3.5.). We offer an interpretation of the daytime cycle of turbulence in low-moderate wind and look at very low or high wind regimes in (Section 3.6.).

3.3. Methods

3.3.1 Temperature ramps and their detection

Temperature ramps are characterized by an abrupt change in temperature, often sought after in the skewness of the temperature derivative, and by a narrowband peak in spectral power (0.0024 - 0.0167 Hz). Skewness alone is not a sufficient indicator of ramps as it could be caused by waves, larger scale temperature fronts such as fresh water lenses, or small random features. Instead, we derived a weighted skewness (Skw) from the combination of skewness of derivative and spectrograms of band-passed temperature (0.0005 - 0.03 Hz). Narrowband peaks were arbitrarily sought after in the 1-7 min range of

the 0.05 Hz band-averaged spectrograms by normalizing a 3-point running variance with the daily maximum variance in that frequency range. We retained times when Skw>0.1 $(℃\ s^{-1})^2\ Hz^{-1}$ as indicative of narrowbanded, skewed temperature features.

Lastly we acknowledge the possibility of Langmuir circulations (LC) and our inability to distinguish them from shear instabilities (SI). The magnitude of the skewness, weighted skewness, or turbulence did not change with respect to the relative direction of the wind to the current, which did not vary much. Langmuir circulations are in the same approximate frequency band as shear instabilities and could also produce temperature oscillations. Our upper ocean velocity dataset from ship-mounted ADCP was too coarse to seek coherence of horizontal and vertical velocities as a sign of LCs, and so we were unable to diagnose whether a temperature ramp might be caused by a shear instability or a LC, especially in cases of weak to moderate skewness.

3.4. Evolution of Turbulence in the diurnal warm layer

The behavior of daytime mixing followed a consistent pattern on days with light - moderate winds when the heat budget was mainly one dimensional.

Upon sunrise, temperature at 0.1 m subtly increased on 8 October 2011 (Figure 3.1), a sign of the nascent diurnal warm layer even as the net surface heat flux remained negative (cooling). Nighttime convective mixing was thus terminated by penetrating solar radiation which provided sufficient internal heat to raise temperature at T0.1 and restratify the ocean surface before the net surface heat flux became positive (Figure 3.1). The net temperature at T0.1 being a balance between the instantaneous absorption of solar flux at that depth and heating (or cooling) at the surface (Fairall et al., 1996a), local warming can be observed when internal heating and surface cooling are small. A decay in turbulence was coincident and continued for about one hour after the change of surface heat flux to

warming.

Following this turbulence decay temperature significantly increased along with stratification in sensors above 2.5 m while ϵ rapidly increased. The growth following the morning minimum lasted until the MLD had reset near the surface and the local temperature increased markedly faster. The rate of increase was variable and directly correlated to the degree of stratification. At 1.5 m ϵ remained high and weakly but steadily increased throughout the afternoon until temperature peaked. At the onset of temperature decrease in late afternoon as the local temperature gradient collapsed, a secondary and modest local minimum in ϵ was observed. Upon nightfall and the change of net surface heat flux into cooling, convective mixing resumed and generated turbulence comparable to similarity scaling in neutral boundary conditions ($(1.76\epsilon_* + 0.58J_b^0)$ where ϵ_* is the Law-of-the-Wall approximation $u_*^3/\kappa/z$, u_* is the friction velocity $\sqrt{\tau/\rho}$, and J_0^b is the surface buoyancy flux (Lombardo and Gregg, 1989). This daily cycle in $\epsilon 1.5$ was observed for three consecutive days (Figure 3.1).

The cycle of $\epsilon 2.5$ showed some variations from that at 1.5 m. The morning minimum was not as weak, although the phase of the abrupt decrease and rapid increase early-mid morning was approximately synchronous over the top 3 m. Once recovered from the morning minimum, $\epsilon 2.5$ m either maintained its intensity (e.g. 10 October) or decreased for some time (e.g. 9 October) (Figure 3.1). This difference coincided with whether the MLD was above or below the sensors. We hypothesize that the initial rise in ϵ below 2.5 m was caused by heating throughout the water column creating small turbulent eddies, but decreased mid-late morning as the MLD shoaled above these depths, confining heat above. Deeper sensors were then cut off from surface sources of turbulence, leading to a decrease in mixing. This was further supported by the behavior of ϵ during the second half of the day below 2.5 m which steadily decreased as long as the warming trend of temperature remained low, likely only caused by penetrating sunlight while in the mixed

layer above, the influence of the net surface heat flux increased heating more drastically. Turbulent dissipation increased again deeper along the chain, often very sharply, as the MLD neared and overtook the sensors measuring mixing to immerse them into the mixed layer.

3.5. Scaling of turbulence decay, growth, and equilibrium state

The cycle of turbulence in the water column is governed by the evolution equation for turbulent kinetic energy. Total changes to TKE are determined by a balance between shear production, buoyancy production (or destruction), and dissipation:

$$\frac{\partial}{\partial t}q^2 = P + B - \epsilon \tag{3.1}$$

where the TKE $\mathrm{q}^2 = \frac{1}{2}\overline{u_i u_i}$, the shear production $\mathrm{P} = \overline{u_i u_j}\frac{\partial u_i}{\partial x_j}$, and the buoyancy production (destruction) $\mathrm{B} = (g/\rho\overline{w'\rho'})$ with g the gravity, ρ the density, w the vertical velocity, overbars denoting mean quantities and primed quantities denoting the turbulent fluctuations around their mean. Three limiting cases are considered: the decay, growth, and equilibrium state of turbulence.

3.5.1 Decay

The decay rate of ϵ once cut off from surface sources by restratification was described by Brainerd and Gregg (1993a) and refined by Smyth et al. (1997) following the capping of the ocean's surface by a freshwater lens. They both derived a time scale for viscous

dissipation from a reduced TKE equation when shear and buoyant production were absent:

$$\frac{\partial}{\partial t}q^2 = -\epsilon \tag{3.2}$$

An invicid scale relationship for ϵ is given by

$$\epsilon = \frac{C_\epsilon q^3}{l} \tag{3.3}$$

where C_ϵ=0.54 is a proportionality constant (Smyth et al., 1997). Replacing l with the Ozmidov length scale $L_o = \sqrt{\epsilon/N^3}$,

$$\epsilon = q^2 N\mathcal{C} \tag{3.4}$$

where $\mathcal{C} = \left(\frac{C_\epsilon}{a}\right)^{2/3}$ with a=1 a proportionality constant (Smyth et al., 1997). Solving (3.2) with (3.4),

$$\epsilon \propto e^{(-t/\tau_d)} \tag{3.5}$$

where $\tau_d = (N\mathcal{C})^{-1}$ is a viscous time scale for the decay of ϵ. This decay rate corroborated our observation following restratification after sunrise and below the MLD once it had reset near the surface. These two cases were each discussed in Brainerd and Gregg (1993a) and Smyth et al. (1997).

3.5.2 Rapid Growth

The morning minimum of ϵ ended as the water column became sufficiently stratified for shear production. The TKE balance should then be between accumulating shear from wind, buoyancy destruction from net surface heat flux, and viscous dissipation. From equation 3.1, we have assumed that the shear production P was approximated as $u_*^3/\kappa z$, with κ=0.4 the Kolmogorov constant. We expressed buoyancy destruction as

$B = -g\alpha \dfrac{J_q^h}{\rho C_p}$ with turbulent heat flux $J_q^h = \rho C_p K_T T_z$, where C_p is the heat capacity of water (4000 J kg^{-1} ℃$^{-1}$), and T_z is the temperature gradient. The temperature diffusivity $K_T = \chi/2T_z^2$ was equated to the momentum diffusivity $K_\rho = \Gamma\epsilon/N^2$ in stable stratification conditions, and with $N^2 = g\alpha T_z$ the buoyancy frequency. Equation (3.1) became

$$\frac{\partial}{\partial t} q^2 = \frac{u_*^3}{\kappa z} - (\Gamma + 1)\epsilon \tag{3.6}$$

which, when solved for TKE dissipation gave a growth rate

$$\epsilon \propto e^{(t/\tau_g)} \tag{3.7}$$

$$\tau_g = \left(\frac{u_*}{\kappa z} - (1 + \Gamma)\mathcal{C}N \right)^{-1} \tag{3.8}$$

This growth rate was terminated either once the system reached steady state or when the MLD was reset above, closer to the surface thereby isolating the ocean's interior from surface sources.

3.5.3 Steady state

In a steady state balance the TKE budget became

$$\frac{u_*^3}{\kappa z} - (\Gamma + 1)\epsilon = 0 \tag{3.9}$$

$$\epsilon = \left(\frac{1}{1 + \Gamma} \right) \frac{u_*^3}{\kappa z} \tag{3.10}$$

which is equivalent to the Law of the Wall scaling modulated by a constant. This equilibrium state was observed following morning rapid growth.

3.6. Discussion

3.6.1 Interpretation of the cycle of turbulent kinetic energy dissipation

The repeatability of the daytime behavior of ϵ showed the remarkable synchrony of the abrupt shutdown of mixing following sunrise (Figure 3.2e). The time to recover from the morning minimum did more or less coincide with local temperature increasing markedly faster.

The observed decrease in TKE dissipation after sunrise followed the parameterization from Smyth et al. (1997) (Figure 3.2e). The primary nocturnal source of TKE in low winds being buoyancy, sunrise suppressed the buoyancy source, and ϵ decayed near the surface. The same phenomenon was described in Smyth et al. (1997) as a turbulent patch was cut off from the surface sources of TKE by a freshwater lens. While this decay was ongoing, the dying eddies were still capable of transporting some heat from the surface contributing to local heating before formal restratification and appearance of a newly formed MLD (Brainerd and Gregg, 1993a). This parametrization worked within approximately 20% on each of the three days (Figure 3.2f). Difficulties in deriving temperature gradients from discrete sensors at times of weak stratification might explain the larger deviation of the predicted decay rate on 8-9 October from the observations.

The scaling for the growth rate of ϵ (Figure 3.2g) followed observations surprisingly well (Figure 3.2g). This parameterization relied on shear, buoyancy, and dissipation, which all changed daily based on varying wind conditions. This highlights the tight coupling between the atmosphere and the top two meters of the ocean in low wind and strong insolation conditions. Afternoons featured an approximately steady dissipation rate while stratification peaked. On days with moderate stratification ϵ reached this scaling by late afternoon. The stronger the buoyancy frequency, the longer it took to approach scaling estimates (e.g. 9 October, Figure 3.2e). This relationship points to a balance between buoyancy gain at the surface through heat from the sun and buoyancy loss at the base of

the mixed layer.

In stably stratified conditions the likely source of turbulence must be shear, a clear sign of which are temperature ramps (Figure 3.3). Weak temperature ramps were observed on a daily basis close to the surface starting mid-morning as the MLD had reset. The evolution of ramps on 10 October 2011 is illustrated on Figure 3.4A-D. At 0512, oscillations at 1.5 m were about 1 minute long (36 meters with a current velocity of 0.60 m s^{-1}). They grew in length up to 2 minutes (72 meters) by 1051. This growing billow size was possibly caused by the increasing buoyancy frequency over the same time period (Hazel, 1972; Moum et al., 2011). Their amplitude also evolved not only temporally from 0.02 to 0.12℃ at T1.5 between 0512 - 0826 but also spatially peaking at 0.2℃ at 0826 at T6.0, decreasing thereafter to about 0.15℃ by 1051. By that time the temperature gradient at the surface had nearly collapsed as the skewness turned negative, indicating cooling. The changes in amplitude reflected the growing vertical temperature gradient which was folded within the Kelvin-Helmholtz (KH) rolls sampled by the sensors.

The distribution of ϵ showed about an order of magnitude higher dissipation when temperature ramps were observed (Figure 3.4e). The presence of ramps evolved in time and space over the course of a day (Figure 3.4f). In the morning ramps were predominantly found above 4 m and in small numbers. By noon ramps were more numerous and seen more substantially down to 5.4 m. In the early evening, ramps were found in highest numbers at all depths. This indicated a time and space development of Kelvin-Helmholtz billows which followed ϵ and supported its origin as shear instability.

3.6.2 Daytime turbulence in different wind and stratification conditions

The dynamic range of atmospheric and stratification condition offered in DYNAMO and EQ14 dataset allowed to assess whether the magnitude of ϵ changed in these different conditions. TKE dissipation followed Law-of-the-Wall scaling based on wind stress

(equilibrium state, Section 3.5.3). We were able to verify how well this scaling works in varying winds and at various depths. Profiles of T, N^2 and ϵ during Leg2 are illustrated on Figure 3.5a-k. These trends were discussed in Section 3.4. and are only shown here for reference. Note the overall agreement between TKE dissipation and ϵ_*.

During Leg3 the stratification was stronger in the top 3 meters. Temperature was much higher at the surface, N^2 was up to an order of magnitude higher at 1.5 m, and ϵ exceeded ϵ_*. Magnitude of ϵ near the surface beyond similarity scaling estimate was presented in Callaghan et al. (2014). They observed similar overestimate of ϵ in a single profile shortly before the onset of the surface mixed layer deepening in early afternoon. Their corresponding buoyancy frequency was around 10^{-5} s^{-2}. Our observations are more robust and coincide with a stratification far greater, near $10^{-3.5}$ s^{-2}, and a MLD < 2 m. Such conditions might be conducive to a slippery diurnal jet (Kudryavtsev and Soloviev, 1990), a thin layer in contact with the surface at the base of which stratification is so strong that it slips over the water below with minimal friction. This jet is driven by increased shear caused by momentum trapped over a thinner layer, therefore causing more turbulence. Conditions during EQ14 were much windier with sustained speed beyond 6 m s $^{-}1$ and weak stratification. The temperature profile was more concave than exponential indicating the higher amount of wind induced mixing. On the three days illustrated on Figure 3.6, ϵ near the surface approximated wind scaling.

3.7. Relationships between wind stress, temperature gradient and ϵ

During DYNAMO legs2 and 3, dissipation was significantly higher (at the 95% confidence level) when ramps were present (Figure 3.7). During EQ14, ϵ was more intense than during DYNAMO and we noted only little difference in magnitude in the presence of ramps. The distribution of ϵ therefore did not correlate with the presence of ramps.

The background temperature gradient was much weaker and the winds stronger and more sustained. The existing turbulence at times of ramps might have be generated by shear instabilities, but Langmuir cells (visually observed during EQ14) were also expected to contribute to mixing and might create elevated turbulence without ramps.

With the large range of wind stress, temperature gradient, and turbulence measured in the three datasets, we can evaluate the relationship between these parameters in the upper 8-10 meters of the equatorial oceans. At times of higher winds, 0.035 N m^{-2}, T_z was weak and the relationship $\log_{10}\tau$ - $\log_{10}T_z$ was nearly identical in the presence or absence of ramps (Figure 3.8). At that speed, T_z decreased likely as a result of shear instabilities, Langmuir cells and wave breaking closer to the surface. The weaker wind stress tail end of the EQ14 dataset (blues, Figure 3.8) pointed to a diverging relationship around 0.025 N m^{-2} with "rampy" T_z higher than "nonrampy" T_z. During DYNAMO Leg2 (greens, Figure 3.8), the winds were only moderate and a clear distinction arose between times with temperature ramps and times with none. When ramps were present, the relationship between τ and T_z prolonged that suggested by EQ14, with T_z decreasing when winds increased. Without ramps however (dark green), T_z decreased as τ decreased. When winds are high and T_z is weak, shear instabilities are no longer the sole generator of turbulence and the "rampiness" does not designate a different regime. Leg3 confirmed this bisection of trends, rampy times (yellow, Figure 3.8) feature a high T_z for a low wind speed whereas non-rampy times (orange) had a weaker T_z comparable to that of Leg2 without ramps.

The relationship between τ and T_z was also reflected in ϵ. For low T_z from EQ14 (Figure 3.9, blues), a specific branch of increasing ϵ for decreasing T_z existed. Dissipation was higher when ramps were present. Leg2, in green, showed a remarkably opposite behavior based on the presence of ramps. When ramps were observed, ϵ followed the same trend as EQ14, decreasing with increasing T_z up to 0.1℃ m^{-1}, beyond which ϵ

increased for higher T_z. In the absence of ramps, however, ϵ decreased until T_z=-0.10℃ m^{-1} but then increased for greater T_z. Dissipation with or without ramps merged around T_z=-0.05℃ m^{-1}, and there was no discrimination in the presence ramps for increasing epsilon at higher T_z. Leg3 verified this pattern with a few differences. Ramps were detected at ϵ lower than any other dataset for T_z=-0.012℃ m^{-1}, and ϵ increased for increasing T_z regardless of the presence of ramps. The specific branches drawn by the relationship between T_z and ϵ might point to a need for different parameterization based on the wind and stratificaton regimes.

3.8. Summary

New observations from a bow-mounted fast thermistor chain deployed at the equator in the Indian ocean provided detailed time series of temperature in the top seven meters of the ocean under various regimes of wind and stratification. Fast temperature measurements permitted estimation of turbulence through fits to the Batchelor spectrum in the inertial subrange. The dissipation of TKE thus obtained followed the anticipated similarity scalings at night to within an order of magnitude, validating the technique.

The near surface dissipation followed a clear cycle governed by the TKE budget:

1. abrupt termination of nighttime convection by restratification of the surface from penetrating sunlight right after sunrise decreased ϵ at a rate proportional to $\epsilon = \mathcal{C}N\ e^{(-t/\tau_d)}$ where $\tau_d = (N\mathcal{C})^{-1}$. During this decay no distinct diurnal mixed layer existed, stratification was weak, and a nascent diurnal warm layer appeared.

2. following the morning minimum, ϵ then increased with the growing local stratification and was proportional to $\epsilon = \mathcal{C}N\ e^{(t/\tau_g)}$ where $\tau_g = \left(\left(\frac{u_*}{\kappa z} - (1+\Gamma)\mathcal{C}N\right)\right)^{-1}$. This growth period was observed above the mixed layer depth and coincided with the apparition of temperature ramps thought to be a signature of shear instabilities.

3. ϵ reached near steady state in the afternoon and was proportional to $\frac{1}{1+\Gamma}\frac{u_*^3}{\kappa z}$ in cases of moderately strong stratification.

When the mixed layer depth reset close to the surface, ϵ below decayed at the same rate as observed during restratification. ϵ overestimated Law-of-the-Wall scaling and steady state approximations in the presence of very shallow MLD (< 2 m) and strong buoyancy frequency ($10^{-3.5}$ s^{-2}), suggesting the presence of a diurnal jet. In conditions of strong wind and weak stratification, TKE dissipation was not significantly stronger in the presence of ramps, indicating either a failure to automatically detect ramps, or that ramps were not an indicator of turbulence in these conditions. Langmuir cells or wave breaking can generate turbulence in high wind conditions. A distinct relationship can be drawn between ϵ and temperature gradient, hinting at different regimes of turbulence in different wind conditions.

3.9. Acknowledgements

We are grateful to James B. Edson for sharing the meteorological and air-sea heat fluxes.

3.10. Figures

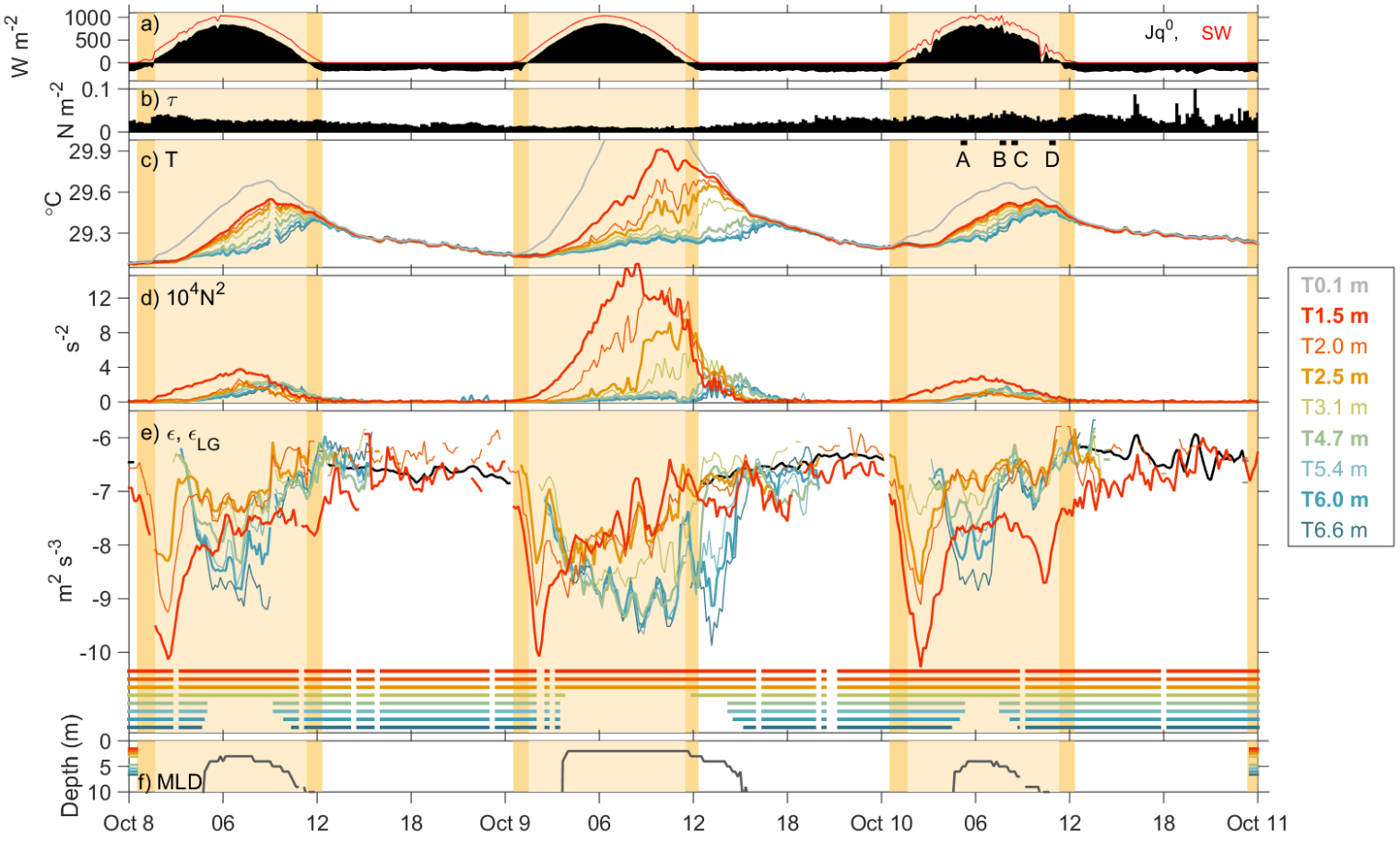

FIGURE 3.1: Time series illustrating the diurnal progression of ϵ and related variables. (a) Net surface heat flux J_q^0 (black) and short wave radiation (red), (b) wind stress, (c) Tpod temperatures (T0.1 in grey) , (d) buoyancy frequency $N^2 = g\alpha T_z$, (e) ϵ and the similarity scaling for nighttime dissipation, $1.76\epsilon_* + 0.58J_b^0$ (black), and (f) the mixed layer depth (grey) with side ticks indicating the depth of each sensor. The solid lines on panel (e) indicates the presence of each time series from panels (c)-(e) above the mixed layer depth plotted on (f). The vertical yellow bands mark times when the net surface heat flux is positive (warming), orange bands reflect the times when solar radiation is positive while J_q^0 is negative. Labels A-D on (c) mark times highlighted on Figure 3.4. The days depicted on this figure were chosen for their minimal disruption by advection therefore keeping the heat budget close to a one dimensional balance. Times with temperature gradient below threshold of -$10^{-3.1}$°C m^{-1} were removed.

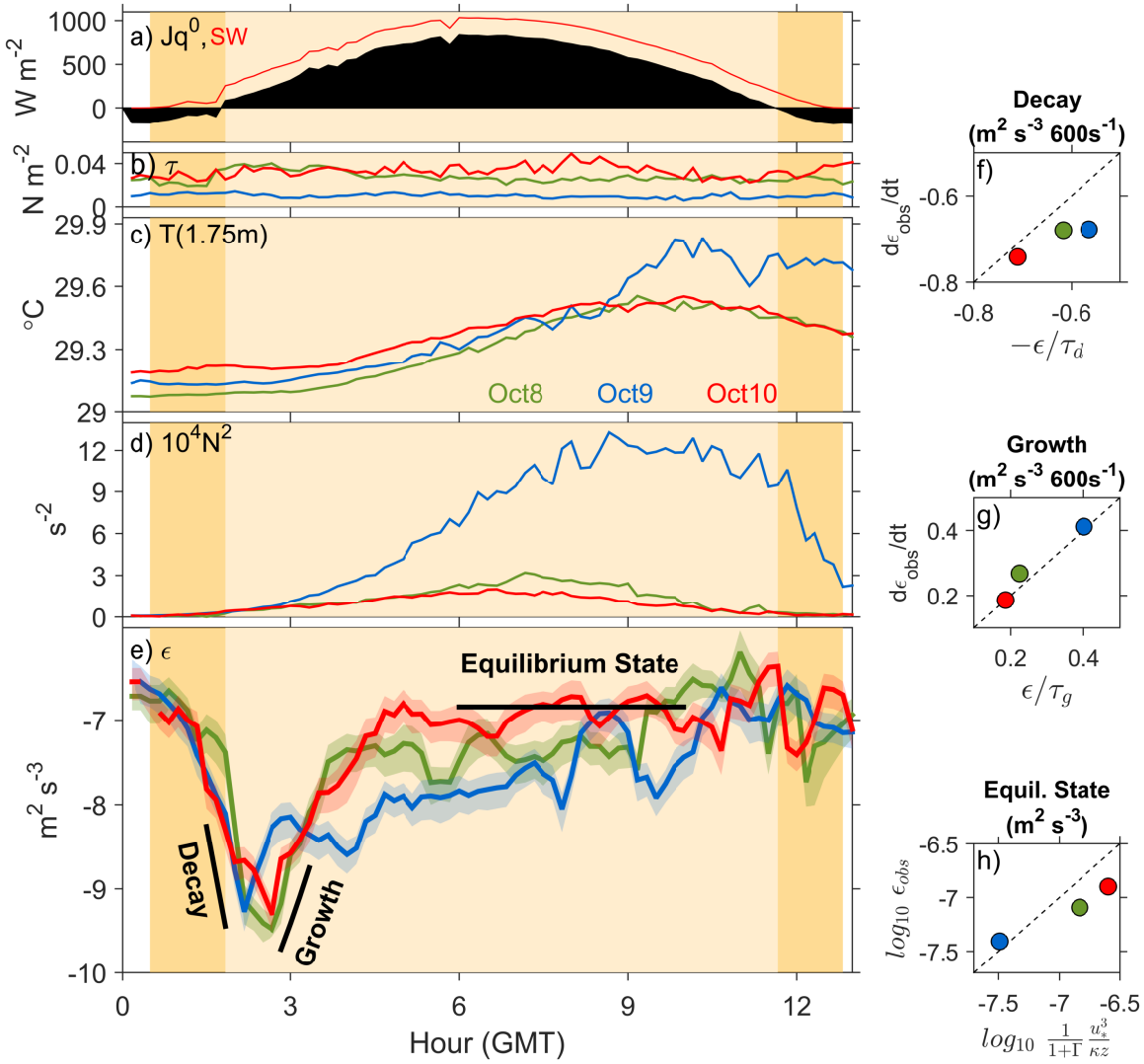

FIGURE 3.2: Detailed evolution and scaling of near surface ϵ and relevant variables averaged over 1.5 - 2.0 m. (a) Net surface heat flux (black) and incoming solar radiations (red), (b) wind stress, (c) temperature, (d) N^2, and (e) ϵ with 95% confidence limits. The 3-day average decay rate was calculated from equation 3.5 over the 1.6 hr preceding the morning minimum, the growth rate was computed from equation 3.7 over the 0.6 hr following the morning minimum, and the steady state magnitude was computed from equation 3.9 over 4 hours. The yellow vertical band mark positive net surface heat flux and the orange bands mark non zero short wave radiation. (f) estimated vs. observed decay rate of ϵ from days plotted on (e) with a 1:1 dash line, (g) same as (f) but for the growth rate, (h) ϵ from equilibrium state vs. observed. C_1 and C_2 are proportionality constants.

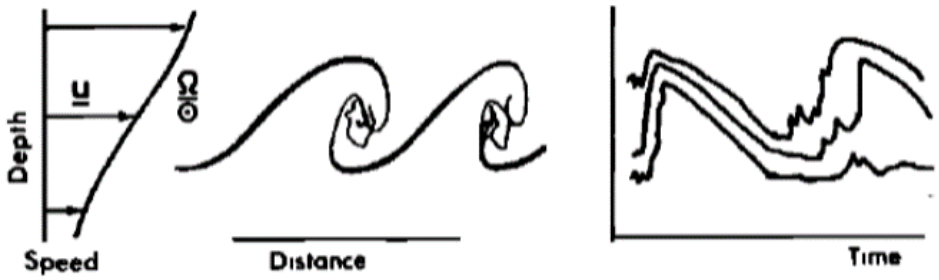

FIGURE 3.3: Excerpt from Figure 4 in Thorpe (1978) showing a schematic of a sheared current layer on the left, Kelvin-Helmholtz instabilities at center, and the resulting temperature time series observation sampled through the billow on the right.

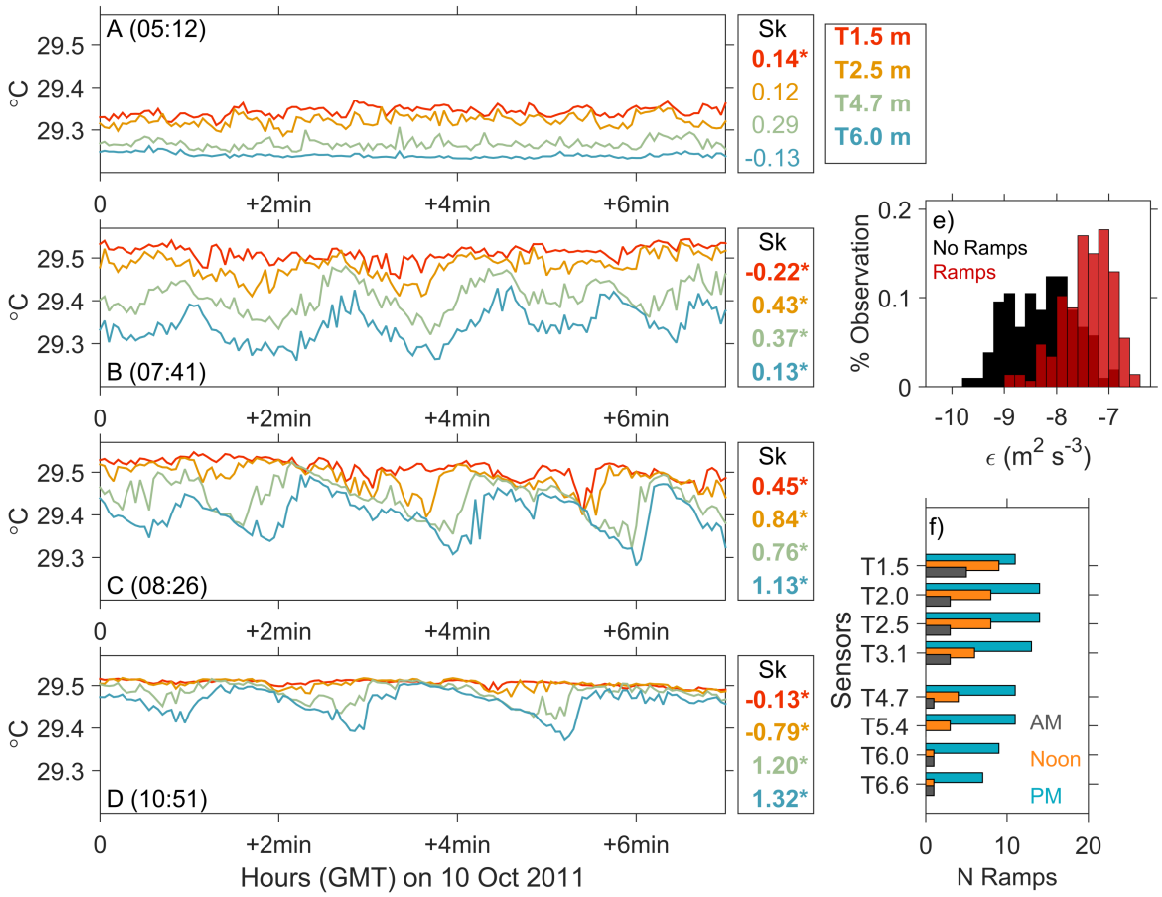

FIGURE 3.4: Evolution and details of temperature ramps on 10 October 2011 at four depths. (A-D) temperature low-passed at 30 sec, with start time in parenthesis and time increments on abscissa. The skewness for each time series is indicated on the panel immediately to the right. The skewness is followed by an asterisk if the automated algorithm selected this particular time series as featuring ramps, (e) Normalized distribution of ϵ in the presence of ramps (red, N=147) or without (black, N=105) during daytime. The Kolmogorov-Smirnov test confirmed a statistically significant difference between both distribution ($p \ll 10^{-4}$). (f) occurrence of ramps at each depth in the morning (03-05), at mid-day (06-07), and in the afternoon (08-10). The histograms were computed using all days from Leg2 which were not disrupted by freshwater lenses.

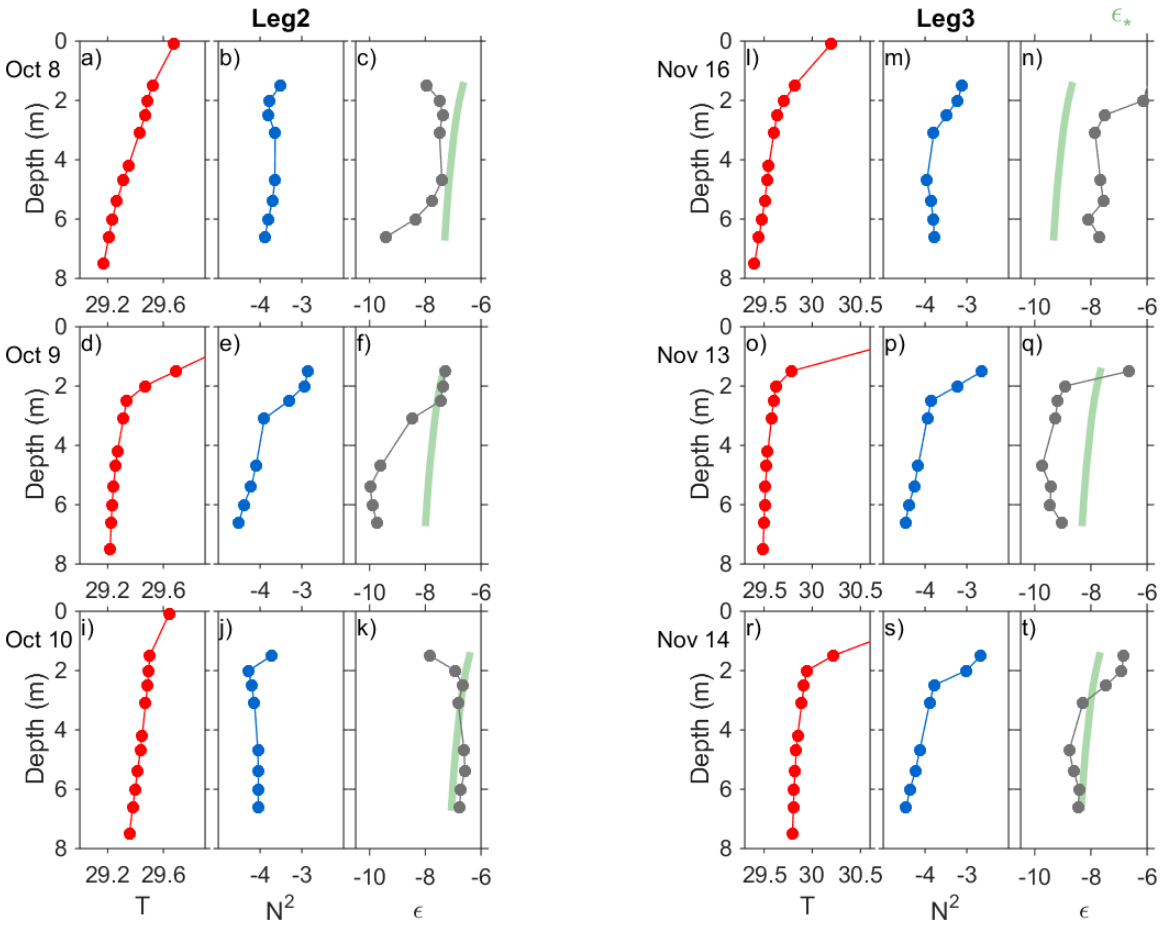

FIGURE 3.5: Hourly average profiles in mid afternoon of Temperature (red), buoyancy frequency (blue) and ϵ (grey) overlaid on Law-of-the-Wall scaling ϵ_* (green) for six individual days during Leg2 (a-k) and Leg3 (l-t).

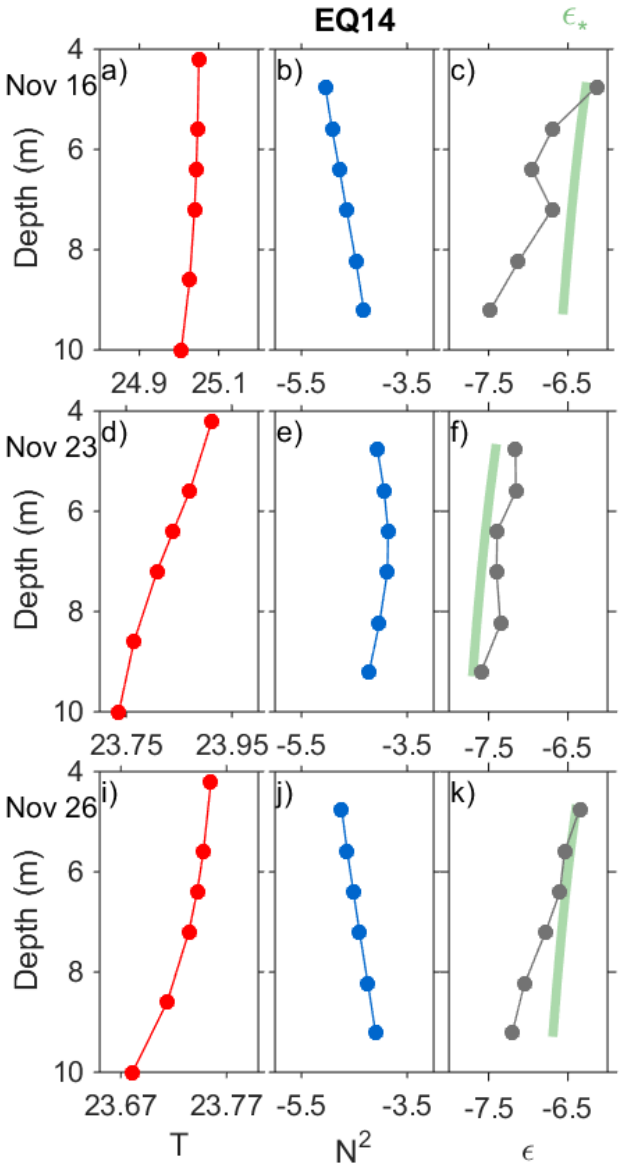

FIGURE 3.6: Hourly average profiles in mid afternoon of Temperature (red), buoyancy frequency (blue) and ϵ (grey) overlaid on Law-of-the-Wall scaling ϵ_* (green) for three individual days during EQ14.

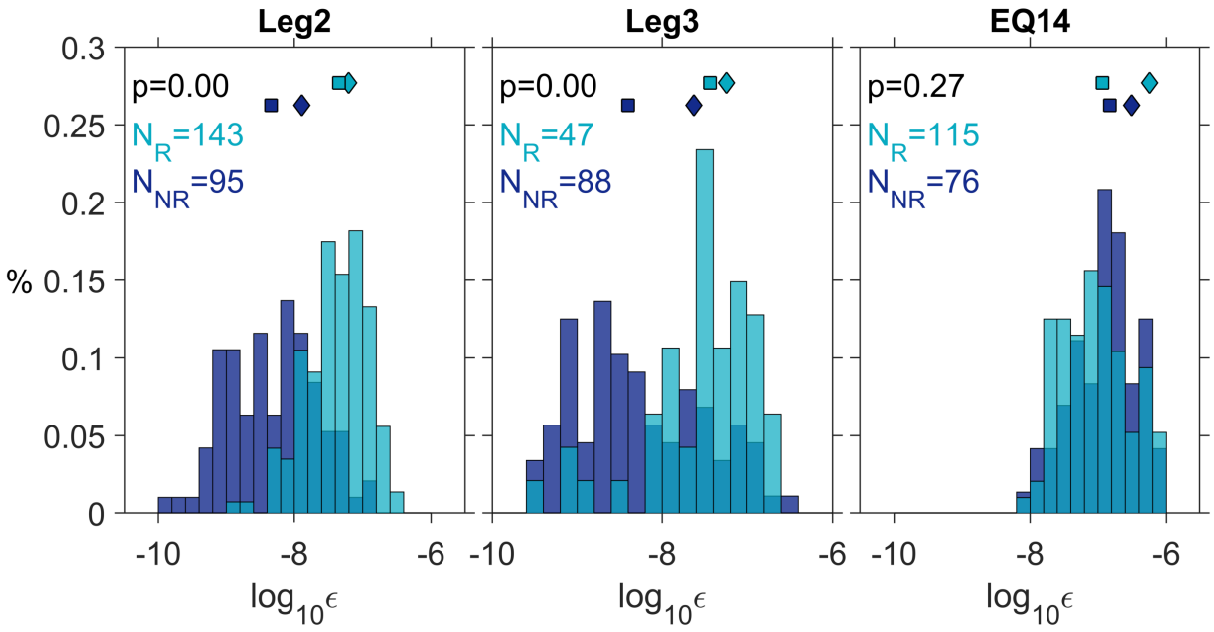

FIGURE 3.7: Probability density functions of ϵ when temperature ramps are observed (dark blue) and when they are not (light blue) during Leg 2 (left), Leg 3 (center) and EQ14 (right). Diamonds (squares) show the distribution mean (median). The distributions are significantly different to the 95% confidence level for a Kolmogorov-Smirnov p-value $<$ 0.01. The number of observation for each distribution is also indicated (N_R and N_{NR}).

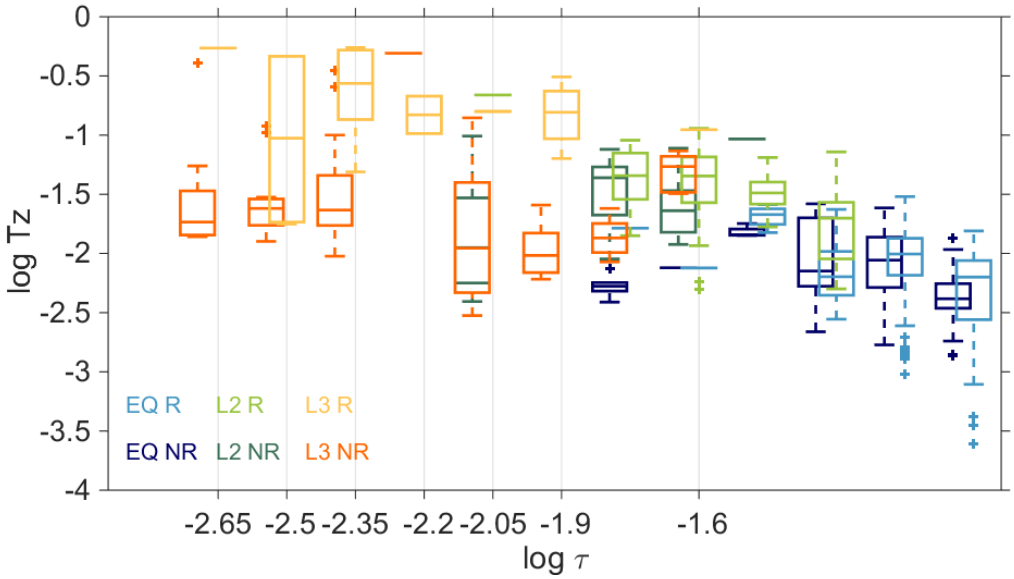

FIGURE 3.8: Boxplot of the $\log_{10}$ of temperature gradient T_z sorted according to the $\log_{10}$ of wind stress τ for Leg 2 (L2), Leg 3 (L3) and EQ14 (EQ) separated between times of ramps observations (R) and none (NR). The bar at the center of each box represents the median, the lower and upper edge of the box the 25th and 75th percentile respectively. The whiskers illustrate points outside the 25-75 percentile considered extreme. Individual markers show points considered outliers.

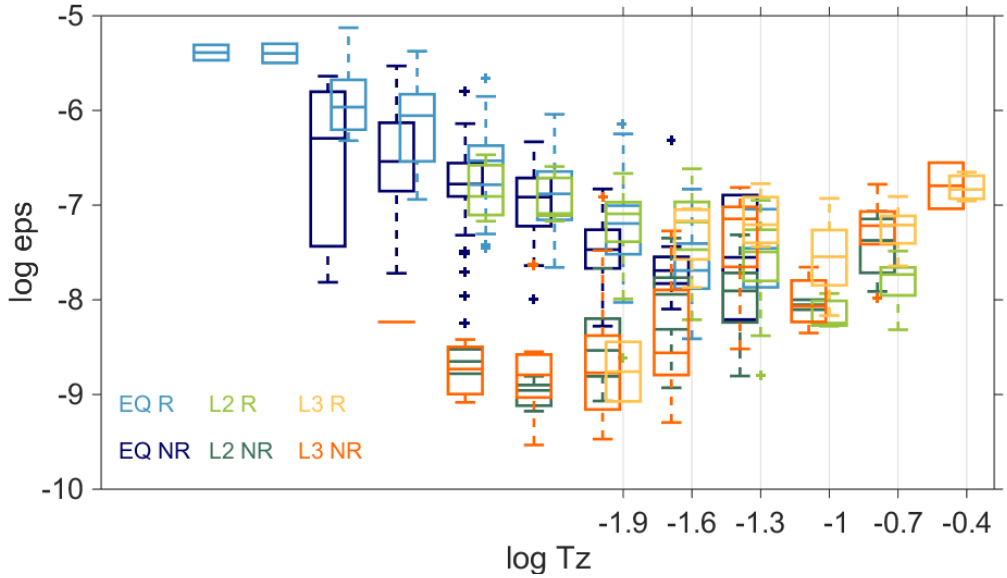

FIGURE 3.9: Boxplot of $\log_{10}\epsilon$ sorted according to the $\log_{10}$ of temperature gradient T_z for Leg2 (L2), Leg3 (L3) and EQ14 (EQ) separated between times of ramps observations (R) and none (NR). The bar at the center of each box represents the median, the lower and upper edge of the box the 25th and 75th percentile respectively. The whiskers illustrate points outside the 25-75 percentile considered extreme. Individual markers show points considered outliers.

Spatio-temporal evolution of temperature in the diurnal warm layer

Aurélie J. Moulin, James N. Moum, and Emily L. Shroyer

4. SPATIAL AND TEMPORAL EVOLUTION OF THE DIURNAL WARM LAYER

4.1. Abstract

Neglecting advective effects, the diurnal warm layer represents a balance between the net surface heat flux, penetrating solar radiations and vertical mixing. Typically, the latter two terms are parameterized and the relative influence of each is hard to isolate due to measurement uncertainties. The high temporal and spatial resolution of subsurface temperature and turbulence measurements, augmented with air-sea heat fluxes, offered a new look into the formation and collapse of the diurnal warm layer. These measurements also permitted a re-assessment of warm layer models for temperature structure and heat content. DWL formation was initiated upon sunrise when the termination of nighttime convection transported small amounts of heat downward as turbulence decayed. Heat continued to be transported downward until complete restratification near the surface. After that time, the heat near the surface accumulated with a vertical exponential decay and exceeded the local divergence of solar absorption as turbulence mixed warm water from above. Further down, absorbed solar radiations were the sole contributor to heat gain. The DWL collapse was initiated mid afternoon when net surface cooling from latent, sensible, and radiative heat exceeded the local divergence of absorbed solar radiations. As the surface became weakly stratified, warm water from above was mixed down by daytime turbulence. The heat that had been accumulated in the DWL thus far was then eroded both from above as surface cooling dissipated heat at the surface, and from below through shear instabilities at the base of the mixed layer. PWP and COARE3.5 typically underestimated sea surface temperature and demonstrated weaknesses at reproducing the time-varying heat content over the top five meters.

4.2. Introduction

When the heat budget is mainly one dimensional and no barrier layer or freshwater lenses are present, nighttime convective mixing disperses any heat that was accumulated over the previous day. Upon sunrise a new heating cycle can thence start on a blank slate. Heat deposited at the ocean's surface by the sun may be mixed deep in the ocean's interior, may linger relatively close to the surface, or may return to the atmosphere through air-sea interactions. Reconciling the heat budget is key to track the fate of the oceanic heat content and to improve parameterizations.

4.2.1 Brief history of research on the diurnal warm layer formation

The climatological importance of the diurnal warm layer has been known for the past 40 years (Stommel et al., 1969; Woods, 1968; Simpson and Dickey, 1981; Price et al., 1986). Modeling efforts to include their parameterization in larger ocean models have been successful at reproducing basic mechanisms. Elements of understanding of the DWL came from Noh (1996) who looked into the thickness of the diurnal thermocline at the base of the DWL and explained its formation as a balance between shear and buoyancy production. Brainerd and Gregg (1993a) provided key elements of the diurnal warm layer formation by looking at restratification. Other elements were provided by studies on the irradiance profiles such as Lewis et al. (1990). Major advances were further provided from the Tropic Heat and TOGA-COARE field experiments.

New observations of the DWL were recently made in the Indian Ocean during the DYNAMO campaign. More statistics were offered, such as daily mean SST warm anomalies of 0.2℃ up to 0.8℃ between the surface and 10 meters below, or the prevalance of high sea surface temperature during MJO's suppressed convective phase (Matthews et al., 2014).

4.2.2 Elements of the Heat Budget

The one-dimensional heat budget is expressed as

$$\rho C_p \int_0^h \frac{\partial T}{\partial t} dz = J_q^0 - I_h - J_q^h \tag{4.1}$$

where ρ is water density (kg m^{-3}), C_p the heat capacity of sea water (J kg^{-1} ℃$^{-1}$), J_q^0 the net surface heat flux (W m^{-2}), I_h the transmitted solar radiation (W m^{-2}), and J_q^h the turbulent heat flux (W m^{-2}).

The net surface heat flux is a balance between the downwelling shortwave and longwave solar radiation, against the latent, sensible, and radiative cooling fluxes. A portion of the radiation hitting the surface, the albedo, is reflected to the atmosphere. This quantity is typically about 5% of incoming sunrays at midday and low latitudes (Payne, 1972; Katsaros et al., 1985). The remaining absorbed solar radiation (ASR) follows an exponential profile governed by the transmission of solar radiation. This downward attenuation of solar radiation is affected by the sun angle, the cloud index which changes the intensity and spectral composition of sunrays, and by the clarity of ocean water (Ohlmann et al., 2000). The turbulent heat flux is the result of turbulent mixing working to diffuse heat.

These elements are known to various degrees of accuracy. Incoming solar radiation and net surface cooling are deemed very accurate, and so is the measured heat content since it relies on direct observations. The profile of solar attenuation is difficult to measure, especially in the top five meters (C. Ohlmann, pers. communication). Yet this is the depth range where 50% of shortwave radiation is absorbed where it is known to be inaccurate. The turbulent heat flux is responsible for distributing the heat sources and sinks from the atmosphere.

4.2.3 Overview of two popular diurnal warm layer parameterizations

Modeling efforts to include DWL parameterization in larger ocean model have been successful at reproducing basic elements. These models include Price-Weller-Pinkel (PWP), Profile-of-Ocean-Surface-Heating (POSH), K-Profile-Parameterization (KPP), or General-Ocean-Turbulence-Model (GOTM) to name a few. Other modeling efforts were concentrated on estimating the sea surface temperature to quantify heat fluxes, like the COARE algorithm. Two of these popular diurnal warm layer models were chosen to assess performance and identify possible means of improvement based on their functioning details and ease of use.

The Price - Weller - Pinkel model (PWP)

PWP was developed to model the structure of temperature (T), salinity (S), density (ρ), and velocity in upper ocean mixed layer. It was first tested against observations with moderate winds (4 - 7 m s^{-1}) and strong insolation with data collected offshore southern California (Price et al., 1986). It is initialized with a temperature, salinity, and velocity profile and modified by the addition of time-varying forcings, namely sensible, latent, and rain-induced cooling as well as internal warming from shortwave solar radiation attenuated with depth. After an adjustment of static instabilities, the mixed layer depth (MLD) is evaluated as the depth where the local density gradient exceeds the surface gradient by 0.01 kg m^{-3}. Wind stress is then applied at the surface, and the MLD deepens through a bulk Richardson number adjustment to simulate dynamical instabilities in the mixed layer (ML), and a gradient Richardson number to simulate entrainment at the base of the ML.

The COARE3.5 algorithm

The COARE algorithm was developed following the TOGA-COARE (Tropical Ocean Global Atmosphere Coupled Ocean Atmosphere Response Experiment) field experiment in the early 1990s. Its primary goal was to model air-sea fluxes of heat and moisture from time series of wind, air temperature, humidity, and solar radiations (Fairall et al., 1996a,b, 2003). It was then augmented with a warm layer module to better estimate the sea surface temperature (SST), a critical parameter in quantifying air-sea fluxes. To do so it parametrizes a cool skin correction caused by latent, sensible, and radiative cooling at the surface, and a warm layer correction to be applied to a temperature time series measured at some shallow depth. The warm layer correction is a byproduct of absorbed solar radiation and net surface heat flux linearly distributed over a depth determined by a bulk Richardson number. This distribution leads to a linear temperature gradient between the estimated depth of the mixed layer and the surface. The warm layer correction can then be estimated from the temperature and depth of a measured time series.

We aim at diagnosing the performance of PWP and COARE3.5 (Section 4.4.) before detailing observation of the diurnal warm layer formation (Section 4.5.) and collapse (Section 4.6.). Suggestions for parametrizations improvements are offered with a discussion (Section 4.7.) followed by a summary (Section 4.8.).

4.3. Methods

4.3.1 Data

The data used therein were collected during the DYNAMO field project from a thermistor chain (T-chain) deployed at the bow of the R/V Revelle (Section 2.1.1). Mixing estimates were derived by regressing spatial temperature spectrum onto the Batchelor spectrum in the inertial subrange of turbulence (Section 2.5.).

4.3.2 Computation of Heat budget terms

The terms of the heat budget equations were computed as follow.

$$Heat\ content : H_t = \rho C_p \frac{\partial T}{\partial t} \Delta z \ \ [Wm^{-2}] \tag{4.2}$$

$$Transmitted\ solar\ radiation : I_h = Solar * Tr(h) \ \ [Wm^{-2}] \tag{4.3}$$

$$Turbulent\ Heat\ Flux : J_q^h = \rho C_p K_T T_z \ \ [Wm^{-2}] \tag{4.4}$$

where ρ is the density, C_p the heat capacity of water, Δz is the separation between two sensors, Solar is the downwelling solar radiation, Tr(h) is the attenuation coefficient at depth h, and K_T is temperature eddy diffusivity.

4.4. Performance of PWP and COARE3.5

The diurnal warm layer is the near surface region where the heat content has been modified by solar radiation, net surface heat fluxes, and mixing, and is easily seen on temperature image plots (Figure 4.1). The addition of heat at the surface combined with weak to moderate winds confined warm temperature near the surface and caused the mixed layer depth to shoal mid morning, progressively deepen for the rest of the daytime and into the night.

The MLD defined the depth above which water properties are well mixed. Its location is controlled by physical processes and determines the shape of a temperature profile. An inaccurate temperature profile therefore highlights weaknesses in models. The range of MLD obtained by various avenues is shown on Figure 4.2. MLD evaluated from density is best but the Chameleon being in the ship's wake, $\mathrm{MLD}_{Chameleon}$ was

overestimated. MLD from T-chain temperature data provided a more accurate estimate when the density field was mostly influenced by temperature, but limited the depth range to the upper 8 meters. Merging T-chain with Chameleon data below 8 meters permitted to evaluate MLD from temperature over a deeper range. $\mathrm{MLD}_{T-chain}$ should be more representative of the mixed layer depth at times without significant salt stratification.

Two characteristic profile shapes dominated equatorial regions: exponential (Figure 4.3C-D) and hyperbolic tangent (tanh, Figure 4.3A-B). PWP was unable to reproduce either of these shapes accurately (Figure 4.3). More than simply shapes, both PWP and COARE3.5 underestimated SST (Figure 4.4). COARE3.5 performed much better than PWP, perhaps due to the temperature forcing. The depth of this input temperature time series did have an effect on the magnitude of SST anomaly in COARE3.5. For input time series below 1 m COARE3.5 underestimated SST during the day and overestimated SST at night (Figure 4.5b). The trend was mostly reversed when forced with a temperature time series above 1 m. PWP underestimated SST by up to 0.5 ℃ during days with low winds. It performed well below 1 m during daytime in moderate winds, overestimated temperature in low winds, and always underestimated temperature in early evening at all depths.

COARE3.5 inaccuracies were mostly rooted in its assumption of a linear temperature profile. PWP errors were likely caused by the mixing parameterization not distributing sufficient heat in early evening. Both models were affected by inaccuracies of solar transmission profiles and albedo.

Figure 4.3 showed that PWP was not resolving the profile shape very well. A simple fit of exponential and tanh profiles to observed profile showed that exponential fit errors were greater in late afternoon and early evening while tanh fit errors were greater mid morning until late afternoon. Although intuitive, this may suggest a path toward improving parameterization by indicating times when certain physical processes

were more prevalent. The overall mechanisms of heat accumulation and dissipation are known (Price et al., 1986), but possible improvements could be made by detailing these processes (see further discussion in section 4.7.2).

4.5. Diurnal warm layer formation

4.5.1 Restratification in moderate winds

After sunrise, absorbed solar radiation are able to warm the subsurface upper ocean. While it was still early and solar radiation and net surface heat flux were weak, observed temperature was warmer than predicted by penetrating sunlight at all depths (Figure 4.7c). In addition, the temperature contours were vertical, a sign that stratification remained weak. Between 0130 - 0200 turbulence decayed significantly while the difference between observed and radiative temperature increased. Brainerd and Gregg (1993a) mentioned the ability of decaying eddies to transport surface heat down until restratification had fully occurred. Our observations support this theory.

At T1.5, a heat deficit appeared around 0230 and persisted until about 0600 (Figure 4.7c). This implied an export of heat locally deposited by attenuated sun rays. Between T2.0 and T3.1 however, the deficit only existed until 0400, after which time an excess developed. Interpreting the difference between observed and radiative heat as an indication of mixing, this surplus of heat corroborated trends observed in temperature variance dissipation, χ (Figure 4.7d). Observed χ remained homogeneous across all depths until about 0400. It then diverged: shallow χ increased while deeper it decreased. This also coincided with the development of oscillation in low-passed temperature contours.

At approximately 0400 on 08 October the water column effectively restratified, accumulating heat and shear above as indicated by temperature contour oscillations and

excess heat near the surface. Turbulence decayed between 0400 - 0530 at T6.0, and after 0600 temperature changes at 6 meters and below were mostly explained by radiative heat. Above, the excess heat had been mixed down from the near-surface where the exponential decay of solar radiation accumulated the bulk of heat.

The importance of this observation, not unique to 08 October 2011, is that heat from the sun was not homogeneously deposited with time. It was originally exponentially distributed due to the exponential decay of solar absorption, a fact that has been known at least since the early 1970s. Decaying eddies transported this heat down early - mid morning (Brainerd and Gregg, 1993a). After full restratification, the heat content above the stratified depth was modulated by turbulent heat flux driven by shear instabilities and importing heat from above, bringing heat in excess of local sources. Below, the heat deposited close to the surface was not transported by turbulence and remained above in the mixed layer. It was not communicated below as the shear was trapped at the bottom of the mixed layer thereby creating a barrier. At these deeper depths the heat was entirely due to absorbed solar radiation.

4.5.2 Restratification in low wind

When winds are weak it takes longer for the restratified surface layer to descend to 1.5 m, the depth of our shallowest mixing measurement where we can observed χ. We know from Figure 3.1 that ϵ had already started to markedly decay by 0100. It was therefore restratified above and this was reflected in the temperature anomalies on Figure 4.8 where the observed temperature was nearly explained by radiative heat. Since no turbulence were present, no heat from above was transported and no excess heat was observed. Temperature contours were closer together above 2 m, stratification was more intense, heat was exported from the very surface to T1.5 where there was excess heat. But Figure 4.8c suggests that there was a deficit of heat between 2 - 4 meters most of the

morning. Given the strong stratification above and the stable stratification from absorbed solar radiation it seems unlikely that mixing could explain this deficit. The temperature derived from absorbed solar radiation rely on the solar transmission profile which is known to be inaccurate above 5 meters (Ohlmann et al., 2000). This might explain at least part of this deficit, and would also suggest that the heat excess observed on 08 October (Figure 4.7) might be underestimated.

4.6. Collapse of the diurnal warm layer in early evening

4.6.1 Collapse in moderate winds

The descending phase of the sun in the afternoon ideally provides the same amount of heat than the ascending phase in the morning. The difference in the afternoon is that the ocean no longer is a blank slate with heat freely accumulating throughout. Peak heat at the very surface is achieved when the sun is at the zenith, solar radiation is a maximum and albedo a minimum. Net cooling at the surface remains nearly constant when the wind speed does not vary. At some time afternoon, net radiative heating no longer exceeds net surface cooling. From that moment forward, the ocean surface is being cooled from above.

Because of the exponential profile of radiant heating, the onset of local cooling is progressively later with depth (Figure 4.9a). At T0.1 on 18 October local radiative heating neared zero at 0800 and effectively became negative at 0830 when the cooling onset at T0.1 was expected. This cooling however started around 0730, another possible indication of the inaccuracy of the solar transmission profile (or of the depth of T0.1). It might seem counter intuitive that at 1430 local time, the sea surface temperature started cooling since the afternoon heat remained strong, but the balance of exponential radiative heating and net surface cooling was such that there already was a local divergence of heat in mid-afternoon at these shallow depths.

While T0.1 started to cool, between 0730 - 0900, T1.5 stopped warming, temperature variance dissipation stopped increasing, heat excess plateaued, and temperature contours flattened (Figure 4.9). No additional heat was received from above. Over the same time period, deeper temperatures warmed significantly, χ increased, the nearly balanced heat divergence of observed and radiant heat turned into an excess, and temperature contours displayed high frequencies oscillations. These are all signs of surface heat mixed down by turbulence as the mixed layer deepened from shear instabilities. Distinct warming was measured at T2.5 and above, between 0930 - 1030, a period when net cooling at 0.1 m increased. We hypothesize that this was caused by the mixing of warmer water from above, as the surface became unstable. Shortly after 1030 all sensors experience net cooling (Figure 4.9a). Temperature decreased shortly after. At the surface, a deficit of heat was observed starting around 1030 and increased thereafter. More heat was mixed down than was deposited by absorbed solar radiation. This coincided with the time when the net local heat flux became negative. The sun set around 1200 after which any temperature changes observed were solely caused by mixing (neglecting advection). This heat deficit progressed down with time to reach 3 m by 1300. Below 3 meters however, the peak heat surplus occurred around 1000 and decreased thereafter. An hour after sunset heat remained below 3 meter that had been mixed down from above earlier. The temperature structure collapsed around sunset when the net local heating at all depths was zero. Temperature uniformly cooled thereafter.

4.6.2 Collapse in low winds

The same observation can be made about 09 October 2011 (Figure 4.10) although some differences in timing and structure exist. The net local heat flux turned negative at 0.1, 1.5, and 6.0 meters at about the same time as on 18 October. However, owing to the weakness of wind-driven mixing, most of the heat was still confined near the surface: the

temperature difference between T0.1 and T1.5 reached 0.5℃ , the temperature gradient was strong in the top 3 meters and weak below 4 meters, and there was a high excess of heat above 3 meters while the difference observation - radiant heat was nearly balanced below 4 meters. T0.1 featured its peak temperature around 1000. By 1100 all sensors experienced destabilizing net local cooling, entraining warm water from above as already observed on 18 October, although happening one hour later on 09 October.

It is only at 1600 that heat from above reached 6.6 meters, 4 hours after sunset (at 2200 local time) and only at 2200 (0400 local time) that the heat from the previous solar cycle was effectively mixed out of the top 6.6 meters. During the entire solar cycle that day, the heat content at 6.6 m was entirely explained by local radiant heating. The heat exponentially added at the surface remained near the surface, was not mixed with cooler water from below until late night, resulting is much warmer sea surface temperature.

4.7. Discussion

4.7.1 Vertical heat distribution

Looking at patterns of heat excess and deficit in concert with the distribution of turbulence refines our understanding of downward heat transport throughout the day. Figures 4.11 summarizes the trends in heat and turbulence discussed throughout this paper. The role of mixing and shallow mixed layer depth in deistributing heat is illustrated on by the divergence of temperature between observation and radiant internal heating on Figure 4.12. The areas with a heat surplus were directly influenced by mixing, which carried down warm water from above during the peak heating period of the day, mixing it with cooler water from below thereby deepening the mixed layer. At the surface in late afternoon and early evening, increased continued mixing exported more heat than what

short wave radiation has deposited.

Profiles of heat budget reflected the decoupling between the region within the mixed layer and the region below. At 0200, integrating heat from the surface lead to an underestimate of the heat content at each sensor by 10-50 W m^{-2} (Figures 4.13b and 4.14b). Local heat derived from absorbed solar radiation is a good estimate, as previously discussed. From peak insolation onward, stratification determined the vertical distribution of heat. With moderate winds (08 October, Figure 4.13), local heat divergence was a good indicator while integrating from the surface was not. Observed and estimated heat content at T0.1 were large (off scale on Figure 4.13) but immediately below less heat was present than if it had been distributed vertically. What is interesting about Figure 4.13c is that the heat content is not well approximated by depth averages within the mixed layer when it is the scheme used by PWP. This points to the clear role of mixing in modulating the vertical distribution of heat.

By 0900, mixing had continued to cool surface temperature, and the integrated heat profile was affected over the total depth range.

In low wind conditions, both total depth and local integration yielded good heat content estimates at peak insolation. In mid afternoon the local heat content reconciled the locally absorbed solar radiation a few meters below the MLD but an integration from the surface again led to large overestimates of heat content.

4.7.2 Shortcomings of models and paths toward improvements

The accuracy of modeled MLD over a diurnal cycle influences SST greatly by redistributing the exponential heat. Models reproduce the DWL by estimating the MLD from external forcings and then mixing quantities above it. The diffuse warming early in the day throughout the water column may not be represented. Restratification observations in moderate winds showed a termination of convective mixing and subsequent decay,

then followed by a rapid growth of turbulence. As these processes unfolded, heat was carried down in excess of internal solar heating. The PWP parameterization for the onset of the DWL is meant to find the depth at which internal heating equals surface cooling (Compensation depth, Fairall et al. (1996a)), mix all quantities above, and if wind-driven momentum had been accumulated, it then mixes further through Richardson number criterion. This sequence of events seem realistic but did not reproduce the early morning downwelling of heat. The direct consequence was a MLD that shoaled to the compensation depth shortly after sunrise rather than mid-morning (Figure 4.2). This might be improved by considering a time varying Richardson number criterium. COARE3.5 also reset the depth of the warm layer too early, possibly because it first assumed the same compensation depth as PWP before modifying its value.

PWP reproduced the deepening of the MLD fairly well, both in timing and rate. COARE3.5 did well in low wind conditions but deepened too early and too quickly (Figure 4.2) in moderate winds. These discrepancies would imply a heat deficit in models, which is true for the SST estimate from COARE3.5 during the day, and for both surface and subsurface PWP modeled T in moderate wind conditions. In low wind conditions, PWP MLD was too shallow and led to a heat surplus. Decreasing the vertical resolution in PWP could lead to better results but there are limitations for computational stability. The use of a staggered grid could maintain the moderate spacing and we may be able to use differences between each of the staggered grids to refine T outputs.

The mechanisms responsible for DWL collapse should already exist in current parameterizations. However evening accuracy builds on errors previously accumulated in heat and MLD. In moderate wind conditions, PWP did well while COARE3.5 showed a greater deviation from observation, which could be expected given the weaker mixing parameterization it employs.

4.8. Summary

After being reset overnight by convective mixing, the diurnal warm layer started anew every morning. After sunrise and until complete restratification occurred, heat deposited at the surface was carried downward by decaying eddies bringing heat in excess of the local divergence of radiative heating. Complete restratification was achieved when turbulence at the top and bottom of the surface layer became decoupled mid-morning: it increased above and decayed below. Turbulence was therefore a good indicator of the mixed layer depth. After this restratification, the bulk of the heat accumulated near the surface remained confined above the mixed layer depth. This created an excess of heat in the mixed layer compared to the local radiative source. Below the mixed layer, the temperature was completely explained by the local divergence if radiative heating.

The DWL collapse was initiated at the surface when the local heat balance between net surface cooling and the divergence of absorbed solar radiation turned negative. This happened as early as 1430 local time. As the sun became lower over the horizon and radiation intensity decreased, the depth where cooling compensated heating deepened, relaxing the strong buoyancy closer to the surface and allowing warm surface water to mix down. This often created a minor heating burst of a few hundredths of a degrees below T0.1.

PWP and COARE3.5 overall do a fine job at modeling surface heat content but a few features of the DWL were missing when compared to observations. SST was often underestimated and the vertical distribution of heat was not responding quickly enough to temporal changes of profile shapes. In the morning, the MLD was reset near the surface too early preventing heat from being distributed deeper. In the afternoon, PWP reproduced well the timing and rate of deepening of the MLD while COARE3.5 started too early.

A simple balance between internal heating and observed heat content illustrated times when the local heat balance resulted mostly from the local divergence of solar absorption or when it resulted from the total heat content over the mixed layer above. This seemed affected by wind speed. Since PWP mixes away water properties above a mixed layer depth it defines, this will likely create errors in heat content when it is driven mostly by local solar divergence.

4.9. Acknowledgements

We are grateful to James B. Edson for sharing the meteorological and air-sea heat fluxes and providing a copy of the COARE3.5 algorithm. Tom Farrar provided PWP and Carter Ohlmann provided profiles of solar radiation attenuation.

4.10. Tables and Figures

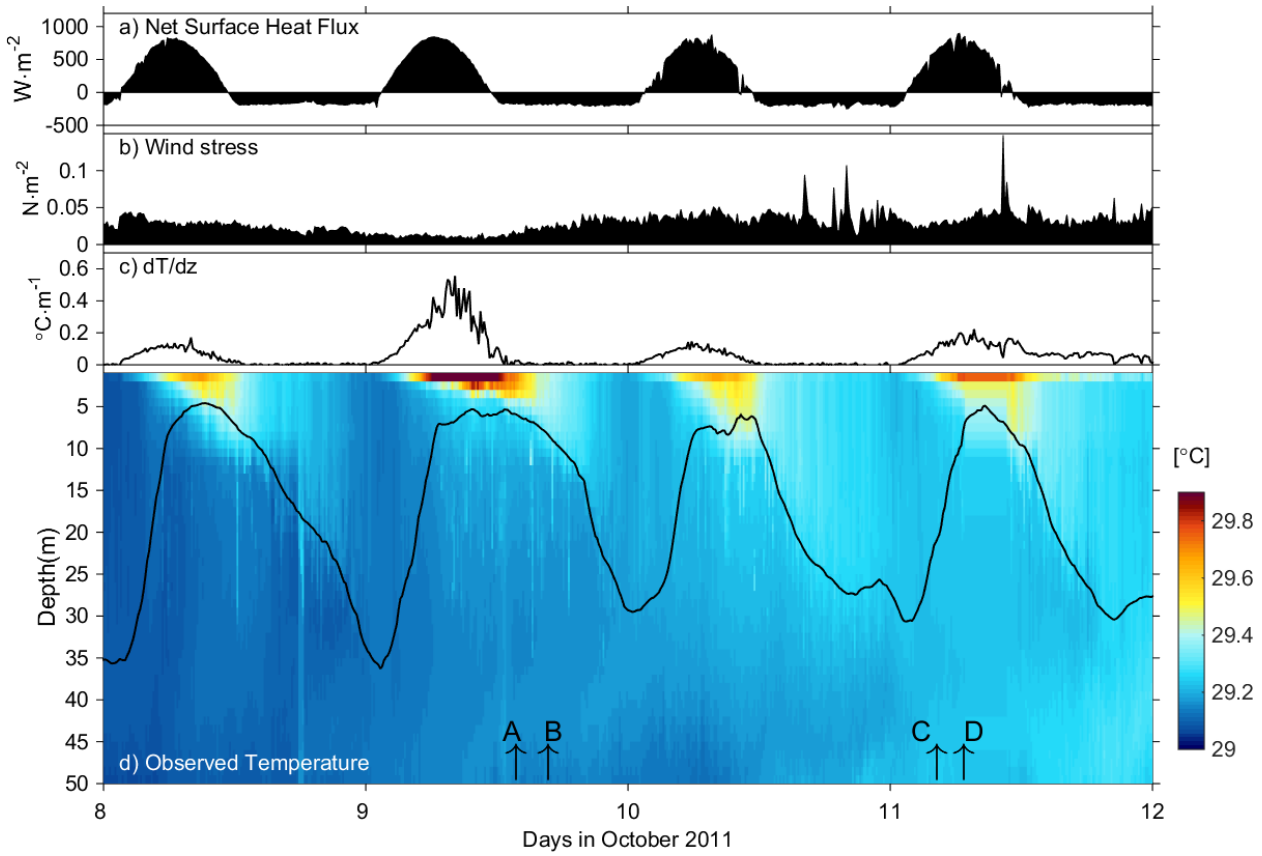

FIGURE 4.1: Air and ocean variables during four days illustrate the evolution of the diurnal warm layer. (a) Net surface heat flux J_q^0, (b) wind stress, (c) temperature gradient over the top 1.5 m, (d) temperature in color overlaid with the mixed layer depth in black. Letters A-D and arrows mark times of temperature profiles illustrated on Figure 4.3.

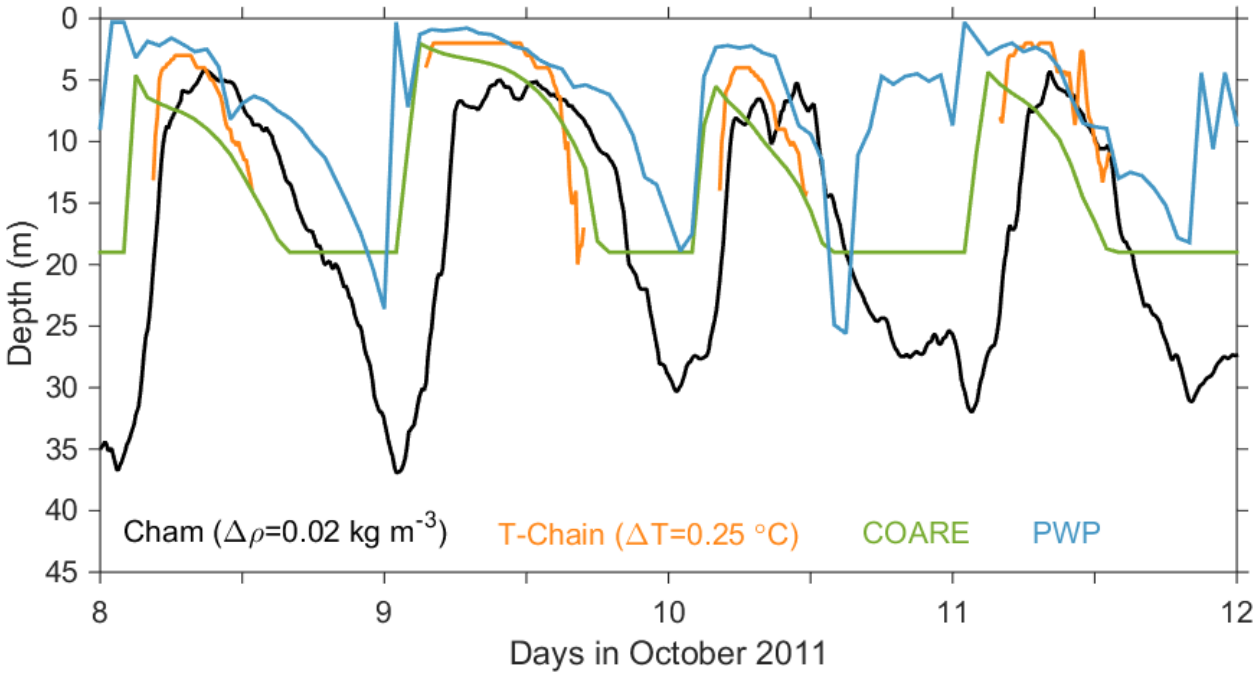

FIGURE 4.2: Mixed layer depth evaluated from various criteria: from density threshhold applied to Chameleon (black), from a temperature threshold applied to T-chain temperature data merged with Chameleon temperature data between 8-20 m (orange), and evaluated by COARE3.5 forced by T1.5 (green) and by PWP (blue). The particular thresholds were chosen to fit the data best.

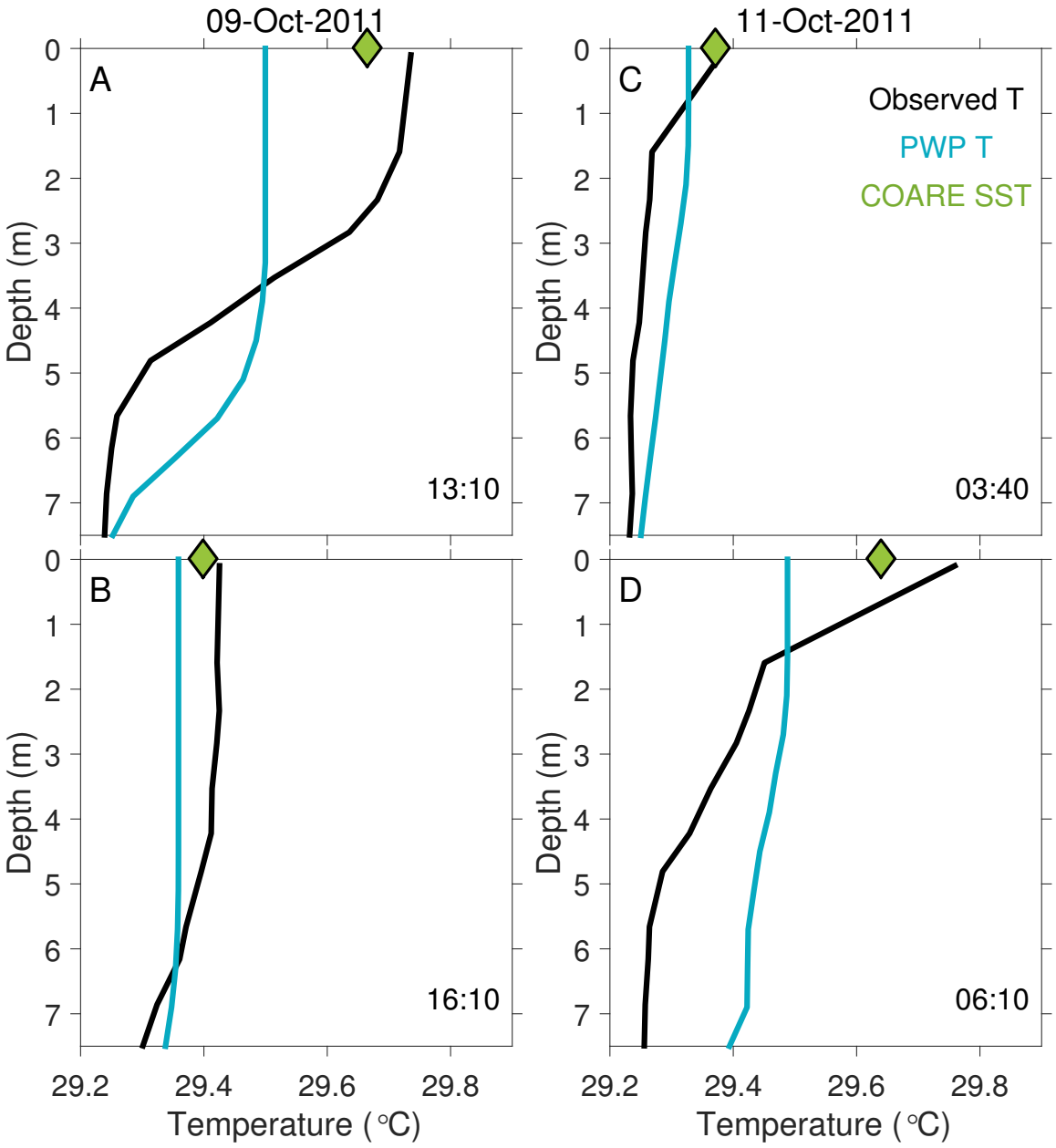

FIGURE 4.3: Performance of PWP and COARE at reproducing observed temperature profile and sea surface temperature in different heating conditions. COARE3.5 was forced with a temperature time series measured at 1.5 m. Letters A-D mark times of temperature profiles illustrated on Figure 4.1.

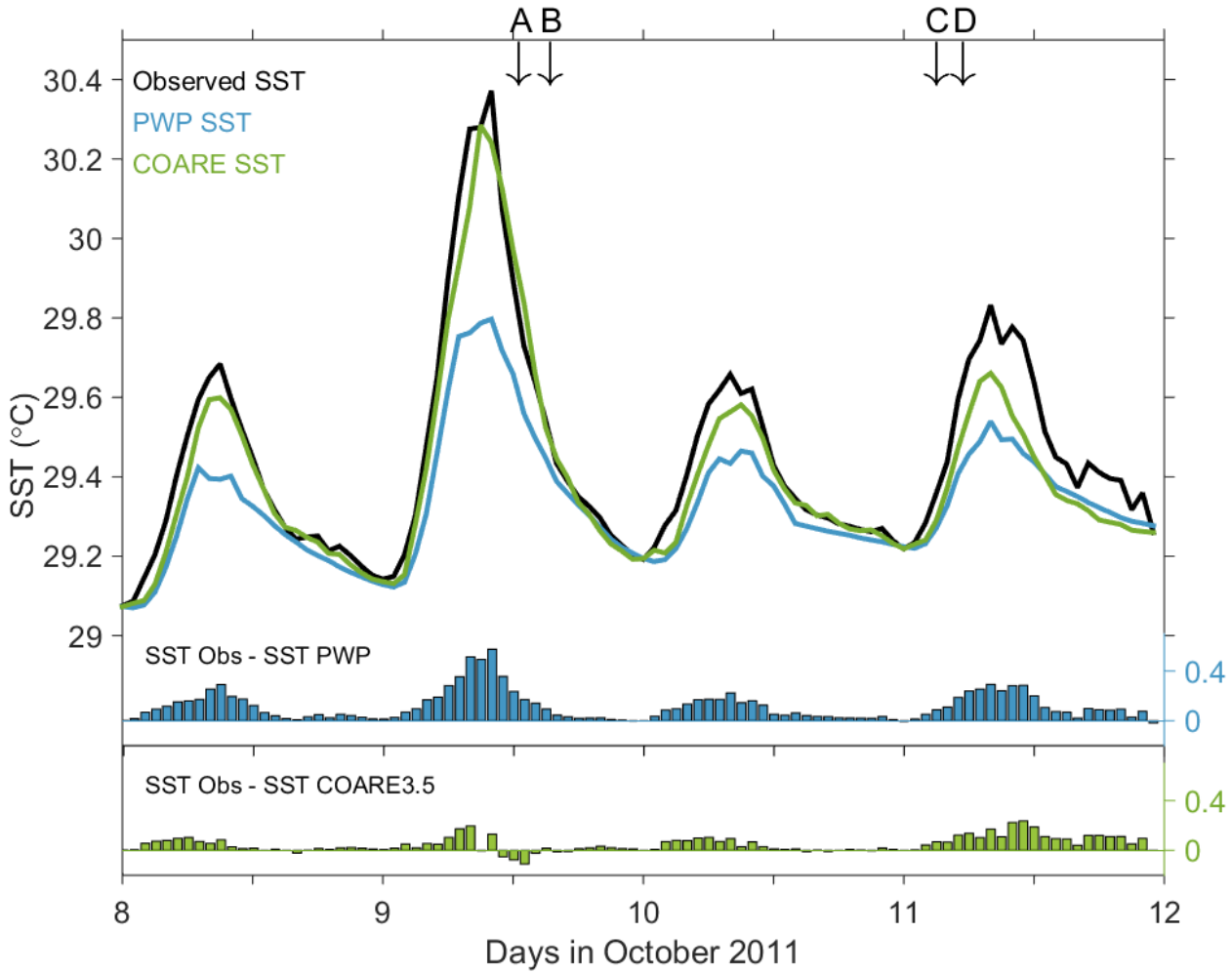

FIGURE 4.4: Temperature anomalies between PWP and COARE3.5 and the observed sea surface temperature. COARE3.5 was forced with a temperature time series measured at 1.6 m. Letters A-D and arrows mark times of temperature profiles illustrated on Figure 4.3.

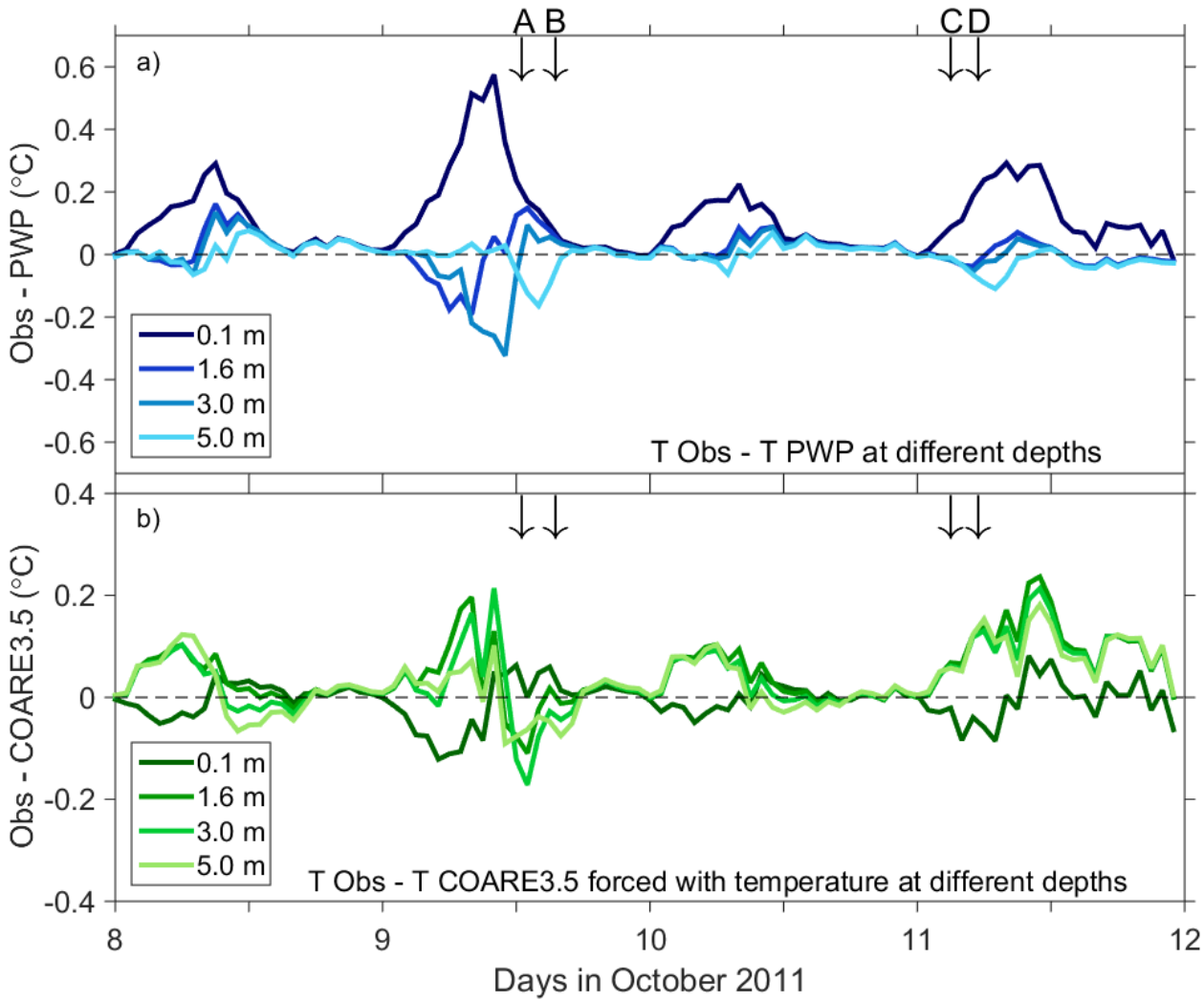

FIGURE 4.5: Temperature anomalies between models and observations (a) anomalies between observation and PWP model output at different depths, (b) anomalies between observed SST and COARE3.5 SST when COARE3.5 is forced with a temperature time series at various depths. Letters A-D and arrows mark times of temperature profiles illustrated on Figure 4.3.

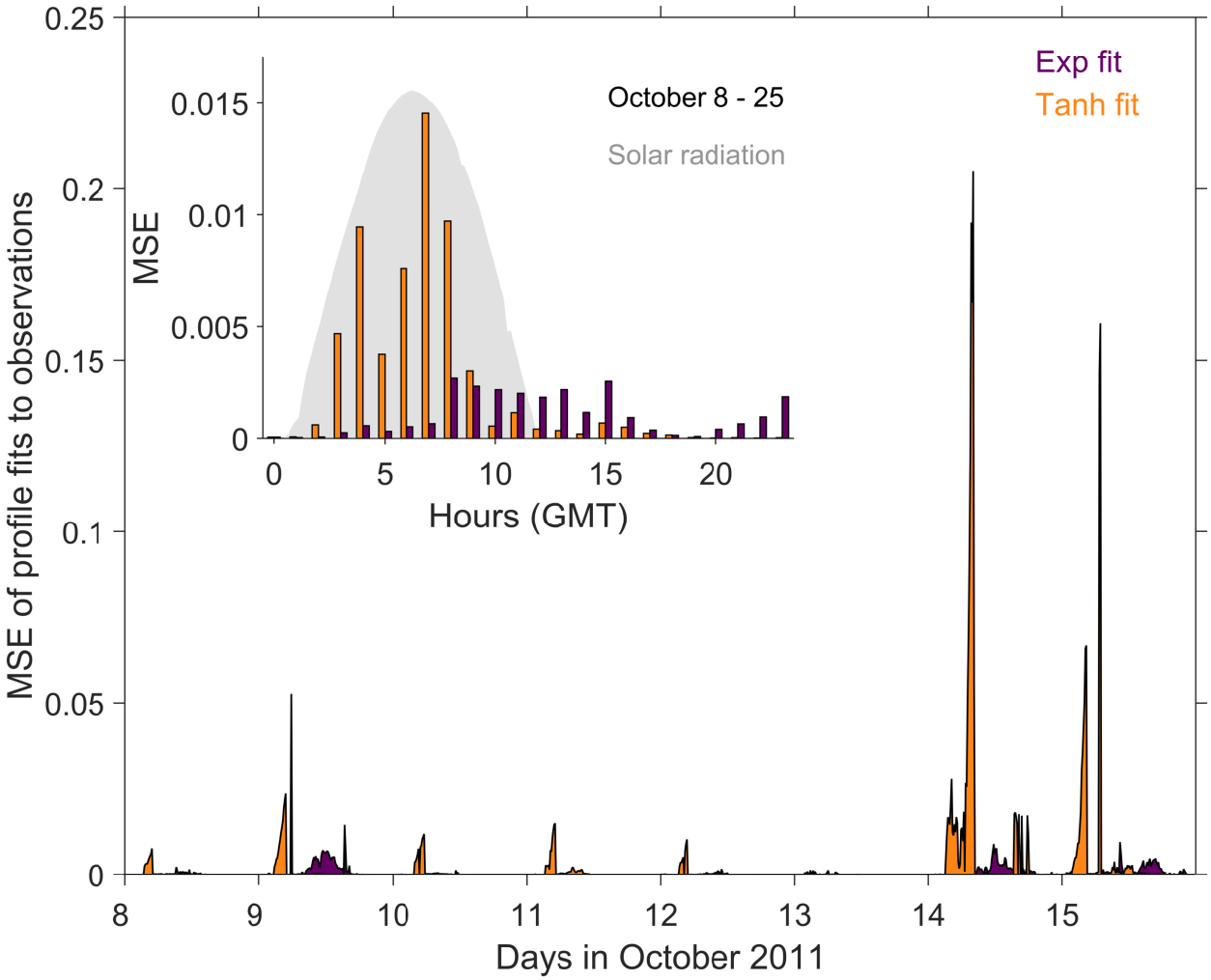

FIGURE 4.6: Mean square error (MSE) of hyperbolic tangent and exponential fits to temperature profiles highlights the time evolving shape of observed profile. The inset shows a composite of hourly MSEs over 17 days. Insolation is shaded in grey to illustrate daytime.

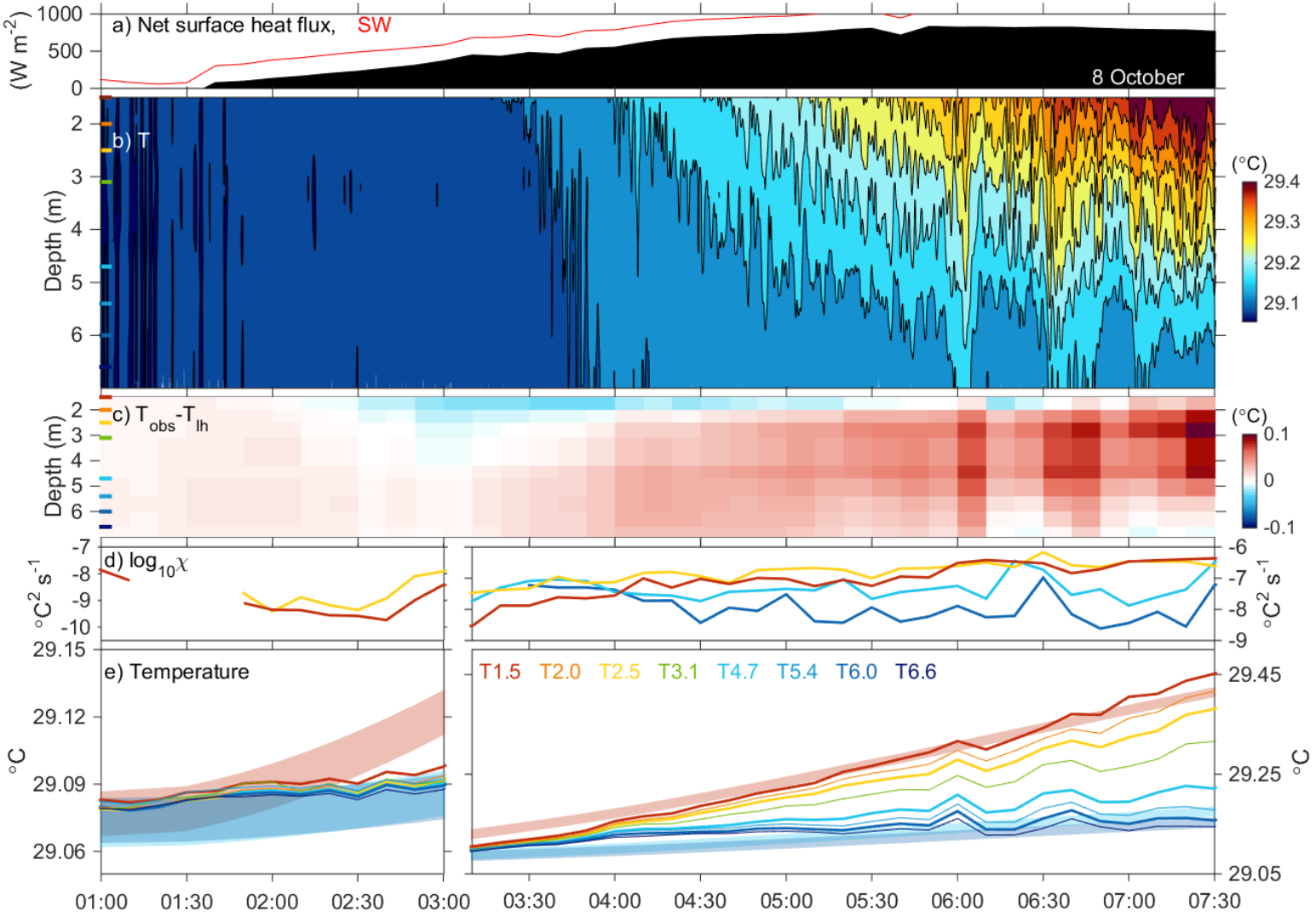

FIGURE 4.7: Upper ocean structure during DWL formation on 8 October 2011. (a) Net surface heat flux, (b) 30-sec low-passed temperature with 0.04°C contours, (c) Temperature difference between observation and temperature derived from absorbed solar radiation, (d) temperature variance dissipation, and (e) Observed temperature (thin, solid lines) and temperature derived from absorbed solar radiation (shaded, thick lines). The left panels on (d-e) have a different ordinate range than the corresponding panels on their right. Colored ticks on the left of (b,c) indicate the depth of each sensors colored on (d,e).

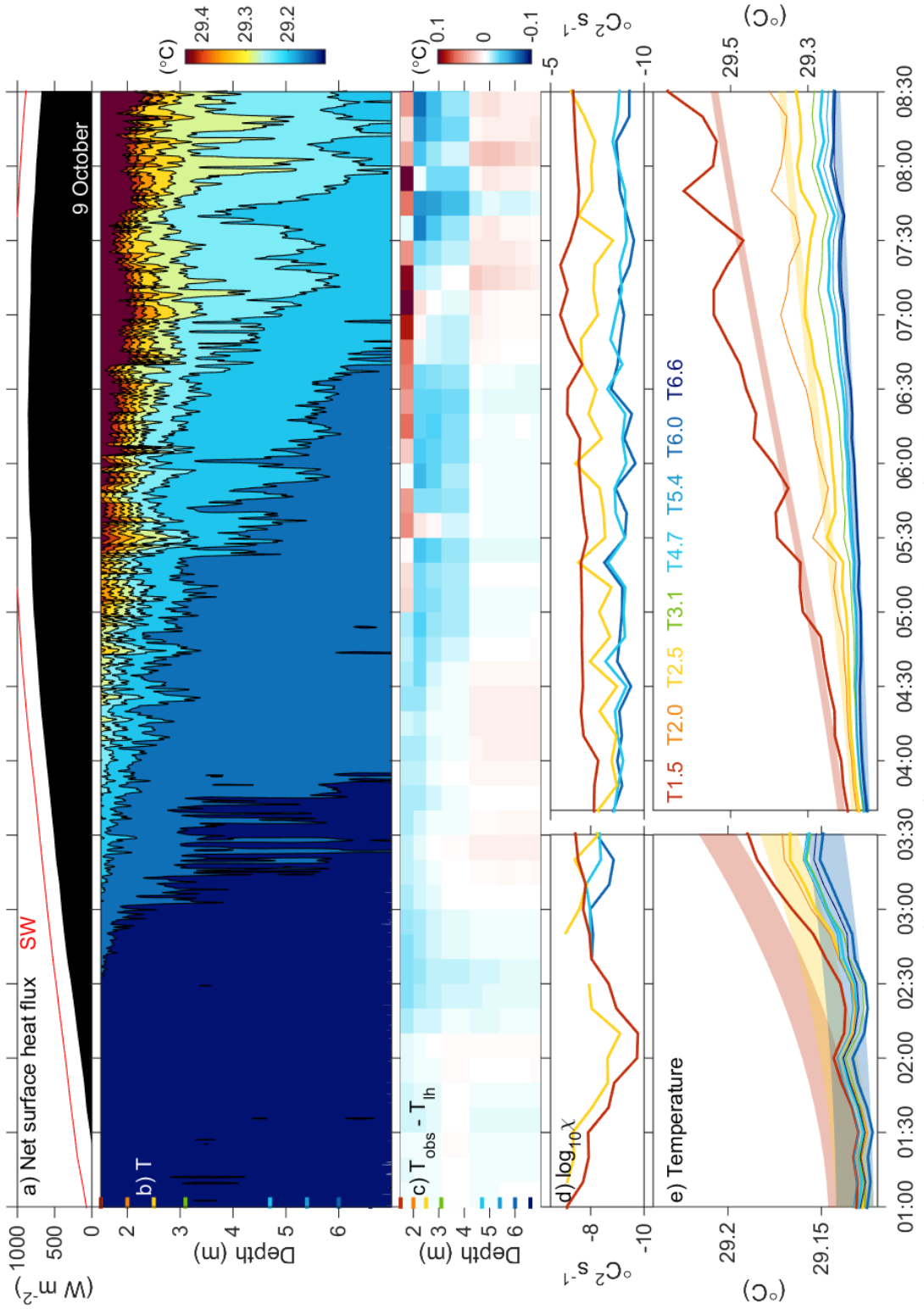

FIGURE 4.8: Same as Figure 4.7 but on 9 October 2011

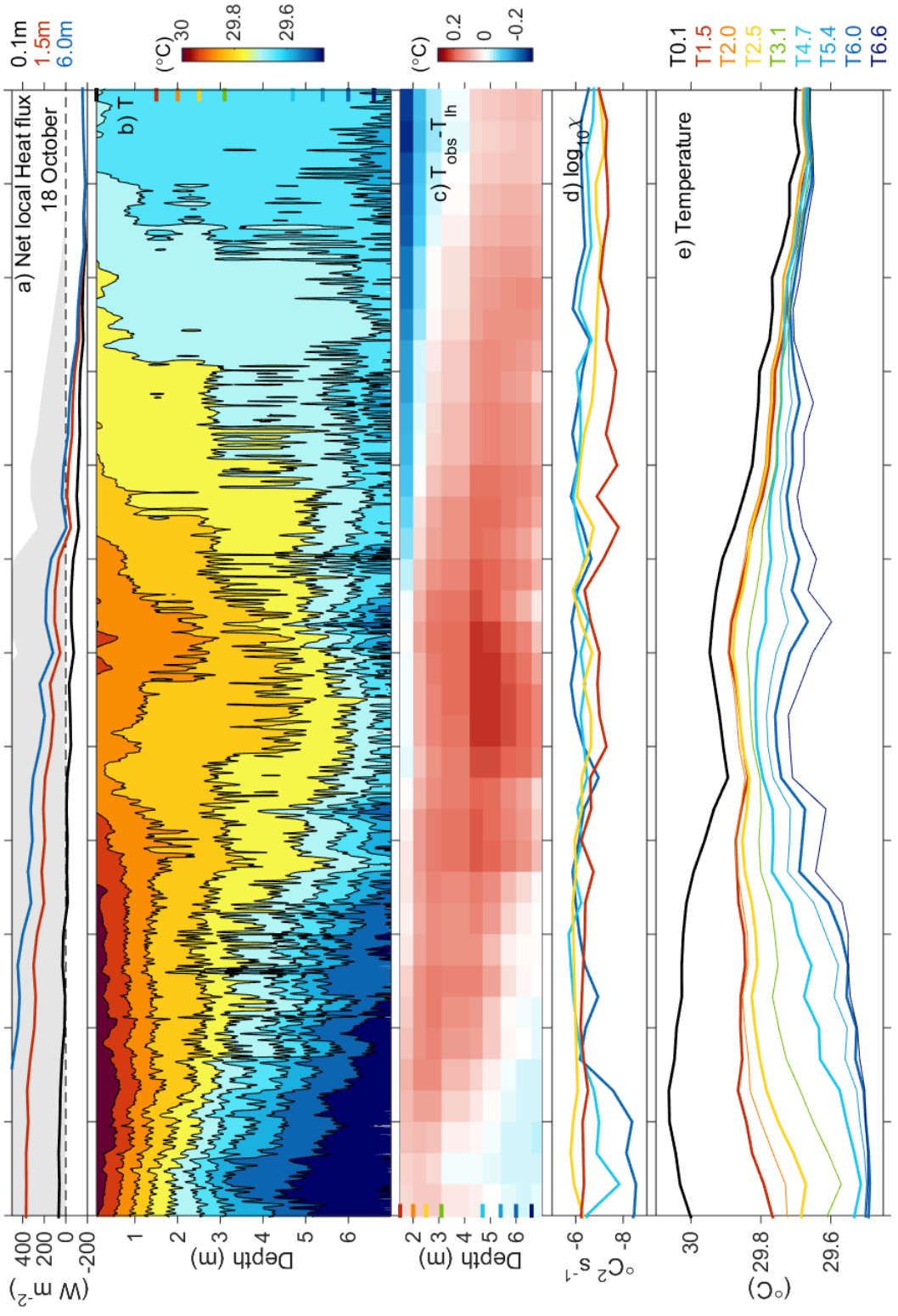

FIGURE 4.9: Upper ocean structure during DWL collapse on 18 October 2011. (a) Net local heat flux calculated from the divergence of net surface heat flux and absorbed solar radiation at the sea snake (black), T1.6 (red) and T6.0 (blue), and shortwave radiation in light grey shades, (b) 30-sec low-passed temperature with 0.06°C contours, (c) Temperature difference between observation and temperature derived from absorbed solar radiation, (d) χ, and (e) Observed temperature. Colored ticks on the left of (b,c) indicate the depth of each sensors colored on (d,e).

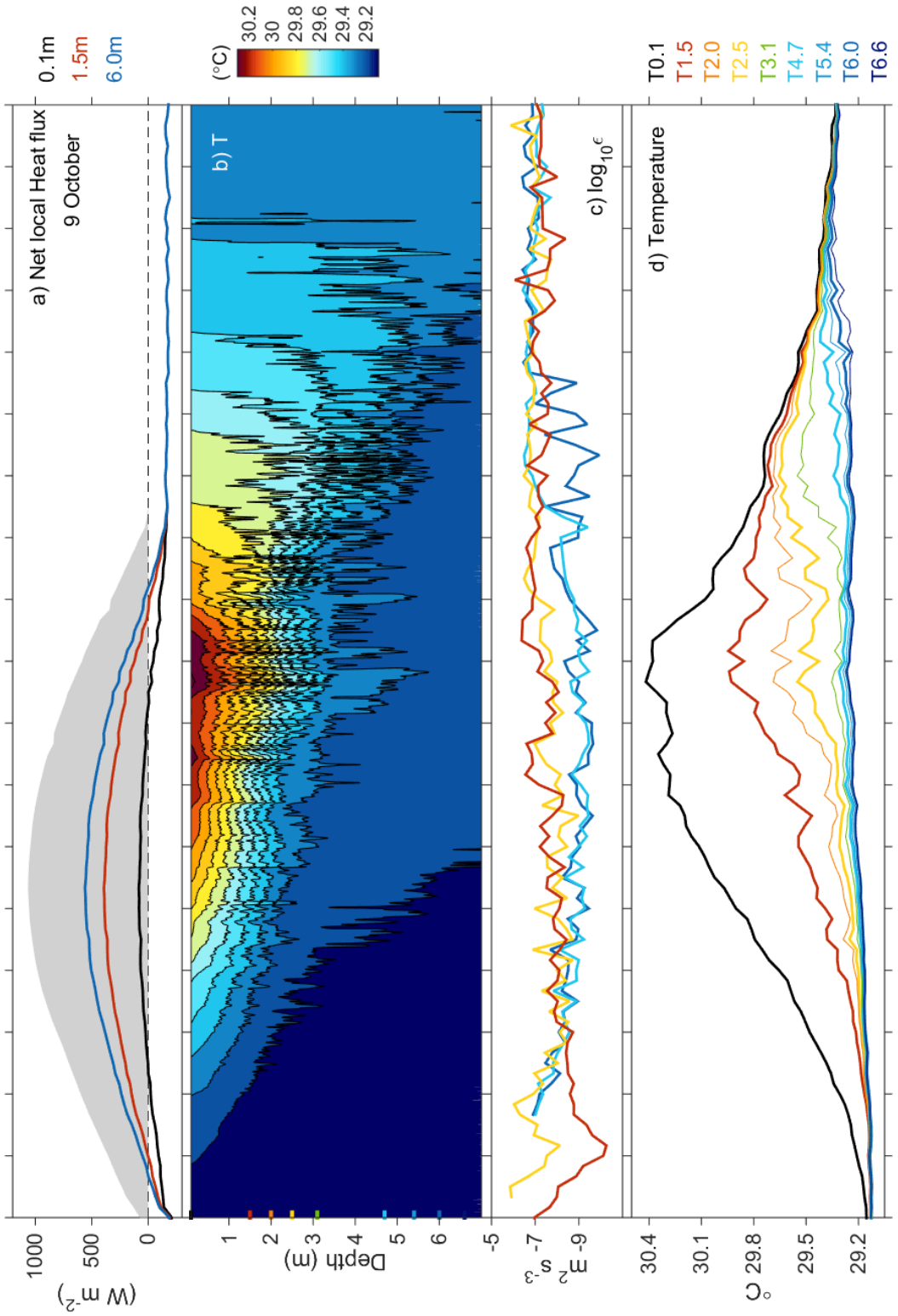

FIGURE 4.10: Same as Figure 4.9 but on 9 October 2011 and with 0.1°C temperature contours on (b)

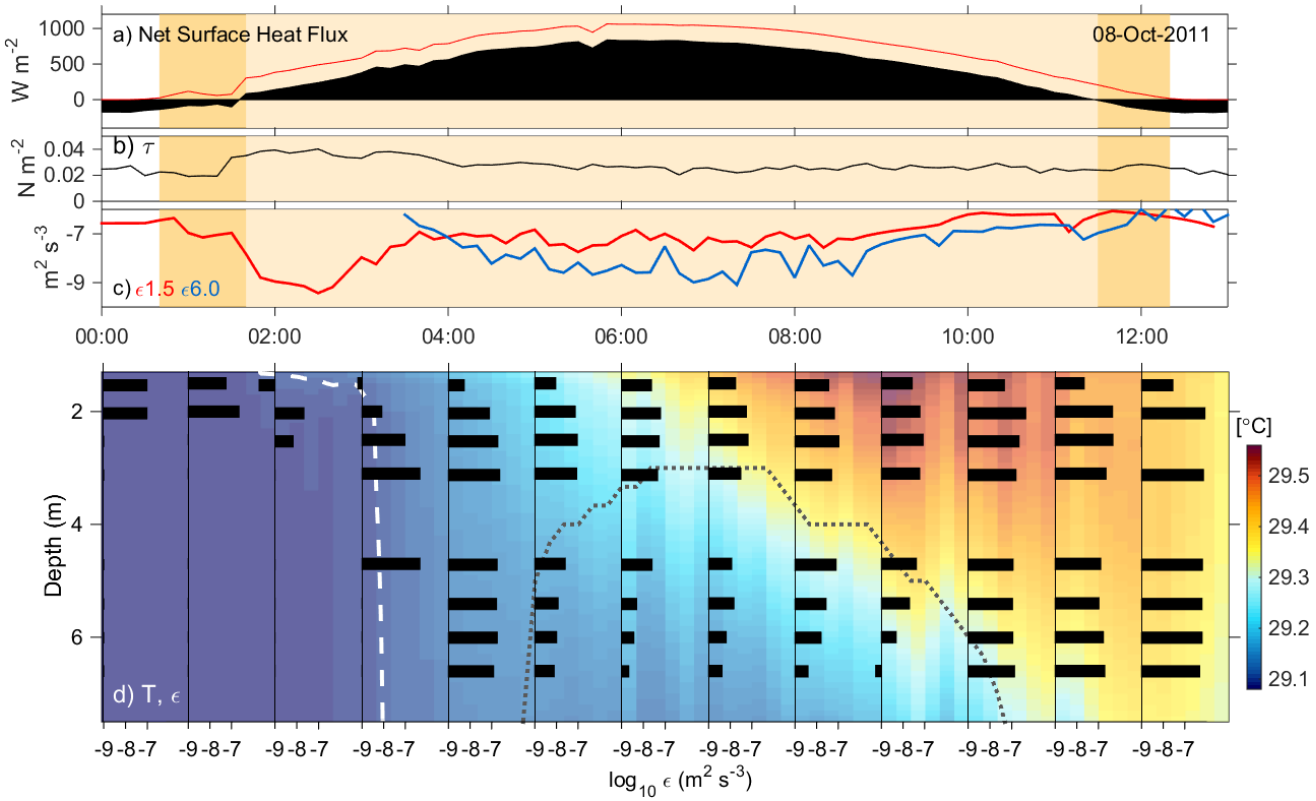

FIGURE 4.11: Evolution of temperature and turbulence during daytime on 8 October 2011. (a) Net surface heat flux (black) and short wave radiation (red), (b) wind stress, (c) TKE dissipation, (d) Temperature (color shading), mixed layer depth (grey dots), and base of the diurnal warm layer following the isotherm of T0.1 one hour after sunrise (white dashes) overlaid with hourly profiles average of ϵ (black bars). The baseline for ϵ bars is at 10^{-9} m^2s^{-3}. Turbulence when the local temperature gradient was smaller than $-10^{-3.1}$°C m^{-1} were removed. Positive net surface heat flux is shaded in yellow while nonzero solar radiation is shaded in orange on panels (a-c).

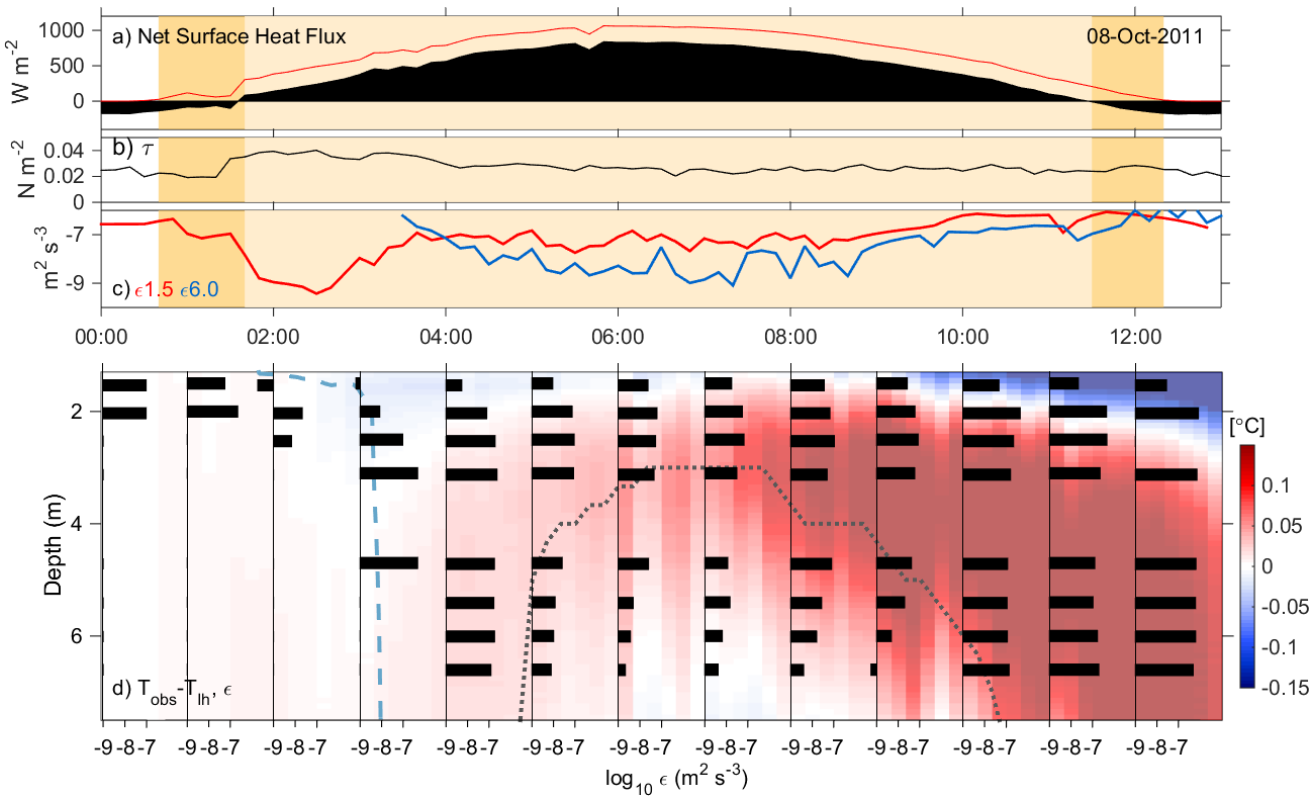

FIGURE 4.12: Same as Figure 4.11 but for the divergence of temperature between observed and radiative temperature on (d)

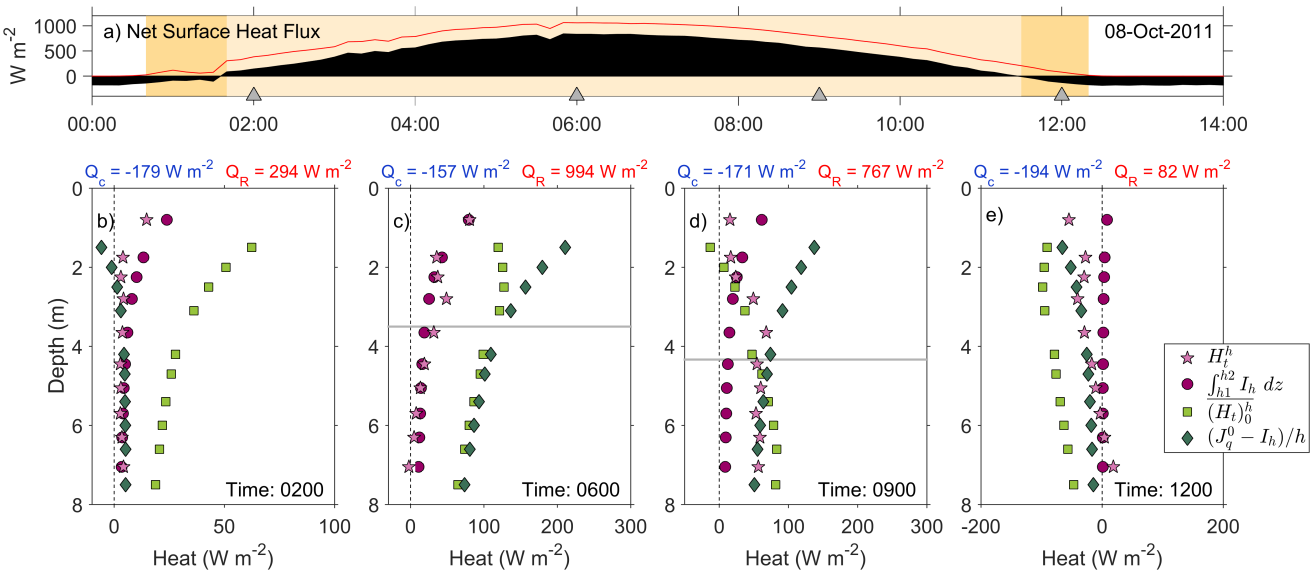

FIGURE 4.13: Heat budget profiles computed locally (purples) or averaged from the surface (greens) on 08 October 2011. (a) Net surface heat flux in black and solar radiation in red. The grey triangles mark the time of heat profile panels below, yellow shading marks net surface heating, and orange shading marks positive shortwave radiation during net surface cooling; (b)-(e) local divergence of absorbed solar radiation over 1 meter (W m^{-2}, purple circles) and local change in heat content (W m^{-2}, pink stars), divergence of heat between the net surface heat flux and the absorbed solar radiation (W m^{-3}, green diamond), and change in heat content integrated form the surface to each instrument (W m^{-3}, green squares). Net surface cooling Q_c and downwelling solar radiation entering the ocean at the surface (minus albedo)Q_R are indicated in blue and red, respectively.

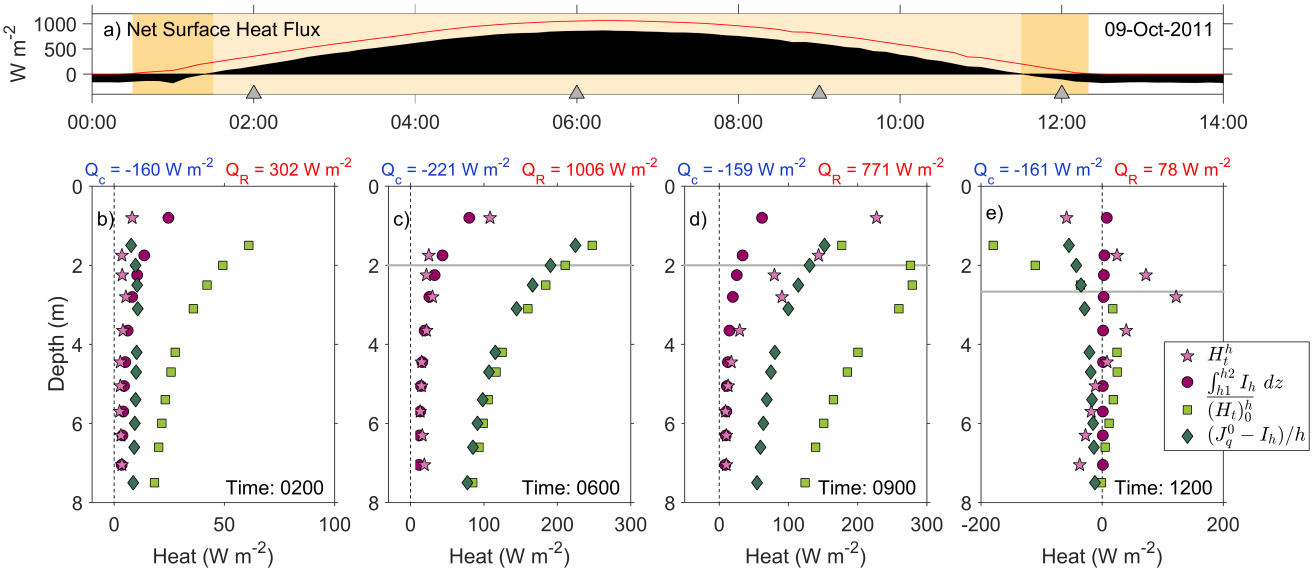

FIGURE 4.14: Same as Figure 4.13 but 09 October 2011.

Thermohaline and kinematic properties of freshwater lenses

Aurélie J. Moulin, James N. Moum, and Emily L. Shroyer

5. THERMOHALINE AND KINEMATIC PROPERTIES OF FRESHWATER LENSES

5.1. Abstract

Twenty-six freshwater lenses (FWLs) were observed in the equatorial Indian Ocean during the DYNAMO experiment and examined using temperature, salinity, C- and X-band radar, and temperature microstructure from a bow-mounted thermistor chain. Measured cross-sections ranged from 5 to 60 km long and 3 to 20 m deep. Salinity anomalies were up to -0.4 psu while the temperature anomalies were between -0.8 - +1.2 ℃. Lenses were generally cooler than surrounding ocean water but a few displayed pockets of warm anomalies. These positive anomalies persisted overnight in spite of evaporative cooling because of the strong stratification at the lenses' base. The freshwater content and temperature of lenses reflected the precipitation history over the path of lenses in the previous 48 hours. Several lenses presented a distinct front with a convergent, turbulent head as typically found with buoyant gravity currents. These fronts were measured propagating at the internal wave speed between 0.04 - 0.14 m s^{-1}. FWLs subject to relatively higher wind speed exhibited the weakest thermohaline signatures and high turbulence. Lenses subject to weak winds however also displayed high turbulence but with stronger thermohaline signatures. Lenses were estimated to be 3 to >48 hrs old and were forecasted to last an average of 3 days if mixing was the only dissipation mechanism.

5.2. Introduction

Fresh water lenses (FWLs) deposited by convective storms in equatorial regions of the ocean have been observed for the past 20 years. Their transient nature however makes

it difficult not only to describe their behavior but also to assess their spatial and temporal extent and effect on air-sea interaction.

The central Indian Ocean is thought to be an area where Madden-Julian Oscillations (MJO) intensify before continuing eastward over the maritime continent and western Pacific Ocean, where they produce strong precipitating storms (Zhang, 2005). The recipe for MJO initiation remains unclear, especially the role of sea surface temperature in air-sea interactions.

FWLs have been referred to as buoyant gravity currents (Soloviev et al., 2002) but a thorough analysis of their structure and dynamics has yet to be performed. In the ocean, gravity currents propagate and redistribute their heat and salt content within the ambient water (Hacker et al., 1996) and therefore their structure and dynamics are important to understand. Positively buoyant gravity currents occur when a light fluid flows into an ambient fluid of greater density. The analogous dense gravity currents have been extensively studied both numerically and experimentally in the laboratory, in the ocean with turbidity currents, and in the atmosphere with sea breeze fronts or pyroclastic flows for example (Simpson, 1997). In contrast the body of research about light gravity current is scarce.

5.2.1 Structure and evolution of gravity current

Buoyant gravity current theory may provide constraints on freshwater lens longevity and how they redistribute heat and salt. Gravity currents are driven by horizontal pressure gradients resulting from the density difference between the current and its ambient fluid. They are typically composed of a bulging head at the front and a tail in the following flow (Simpson, 1982). The head of a gravity current forms first from the roll up of the shear layer at the current interface (Cantero et al., 2007) and after some time only the turbulent front with a calm body is observed (Cantero et al., 2007). The thickness of a positively buoyant gravity current is proportional to its radius (Ungarish, 2009), itself

proportional to the duration of its spread.

Mixing into turbulent head

Shear instabilities incorporate ambient fluid into the head, decreasing the density anomaly with the ambient fluid and decreasing the driving force of the current (Cantero et al., 2006). This entrainment is independent of the magnitude of the density gradient across the front (Hallworth et al., 1993). Gravitational instabilities are also created by a thin layer of ambient fluid interleaved between the current and the boundary. These latter instabilities have been described as shifting lobes and clefts which drive more mixing into the head (Hacker et al., 1996).

Evolution

Undiluted flow is constantly brought forward into the head by counter-rotating vortices until the initial volume of buoyant fluid is eroded. Over this time period, the current propagates at a constant speed. The flow divergence caused by the curved geometry of a cylindrical current however quickly engulfs ambient fluid, decreasing the maximum density, and generating a constant slow down and thinning of the propagating front (Ungarish and Zemach, 2005). The gravity current then evolves into a balance between inertial and buoyancy forces (Simpson, 1982; Hallworth et al., 1993). Vertical velocities in the head are not insignificant, reaching 40 - 60% of the horizontal velocity (Patterson et al., 2006).

The propagation speed and thickness of the gravity currents are a function of the stratification and density anomaly with the ambient fluid (Ungarish, 2009). Gravity currents are known to interact with ambient stratification, causing a fragmentation of the lens and in some instances the separation of the head from the rest of the flow, which subsequently forms a new head (Soloviev et al., 2015). The lens' center was also observed

to collapse due to vertical mixing in models without stratification and with weak wind forcing (Soloviev et al., 2015). Models of a propagating lens displayed a sharper leading density front from frontal convergence, while upwelling from divergence under the gravity current tail weakened density structure at the trailing edge (Wijesekera et al., 2003).

Effect of wind and current

The effects of ambient flow and winds on a buoyant gravity current have also received limited attention. Hogg et al. (2005) report that a propagating two-dimensional flow will initially spread both upstream and downstream: downstream the head remains and the flow deepens while the upstream flow takes the shape of an arrested wedge, eventually becoming eroded. Lenses are typically smaller than the equatorial Rossby radius of deformation therefore determining their propagation direction independently of Earth's rotation. Simpson (1982) notes that a head wind will lengthen the gravity current head while a tail wind will have the opposite effect. Two studies by Soloviev et al. (2002); Soloviev and Lukas (1997) compared the effects of the wind and current directions to Stommel's "overturning gate" concept (Stommel, 1993): a gravity current propagating upstream (downstream) with a head (tail) wind would become a turbulent bore (arrested wedge) and quickly (slowly) erode away. More recently, Soloviev et al. (2015) modeled the evolution of a freshwater lens using three-dimensional Large Eddy Simulation (LES) in a rectangular domain over 40 minutes. They observed a distinct asymmetry of a lens subject to wind stress with the formation of a bore-like front upwind and a thinning tail downwind. Soloviev et al. (2015) suggest that the interface of a propagating bore might become compensated in density or disappear entirely. The speed of a gravity current is driven by the pressure gradient but is also modulated by wind velocity (Wijesekera et al., 2003).

5.2.2 Literature about FWL

Studies on freshwater lenses, or more broadly on the effect of rainfall on surface salinity, have been performed using modeling (Wijesekera et al., 2003; Soloviev et al., 2015), observations from drifters (Reverdin et al., 2012), towed platforms (Asher et al., 2014), TAO moorings (Henocq et al., 2010), or Argo floats supplemented with larger scale atmospheric data using NCEP reanalysis products or TRMM (Anderson and Riser, 2014). FWLs are frequently observed in tropical latitudes and can persist for several days (Henocq et al., 2010) to less than a day in conditions of westerly wind bursts (Wijesekera et al., 1999). Surface mixing is confined to the surface by a shallow halocline and its shape and size depended on the shape and size of the rain squall responsible for the salinity anomaly (Wijesekera et al., 1999).

FWLs retain heat

Lenses deposited by convective storms can perturb air-sea interactions by capping the ocean and confining heat and momentum (Wijesekera et al., 2003), therefore inhibiting their exchanges (Wijesekera and Gregg, 1996). Under these conditions, heat and salt remain trapped in the ocean's interior and become available again once the freshwater lens has dissipated. This would provide a mechanism to pump more energy into the atmosphere by keeping the sea surface temperature warm. Lukas and Lindstrom (1991) found that heat flux at the base of the surface mixed layer was small, with no entrainment of cool thermocline waters because the salt stratification inhibited mixing. This enhances surface mixed layer heating in the absence of westerly wind bursts. When stormy conditions arrive, the surface mixed layer is deepened and the barrier layer eroded.

Link to barrier layer

The surface mixed layer can be shallow in equatorial areas subject to strong heat flux, heavy rain, and intermittent winds (Lukas and Lindstrom, 1991). Wijesekera and Gregg (1996) demonstrated that heavy and sudden precipitation could form buoyant layers with haloclines such that an effective barrier to wind forcing and buoyancy flux was created. These fresh, cool lenses acted in essence as a barrier layer, a phenomenon first described by Lukas and Lindstrom (1991). The warm water underneath FWL becomes isolated from the interior by reduced entrainment cooling from the thermocline and by providing a slippery surface layer which effectively contains heat, salt, and momentum (Soloviev and Lukas, 2006). Barrier layers are known to form either by subduction of a salty water mass below a fresher mass, or by rainfall in conditions of weak mixing and surface heat flux. In this latter case, barrier layers are thinner and tend to dissipate in a few days by nighttime entrainment or strong wind events (Cronin and McPhaden, 2002).

Past observations

Reverdin et al. (2012) show a time lag between the greatest S and T anomalies. The authors attributed this lag to surface heat loss confined in lenses at night, wind stirring of temperature stratified layer during daytime, or rain-water induced cooling. They further noted that the temperature anomalies were smaller during daytime as lenses were subject to insolation. The timing of precipitation compared to the daily cycle of turbulence has an effect on the intensity of the salinity anomaly resulting from the precipitating storm. The nighttime negative buoyancy flux strengthens mixing which favors the quick dissipation of precipitation (Cronin and McPhaden, 1999). Daytime precipitation however tended to be deposited atop a stably stratified water column with low mixing and led to the production of a shallow, stable fresh layer (Cronin and McPhaden, 1999).

Reverdin et al. (2012) made direct observation of the evolution of salinity within a FWL from a towed platform and reported a net increase in the salinity anomaly recovery for wind speeds around 5.5 m s^{-1}. In these wind conditions the recovery time was greater than 6 hrs while it was less than 2 hrs for wind speeds > 7.6 m s^{-1}. Puddles have been observed propagating at 0.08 m s^{-1} (Soloviev and Lukas, 1997) and at 0.05 m s^{-1} (Wijesekera et al., 1999). When winds were greater than 10 m s^{-1}, the gravitational spreading of a lens was thought to be a negligible dissipation process compared to wind mixing.

Mixing in FWL

Smyth et al. (1997) reported an attenuation of turbulent kinetic energy dissipation underneath FWLs resulting from the isolation of the ocean's interior from the surface and the suppression of turbulent kinetic energy (TKE) source descending from the surface. This subsurface mixing attenuation was instigated as freshly deposited rain created a stable layer at the surface, which was already observed in Price (1979). This buoyant surface fresh layer was determined to control near-surface mixing (Smyth et al., 1997). Therefore, the near-surface mixing regime can also be affected by FWLs. Over time, this barrier was broken down by turbulent mixing, and vertical heat fluxes were reestablished (Smyth et al., 1997).

Rain lenses can therefore alter the vertical heat fluxes from which small and large scale atmospheric systems gain energy.

It then becomes pertinent to ask whether freshwater lenses can inhibit air-sea interactions on spatial and temporal scales relevant to MJOs (O(100 km, 2 weeks)), and the magnitude of the heat flux changes. One of the objectives of the Dynamics of the Madden-Julian Oscillation experiment (DYNAMO) was to provide a complete dataset

from 1 km down in the ocean up to 25 km in the atmosphere (Moum et al., 2014) to evaluate the impact of FWL on the structure and dynamics of the oceanic upper layer. Here, a set of 26 FWL was identified and analyzed. A brief summary of data and methods is provided (section 5.3.) followed by a description of FWLs length and thermohaline characteristics (section 5.4.), kinematic properties (section 5.5.), structure of non-propagating lenses (section 5.6.), and a freshwater and heat budget based on accumulated rainfall and salinity anomalies (section 5.7.). A summary is provided in section 5.8..

5.3. Methods

Subsurface and meteorological data from DYNAMO Leg2 (8-26 October 2011) and Leg3 (12-24 November 2011) were used in this work (Section 2.2).

A freshwater lens was characterized by a fresh salinity anomaly which also coincided with a positive or negative temperature anomaly, was coherent over several meters depth, and had a minimum of one hour time interval between two consecutive fresh patches.

In addition to T-chain subsurface measurements, data from the Chameleon profiler were used when FWLs were deeper than the depth range of the T-chain. Propagating velocities of FWL fronts were estimated using X-band radar 15-sec average and variance of sea surface roughness (Appendix A).

The age of lenses was estimated from C-band precipitation maps as the length of time needed for a cumulative sum backward in time and space of radar precipitation at the lens position to equal the freshwater content of a lens (see Appendix B). Freshwater content was calculated as the thickness of fresh water needed to dilute ocean water to the depth of the isohaline representing 90% of the salinity anomaly.

5.4. Thermohaline and length characteristics of freshwater lenses

5.4.1 Contextual background

The central equatorial Indian Ocean typically sees intense insolation during the fall with intermittent, intense rainfall from convective storms when no MJOs are present. Atmospheric conditions during DYNAMO ranged from diurnal heat flux up to 900 W m^{-2} with sporadic cloud cover to mostly overcast (Figure 5.1). The nightly heat flux averaged -200 W m^{-2}. The wind regime was variable with calm days at 0.01 N m^{-2} and windier periods up to 0.20 N m^{-2}. The observations spanned two MJOs, on 23-27 October 2011 and 24-30 November 2011 (Moum et al., 2014). Local precipitation was intense and sporadic with rain rates up to 70 mm hr^{-1}. Temperature records emphasized a diurnal warm layer of up to 2℃ when insolation was strong, and nightly heat dissipation from convection resulted in the vertical homogenization of temperature. The average temperature difference between 0.1-1.5 m was stronger in November 2011 at 0.18 ± 0.42 ℃ and a mean stratification at 15 m of $9.1e^{-5}$ ± $18.5e^{-5}$ s^{-2}. Eight (out of 13) days on Leg3 had a peak surface temperature difference >1℃. Comparatively, Leg2 featured a weaker stratification at $2.4e^{-5}$ ± $4.5e^{-5}$ s^{-2}, mean temperature difference between T0.1 and T1.5 of 0.09 ± 0.20℃, and only five (out of 20) days with peak surface temperature difference >1℃.

Although salinity above 5 m was mostly homogeneous, both legs displayed periods when the surface salinity was significantly fresher than the average salinity over the top 30 m (Figure 5.1d). We observed different tendencies, however, with two fresher periods lasting several days occurred at all depths <30 m (16-20, and 23-24 October). In November, the background salinity had increased by 0.25 psu due to the intrusion of warm and salty water from the Red Sea around 30 m depth between the two sampling periods (Schott and McCreary, 2001). Surface salinity dropped to about 35.1 psu on 14 November 2011 and did not recover to its 30 m depth-average by the end of the record

period; this freshening was also coincident with a period of elevated stratification at 15 m. All lenses are clearly discernible from the surface salinity as clean spikes and their duration is highlighted by the width of the shaded bands on Figure 5.. Also noteworthy is the timing of fresh water lenses observation at the ship and local precipitation (Figure 5.1b). Some puddles were observed in the absence of local precipitation for several days, suggesting that these lenses can be formed upstream and drift for some time. The occurrence or intensity of FWL and the onset of MJOs do not appear to be correlated.

5.4.2 Lens characteristics

The length of observed cross sections ranged from 3-65 km with a distribution heavily skewed toward shorter dimensions (Figure 5.2), and a depth range of 4-20 m. Lenses were estimated at 1 to 38 hrs old and 11 contained more freshwater than the accumulated precipitation in the previous 48hrs. Most lenses required just 40 mm or less. Haline anomalies at the surface could be as high as 1.2 psu fresher (S_0) but most were under 0.4 psu, while temperature anomalies could be either warm or cool. Although mostly cool and smaller than -0.5℃ at T4.2 (but up to -0.8℃ at T0.1), four lenses were distinctively warmer than ambient water by up to 0.5℃.

5.5. Kinematic properties of lenses with buoyant gravity current characteristics

5.5.1 Thermohaline properties

Lens C (Figure 5.3) was observed over 8 hrs shortly after a wind burst associated with moderate precipitation. The temperature structure responded quickly to the wind event and became homogeneous. Salinity behaved similarly to temperature but shallower

sensors displayed a slight dip in response to rain. This lens was strongly stratified in both temperature and salinity and progressively became fresher and cooler at the surface. χ was elevated during the wind event and during nighttime convection(Figure 5.3i).

Temperature variance dissipation was high within lenses owing to the strong temperature gradients. The sharp fronts seen on lenses C and E showed strong turbulence and presented characteristics of gravity currents with a turbulent head. Finally, as previously reported by Smyth et al. (1997), mixing underneath patches is weak. This is best seen beneath lenses C and E (Figures 5.3 and 5.4).

Lens E (Figure 5.4) was relatively short lasting 3 hrs but spanned sunrise. The lens remained cool at the surface but was seen warming immediately following the change in sign of the surface heat flux. Salinity was more complex with pockets of freshwater in an otherwise weakly salt stratified lens. The particularity of lens E was the presence of a sharp front both upstream and downstream, unlike C which featured only a front upstream. More than their sharpness, convergence was suggested at each of these fronts with entrainment of surface cold (warm) water at 0000 (0330) before (after) sunrise, seen as a cold (warm) spike in deeper sensors. T0.1 measured cool waters from the leading to the trailing edge. Deeper sensors however measured much warmer waters towards the lens' center. It is unclear whether this constitutes a lens collapse as modeled by Soloviev et al. (2015) as we observe large temperature oscillations down to 6.0 m in between each front.

5.5.2 Kinematic properties

Case study

An abrupt drop in salinity (S) and temperature (T) was measured on 23 November 2011 at 0400 UTC (Lend F, Figure 5.5c,d). This drop was also associated with an equally

sharp and thin turbulent front in temperature dissipation (Figure 5.5f) in the absence of atmospheric forcing. The dissipation of temperature variance however was also high within the area for $\backsim$20 minutes, reminiscent of the classical gravity current turbulent head. The body of lens F remained turbulent with more elevated turbulence than depicted in Figures 5.3-5.4. The turbulent head delineated on the salinity structure measured 720 m across (Figure 5.5f) and reached 14 m depth. On a finer time resolution however, another smaller, sharper turbulent head was distinct from the broader, deeper feature. This smaller head was 24 m across and 6 m deep (Figure 5.5g). It is unclear whether these smaller features were lobes and clefts caused by gravitational instabilities from ambient fluid atop the lens, or a smaller scale turbulent head. The salinity image (Figure 5.5f) emphasized the difference in salt structure beneath the lens. Ahead of the front and beneath the turbulent head, salt was homogeneous. Underneath the body of the lens, the salt gradient progressively weakened in space due to the shear instabilities generated in the wake of the propagating gravity current.

Ahead of the main front, a smaller drop in T and S, and a spike in mixing were seen around 0255. The shape of the anomaly was similar to the main body of lens F, although weaker in all fields. It also resembled a gravity current with a turbulent head immediately followed by warmer, saltier water. This observation is similar to the features propagating ahead of the main gravity currents modeled by Soloviev et al. (2015). This secondary gravity current showed 6-minute internal waves (power spectrum not shown) which are known to occur by resonance with underlying stratification (Soloviev and Lukas, 1997) when a certain Froude number criteria and depth ratio of the lens to the ocean are satisfied. Both these criteria were met for lens F, supporting the possibility of a wave propagating ahead of the body of the main gravity current.

As this patch was measured after several hours of morning insolation, a distinct ribbon of warm water outlined the turbulent head. A narrow area of relatively smooth

ocean surface with low reflectivity was seen behind a strip of rough surface features on a succession of X-band images. This difference in roughness with a sharp and geometrically straight meridional interface represented the convergent frontal zone as the freshwater lens propagated at the surface. The time at which this band arrived at the ship coincided with the arrival time of the front in subsurface T and S sensors (Figure5.6). The vertical velocity was calculated from conservation of mass and at 0.06 m s^{-1} is within the range of 40-60% of the horizontal velocity (C_f=0.09 m s^{-1}) cited by Patterson et al. (2006).

General propagation

Ten fronts were recorded on X-Band radar with the same physical characteristics. The successful tracking of fronts on successive radar images then informed on the speed C_f at which they were propagating relative to the ocean current, ranging from 0.03 to 0.16 m s^{-1} and mostly in the southeastern quadrant. Measured propagation speed was very close to that expected from linear wave theory, $\sqrt{g'h}$, where g' is the reduced gravity $g\Delta\rho/\rho$. The comparison of all intrinsic and measured front velocities showed good agreement (R=0.87, Figure 5.7) and supported the conclusion that freshwater lenses can propagate as buoyant gravity current. Not all observed lenses featured a turbulent head or a sharp front, nor were they all captured on X-band radar. Wind speed might have been a limiting factor in the ability of the radar to detect fronts. There was no relationship between the strength of the density gradient across the front and capture on radar.

The front seen on Figures 5.5 and 5.6 propagates about 70° clockwise from the wind. Out of the ten fronts captured on X-band radar (of which we knew with certainty their propagation direction) three were oriented between 92° - 102° from the wind direction. The findings from Soloviev et al. (2002), who expanded on Stommel's overturning gate theory (Stommel, 1993) as well as Simpson's arrested wedge and turbulent bore theory established two categories to which a front could be ascribed. The case where a front

was propagating against the wind (>90°) was described in theory as turbulent and short lived. Our three fronts could fit in this category as they are thought to be younger than 3 hours. Soloviev et al. (2002) however also described fronts perpendicular to the wind as having increased turbulence at the front only but we saw increased turbulence throughout the entire lens. With wind blowing from the lens toward the ambient water (i.e., arrested wedge case), light water overlays denser ocean water as it is strained by the wind. In this case, the front becomes arrested, the sharp gradient remains, and shear instabilities eventually slowly erode the lens interface (Soloviev and Lukas, 1997; Soloviev et al., 2002). This also presumes however that the baroclinic pressure gradient, and therefore the density gradient is compensated across the front. In our findings, considering the wind blowing from the lens toward the ocean if the angle between the propagating front and the wind direction is within ± 80° seven lenses should not be seen propagating but arrested. Instead, they looked and behaved as turbulent bores.

We note that some sharp fronts were observed either at the leading edge of a lens, the trailing edge, both, or none. The data do not allow us to address this question and we can only hypothesize that the presence of a front indicated a relatively young to mature stage when enough fresh water was still available to drive the pressure gradient. The absence of a sharp front could be due to either its very young age when the gravity current was not yet established, or a very old lens which no longer propagated. A freshwater lens being a closed density contour, it therefore possesses half of its circumference downwind, and half upwind. This would imply, according to Simpson (1997) and Stommel (1993), that half of every rainwater lens is a density-compensated arrested front while the other half behaves like turbulent bores after the initial gravitational adjustment phase. This could be the case of the lenses we observed with a sharp front on one end and a wedge-like geometry on the other end (e.g. lens C, Figure 5.3). Alternatively, the lens propagation could have ended after running out of lighter fluid before the end of the observation as

observed in laboratory.

5.6. Thermohaline structure of non propagating lenses

Lens B (Figure 5.8) was observed for 25 hrs starting at 2100 on 17 October 2011. At the onset of observation the thermal structure was unstably stratified as is typically the case in freshwater lenses. The rest of the record showed a succession of warming and cooling trends. This is a marked difference from lens C which had a steady thermohaline stratification (Figure 5.3). Salinity progressively decreased with time nearer the surface until 0800, then featured a progressive return to ambient salinity around 1500 coincident with a wind event, and a weak fresh pool until 2100. At 4.2 m, the large salinity variability indicates the bottom of the lens, while the lack of variability at S7.5 means it remained below the lens at all times.

5.6.1 Relationship to environmental variables

Immediate response to rain

Lens A illustrated on Figure 5.9 shows the vertical progression of the response to a precipitating storm starting around 2100. The surface temperature and salinity responded immediately, followed by a 10-min delay at 1.5 m and about 20-min delay at 4.2 m. As the wind and precipitation ended around 2145, cooling and freshening stopped and the fresh patch was advected away. The dissipation of temperature variance, which was elevated due to nighttime convection, abruptly stopped as the FWL formed but the lens interior then became turbulent leaving the area below the patch disconnected from the surface. This was also observed by Smyth et al. (1997). During precipitation, the temperature and salinity response correlated well with wind speed and rain volume (Table 5.1). We also note that the observed density structure remained stable during and

immediately after precipitation. This differed from the findings of Anderson and Riser (2014) which used the Turner angle as a proxi for stability, or from Asher et al. (2014) who found unstable conditions if the rain rate was less than 6 mm hr^{-1}. Asher et al. (2014) found a clear relationship between rain rate and near-surface vertical salinity gradients during and immediately after precipitation. We find a similar relationship, although we are unable to resolve salinity as close to the air-sea boundary and analyzed the horizontal salinity gradient instead, with respect to wind speed and storm duration (Figure 5.10). High wind speeds were associated with weaker horizontal gradients, small speeds with moderate salinity anomalies, while moderate wind velocity was associated with highly variable responses. There was no clear distinction between the cluster of long storm (larger circles Figure 5.10) versus short ones, although longer storms were generally associated with fresher anomalies and higher rain rates. Inversely, short storms were associated with generally weaker rain rates and salinity anomalies.

Delayed observation

Once lenses were formed and advected past the ship, the absence of a sharp temperature front corresponded to the weakest temperature and salinity anomalies (Figure 5.11). There was a suggestive relationship between the magnitude of the thermohaline anomalies as there was a weak linear relationship in $\alpha\Delta$T, $\beta\Delta$S space (R=-0.59). In contrast to the findings of Soloviev and Lukas (1997); Soloviev et al. (2002), but in agreement with Reverdin et al. (2012), high wind speed in our findings corresponded to small T and S anomalies although the inverse was not necessarily true (Figure 5.11). Wind was however not the only source of turbulence, as a number of lenses had elevated mixing while the wind speed remained low. Also interesting to note is the proportion of stratiform and convective rain volume in each lens. Lenses which received proportionately more stratiform rain than convective rain by volume showed small thermohaline anomalies or a positive tem-

perature anomaly and were predominantly non-propagating. Of the propagating lenses, all but two were composed of more than 70% convective rain (not shown). The literature often mentions convective rain as the source of freshwater lenses (e.g. (Soloviev et al., 2015)). We find this to be the case for the majority of propagating lenses but stratiform rain should not be neglected as a contributing source.

Lens F on Figure 5.5 propagated downstream (observed before the gravity current's tail). The wind direction averaged 200° and 1.8 m s^{-1} for 3 hours prior to the front observation which was estimated propagating toward 92°. This implied that the wind was dragging lens water above ocean water, which, according to Soloviev et al. (2002), Soloviev and Lukas (1997), and Soloviev et al. (2015) leads to an arrested wedge and contradicts our observations. However, wind stress was very weak and may not have imposed a drag large enough to destabilize the frontal structure. Lens C (Figure 5.3) propagated upstream toward 300° with winds out of 10° at 3.0 m s^{-1}. In this case ambient ocean water was pushed atop the lens creating, unstable conditions. Wind speeds remained low for most other lenses measured on radar and given the results previously discussed, wind direction did not seem to have an effect on lenses when speeds were 3 m s^{-1} or less. One lens, however, was measured at 6.2 m s^{-1} over the previous 3 hours. Winds were coming out of 310° and the corresponding front had the strongest signature, was tracked for longer than an hour, and propagated toward 58° at 0.12 m s^{-1}. These conditions would indeed create unstable frontal conditions analogous to the model results from Soloviev et al. (2015). Unfortunately with only one instance captured on radar it is not possible to say whether this theory generally applied to all lenses.

5.7. Freshwater and heat budget

5.7.1 Freshwater budget

The freshwater content of lenses observed at the ship was significantly correlated with the age of the patches (Table 5.2) and with the sum of precipitated rain volume derived from C-band radar, but also with the wind stress over the lenses over their presumed lifetime (assuming winds to be homogeneous to the location of the puddles). The precipitation history of each lens was therefore reflected in the freshwater content observed. This was further indicated by the significant correlation between the average salinity of a lens and the salinity inferred from radar precipitation, S_{rad}, where

$$S_{rad} = S\left(1 - \overline{V_{rad}}\frac{d_{rad}}{h}\right) \tag{5.1}$$

with S the ambient salinity, V_{rad} the average volume of rain fallen over the lens over the range of the radar, d_{rad} the duration of precipitation over the lens, and h the depth of FWLs. A dissipation time scale of FWLs, τ_S, was established by equating the change in salt content in a FWL with the salt flux F_S through its base and the time evolution of salinity:

$$\frac{d}{dt}\iiint S\ dxdydz = F_S\ \Delta x \Delta y \tag{5.2}$$

$$\frac{\partial S}{\partial t} = \frac{\partial}{\partial z}K_S\frac{\partial S}{\partial z} \tag{5.3}$$

and with broad assumptions,

$$\frac{\Delta S}{\Delta t}h = K_S\frac{dS}{dz} \tag{5.4}$$

where K_S is the salt diffusivity and is assumed equal to the heat diffusivity K_T:

$$K_S = K_T = \frac{\overline{\chi_{FWL}}}{2\ {T_z}^2}. \tag{5.5}$$

Substituting Δt for τ_S in 5.4 to designate a dissipation time scale derived from salt content, and using ΔS, results in

$$\tau_S = \frac{\Delta S \; h}{K_S \; S_Z} \tag{5.6}$$

This oversimplified time scale provides bounds on the amount of rain water, R_L, expected to remain in a FWL after precipitation and before observation, where

$$R_L = \sum V_{rad} \left(1 - \frac{t_{rad}}{\tau_S}\right). \tag{5.7}$$

and t_{rad} is the time in hours between the rain event and the observation of the FWL at the ship.

Larger fresh water content suggested some puddles were older than the radar range allowed to track (Figure 5.12). A greater freshwater content than measured by radar was also reported in the study from Wijesekera et al. (1999). They suggested an underestimation of radar measurements as a possible explanation. Another possible source of error was the assumption of constant surface current speed and direction, unaffected by winds over 150 km and over 48 hours, which we know to be inaccurate, leading to inaccurate accumulation of radar rain volume.

The dissipation time scale not only helped to account for the rain water believed to remain in each lens when we measured them but also provided a tool to forecast its persistence. We predicted that these FWLs would take an average of 3 days (but up to 22 days) for their salt anomalies to dissipate via constant mixing only. Changes in wind stress and current shear are however expected to modify their dissipation time.

5.7.2 Heat budget

Warm or cool temperature anomalies

FWLs are often cooler than surrounding ocean water (Figure 5.11). Four lenses were however warmer than ambient water independently of the recent net surface heat flux regimes and had a persisting warm interior through the night. Lenses with a positive temperature anomaly were measured in an environment made of relatively older precipitation patches (Figure 5.13, left panels). The presence of precipitation 8-24+ hours old at noon local time suggest that a large proportion of the surface waters had been warming in the past six hours. Parcels older than 18 hours were also subject to the previous diurnal cycle. Figure 5.13d shows the cumulative rain volume and instantaneous precipitation age in a 2-km box following the path of a warm water lens. It shows that the last significant rain shower occurred approximately 18 hours earlier, and another minor event 7 hours prior. This explains the pattern of fairly old rain, which has had time to warm under the sun. The ability of FWL to retain heat was previously described by Anderson and Weller (1996). They highlighted the increased coupling between the atmosphere and upper ocean through rain-induced shallow mixed layer depth, therefore increasing the ability of FWLs to accumulate heat.

Lenses with a negative temperature anomaly that had received a cooling heat flux were in an environment made up of precipitation younger than 6 hours. The example provided on Figure 5.13 (right panels, lens C) shows continuing precipitation between -28 and -12 hours, and another rain event starting two hours prior to observation (at 0300, local time). This lens was observed mostly at night and may have cooled further than when it was originally formed.

FWLs with a negative temperature anomaly that were subjected to recent warming had a precipitation environment made up of both young and old patches (Figure 5.13, center column). The precipitation history of a representative lens, D, showed that it was

formed approximately 45 hours prior to observation, but with only a minute amount of rainfall. Lens D received new precipitation about every 10 hours as the instantaneous age is seen regularly decreasing, but was then subject to more warming. The cumulative volume increased significantly with each new precipitation. When we observed this lens (at t = 0 hr), it was composed of four different rain events in the span of 45 hours, before receiving a new downpour around t = +4 hrs. Superposition of puddles within a lens was also suggested by Price (1979).

Composite nature of lenses

Lens D illustrates the composite nature that these lenses can display. The subsurface measurements of lens D are pictured in detail on Figure 5.14 and show at least two rain events. It features a sharp, turbulent front at the leading edge with a warm spike indicating convergence and downwelling (Figure 5.14c). T0.1 reached 30.5℃ but this heat remained confined near the surface. T1.5 barely sampled through this warm layer before a wind event around 0930 mixed this warm water down. A large downpour around 1030 added cooler water which again remained above T1.5. A warmer remnant from initial formation was therefore isolated between the fresher, cooler surface and the saltier, cool water underneath. This temperature inversion was also observed for a short time around 1530. (Another possible source for this surface cold water is nighttime cooling which remained confined at the lens surface.) The trapped warm layer inhibited this cooled water from mixing downward from convection. The lens' dissipation was therefore not always modulated by nighttime mixing. Wind stress persisted several hours and the cooler surface water was mixed downward, eroding the warmer layer.

This unstable temperature structure was maintained by the stabilizing salt stratification. A large and sudden wind event starting at 1700 effectively destroyed the salt structure by mixing first freshwater downward (freshening between 1700-1730) then

mixing salty water from underneath the lens (1730-1800) and homogenizing temperature.

Heat content

Lens D showed that large precipitating clouds could form lenses which not only persist for a long time, but which also have a stratification such that they can be heated more than ambient water. Subsequent precipitation over existing lenses can change the temperature and salinity structure of the existing lens but the most recent rain pool will remain separated from the initial lens until mixing works to dilute it. Outside of this smaller, newer patch, heat had remained trapped mid-depth due to stratification. This pattern of trapped heat was also observed in lenses with positive temperature anomalies throughout. The dissipation of temperature variance (Figure 5.14f) also illustrates the different "pockets" of freshwater, whether warm or cool.

The heating rate inside lenses was three times larger at T0.1 ($5.6e^{-4}$ ℃/min) and twice as large at T1.5 ($2.4e^{-4}$ ℃/min) compared to an average heating rate outside lenses ($1.6e^{-4}$ ℃/min at T0.1 and $1.1e^{-4}$℃/min at T1.5) based on four consecutive lens-free days. A dissipation time analog to τ_S was derived for temperature, τ_T, using χ, ΔT, and T_z. The average lifetime of FWLs was about 5 days (but up to 28 days), again based on constant mixing only. The realistic dissipation time of lenses would take into account shear and convective instabilities and should therefore be shorter.

The consequences of this capacity of freshwater lenses to retain heat or confine nighttime cooling and of their composite nature is an ocean surface made up of patches of different size and temperature (Figure 5.13), based on the amount and age of precipitation, which can last several hours to several days.

More than concentrating heat at the surface and making it readily available to the atmosphere, the barrier created mid-depth within lenses prevented nighttime convection from releasing heat accumulated during the day by penetrating sunlight and contributed

to warming the ocean's interior. This would have important climatic consequences as this would store more heat which could in turn aid to fuel more numerous or more intense storms in the equatorial regions, like Madden-Julian Oscillations.

5.8. Summary

Twenty-six freshwater lenses were identified in a data set collected in the equatorial Indian Ocean during 34 days of the DYNAMO experiment in 2011. Lenses' characteristics were very variables in size, depth, freshness, temperature, and age. A patch could be as long as 65 km and 4-20 m deep, be observed over 24 hours, and be 38 hours old, or it could be forming as it was observed with simultaneous rainfall. They could be up to 1.2 psu fresher at the surface and be either warmer or cooler than ambient water.

FWLs structure could be organized with a sharp front on the leading or trailing edge (or both), and display features analogous to buoyant gravity currents. They could also be very disorganized without fronts but with several "pockets" of different temperature and / or salinity.

Ten fronts were seen propagating on X-Band radar with velocity corresponding to gravity current speed $\sqrt{g'h}$. As lenses formed, their temperature and salinity anomalies correlated well with wind speed and rain volume. Once lenses were formed, weaker anomalies seemed related to stronger wind speed, also inducing elevated temperature dissipation. High turbulence was however not necessarily related to high wind speed, indicating a mixing regime independent of recent atmospheric conditions.

The freshwater content of FWLs was explained by the sum of accumulated precipitation over their lifetime, as measured by C-Band radar. A number of FWLs were also found to contain more freshwater than the amount accumulated over the past 48hrs, suggesting they were formed more than 2 days earlier.

Lenses were initially cold, and could be entirely cold at the time of observations, but a number of lenses were a mix of cold and warm pockets. This suggested that new precipitation had fallen atop a preexisting, warm lens and formed a newer, cooler, fresher pocket within. These lenses had been formed 5+ hours prior to observation but all featured precipitation within the last hour.

The patchy nature of precipitation in equatorial areas creates patchy temperatures not only at the surface but also at mid depth where heat was seen trapped within puddles due to their strong stratification, which isolates them from the ambient. This caused a lens' heating rate to be 2-3 times higher than in the ambient. More than simply confining heat inside lenses, heat underneath lenses accumulated throughout the day by penetrating sunlight was isolated from the surface, which would contribute to an overall warming of the ocean's interior. As FWLs were estimated to be up to two days old, and to take an average of two to three days to dissipate through turbulent mixing, the equatorial Indian Ocean has the ability to store heat in its interior until a large and strong storm like an MJO is able to reinstate a deeper, cooler mixed layer, resetting the system.

5.9. Acknowledgements

We are grateful to James B. Edson for sharing the meteorological and air-sea heat fluxes. X-band images were provided by Tony Di Paolo, C-band images by Elizabeth J. Thompson. Relative front propagation velocity were obtained from the suggestions of Martín Hoecker-Martínez

5.10. Tables and Figures

TABLE 5.1: Significant relation between freshwater lenses and their environment. Twenty five precipitation events with their respective effect on the ocean were observed (N=25, $\alpha = 0.05$, R_{crit}=0.41, where N is the number of samples, and R_crit is the level of significant correlation based on N). δS and δT are the S and T anomalies of the FWL with respect to their surrounding water, dS/dt and dT/dt are the freshening and cooling rates, V_{rain} is the total volume of rain accumulated during the rain event (mm), and τ the wind stress.

Correlated pairs		R	p-value
During precipitation			
δS_{TSG}	V_{rain}	-0.60	0.0016
δT_{SNK}	V_{rain}	-0.51	0.009
dS_{TSG}/dt	V_{rain}	-0.74	0.00002
τ	dT_{SNK}/dt	0.58	0.002

TABLE 5.2: Significant relation between freshwater lenses and their environment. Twenty six formed lenses were advected past the ship (N=26, $\alpha = 0.05$, R_{crit}=0.40, where N is the number of samples, and R_crit is the level of significant correlation based on N). $\sum P_{radar}$ is the total precipitation accumulated over the FWL over the previous 48 hrs (mm), Z_{FW} is the freshwater thickness of lenses (mm), τ the wind stress, S_{AVG} the average salinity over the FWLS, S_{RADAR} the salinity of lenses predicted from radar precipitation, T_Z the temperature gradient, and J_q^0 the net surface heat flux.

Correlated pairs		R	p-value
Formed lenses			
$\sum P_{radar}$	Z_{FW}	0.54	0.004
τ	Z_{FW}	0.51	0.008
age	Z_{FW}	0.51	0.008
time since last precip.	Z_{FW}	0.74	0.00001
S_{AVG}	S_{RADAR}	0.58	0.002
T_Z	J_q^0	-0.61	0.0009

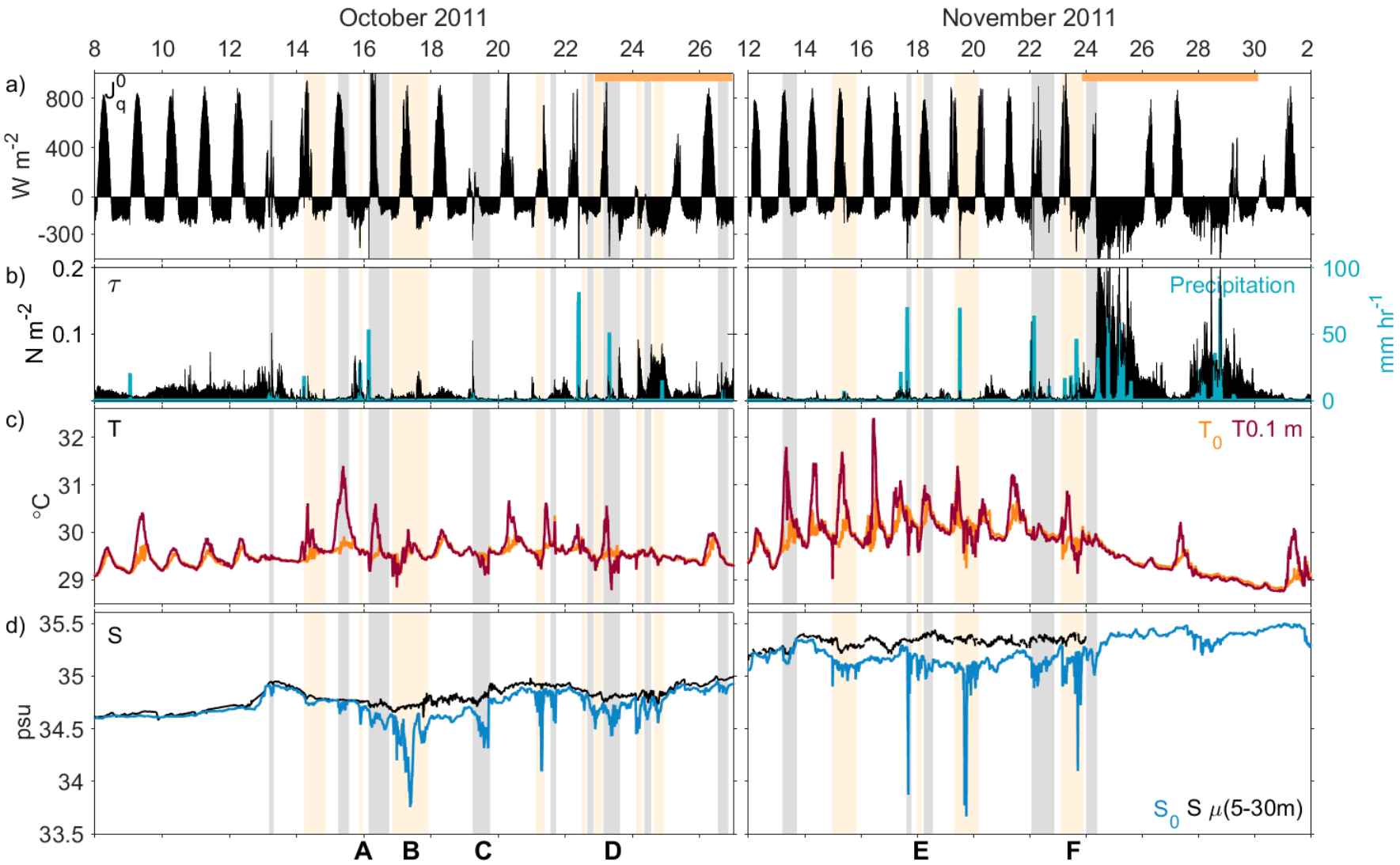

FIGURE 5.1: Overall atmospheric and surface oceanic conditions during DYNAMO Leg2 and Leg3. (a) Net surface heat flux positive into the ocean ($W\ m^{-2}$); (b) Wind stress (black, left axis, $N\ m^{-2}$) and precipitation (grey, right axis, $mm\ hr^{-1}$); (c) Temperature at 0.1 m (SST) and the ship's thermosalinograph (T_0) m (°C), and (d) Salinity from the ship (S_0), and the average salinity from 5-30 m (psu). The alternating vertical shaded bands represent the observation times of FWLs at the ship, the orange bars at the top of panel a) represent MJOs passing over the ship, and the bold letters A-F at the bottom indicate the lenses discussed in this paper.

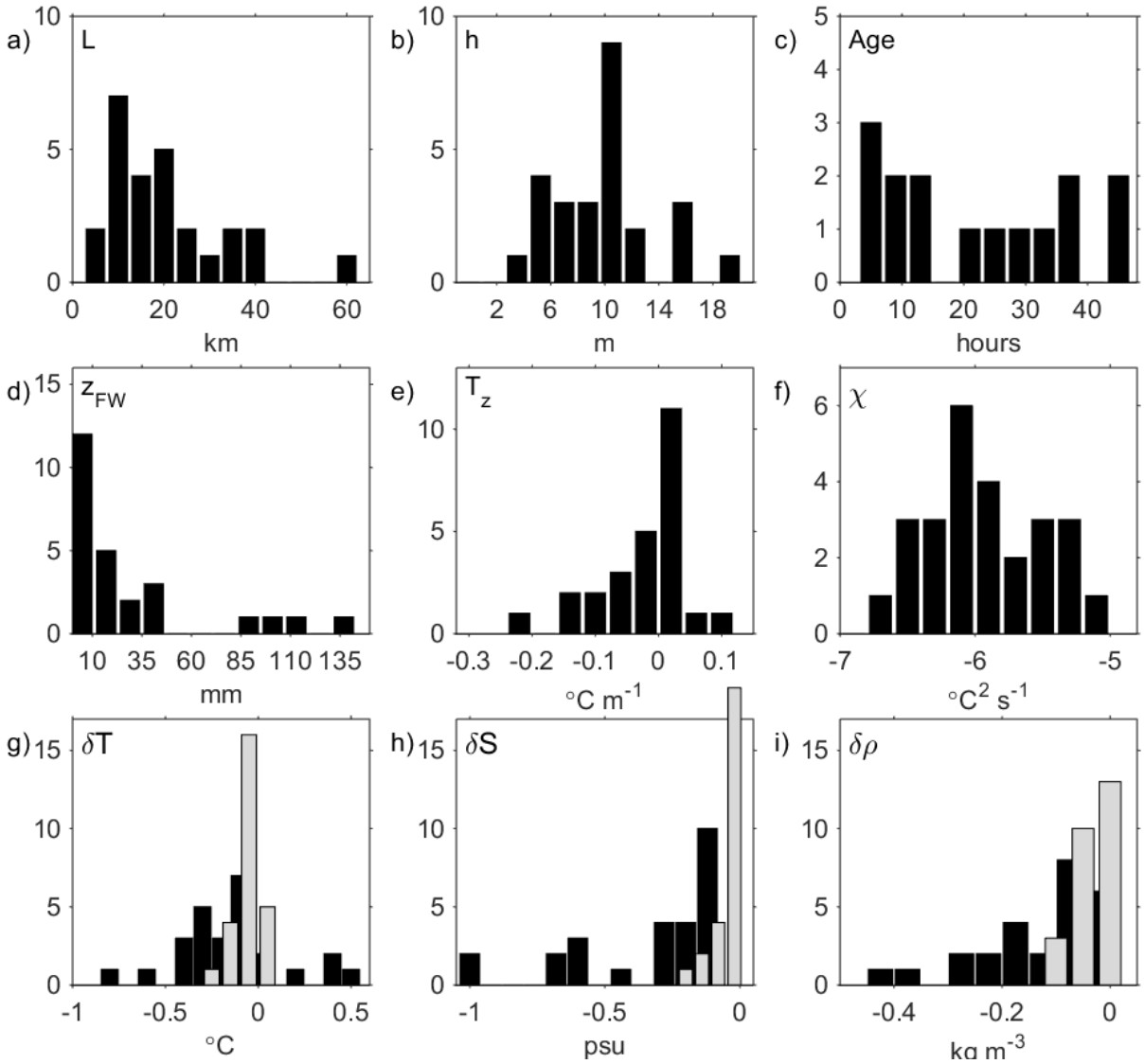

FIGURE 5.2: Histograms of lenses characteristics with (a) their length L (km); (b) depth h (m); (c) age (hrs); (d) freshwater thickness to recover 90% of their salinity anomaly, Z_{FW} (mm); (e) temperature gradient (℃m^{-1}), (f) log_{10} of the dissipation of temperature variance, χ (℃$^2s^{-1}$), (g) temperature anomalies measured by the ship T_0 (black) and averaged over the entire FWL (grey); (h) salinity anomalies measured by the TSG (S_0, black) and averaged over the FWL (grey), and (i) density anomalies measured by the TSG (ρ_0, black) and averaged over the FWL (grey).

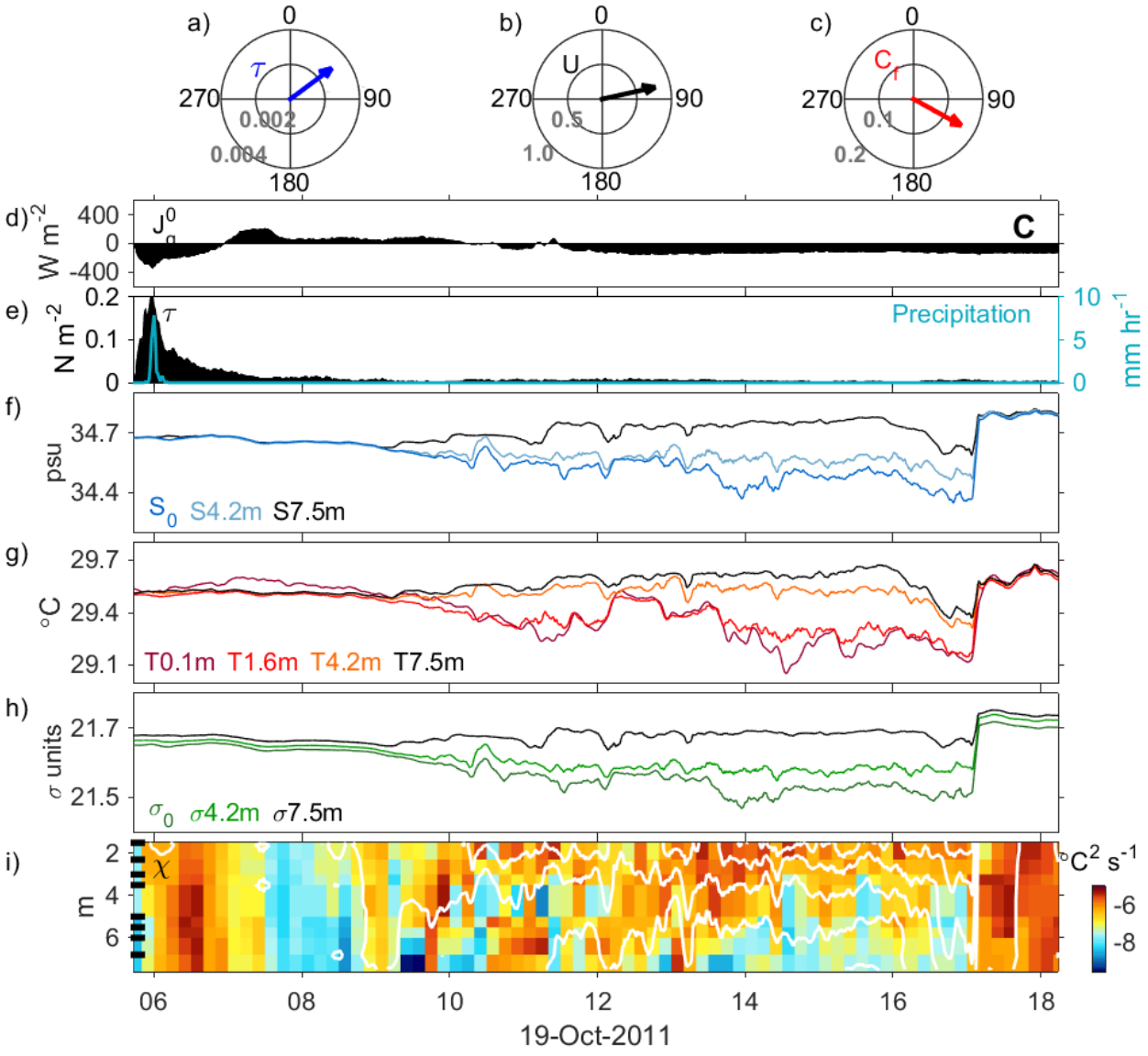

FIGURE 5.3: Structure of lens C. (a) The wind stress; (b) current velocity; (c) front velocity; (d) Net surface heat flux positive into the ocean (Wm^{-2}); (e) wind stress (black, left axis, Nm^{-2}) and precipitation (blue, right axis, $mmhr^{-1}$); (f) Salinity (psu); (g) Temperature (℃); (h) Density (kg m^{-3}), and (i) log_{10} of the dissipation of temperature variance, χ ($℃^2 s^{-1}$) overlaid by temperature contours in white.

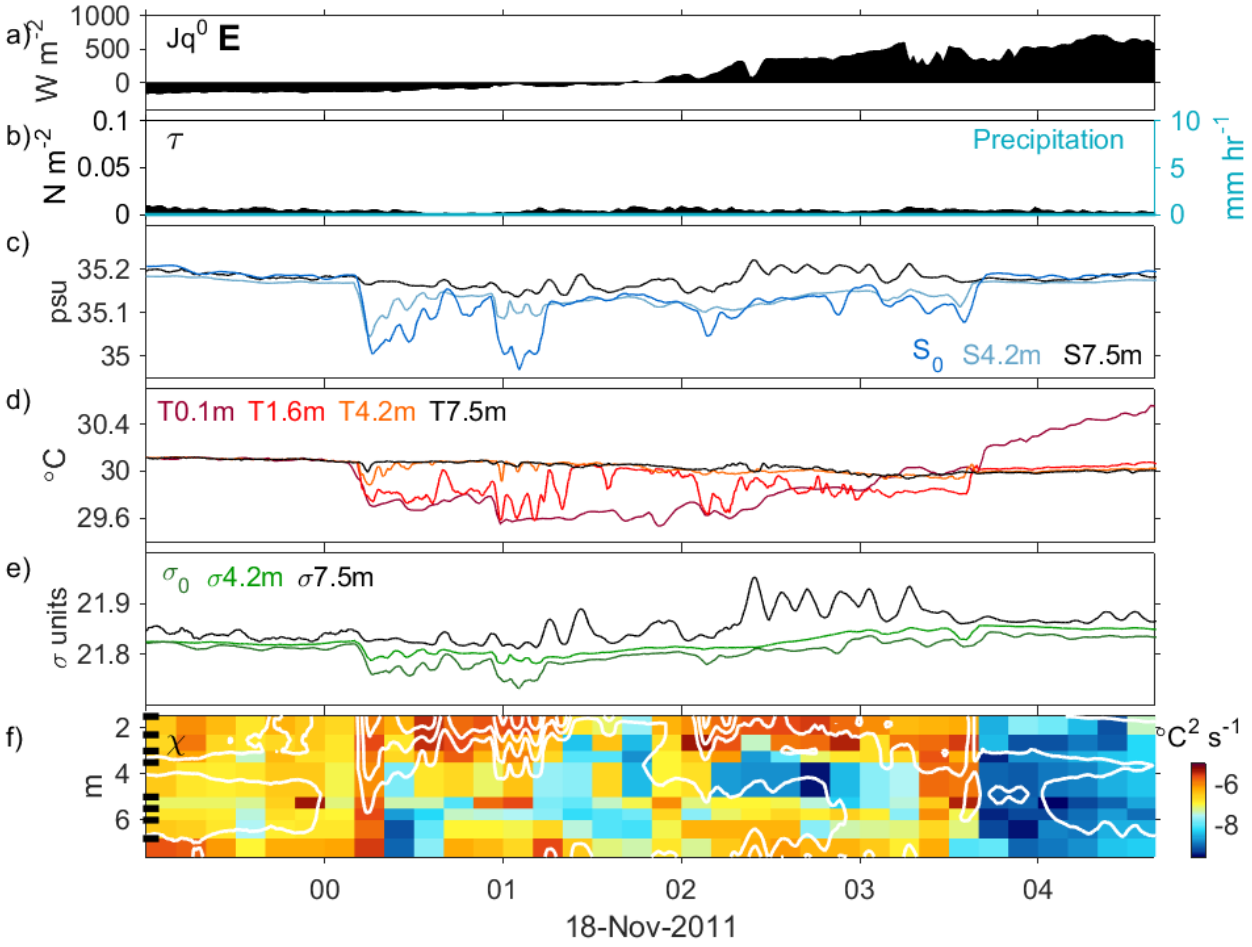

FIGURE 5.4: Structure of lens E. (a) Net surface heat flux positive into the ocean (Wm^{-2}); (b) wind stress (black, left axis, Nm^{-2}) and precipitation (blue, right axis, $mmhr^{-1}$); (c) Salinity (psu); (d) Temperature (°C); (e) Density (kg m^{-3}), and (f) log_{10} of the dissipation of temperature variance, χ (°C$^2 s^{-1}$) overlaid by temperature contours in white.

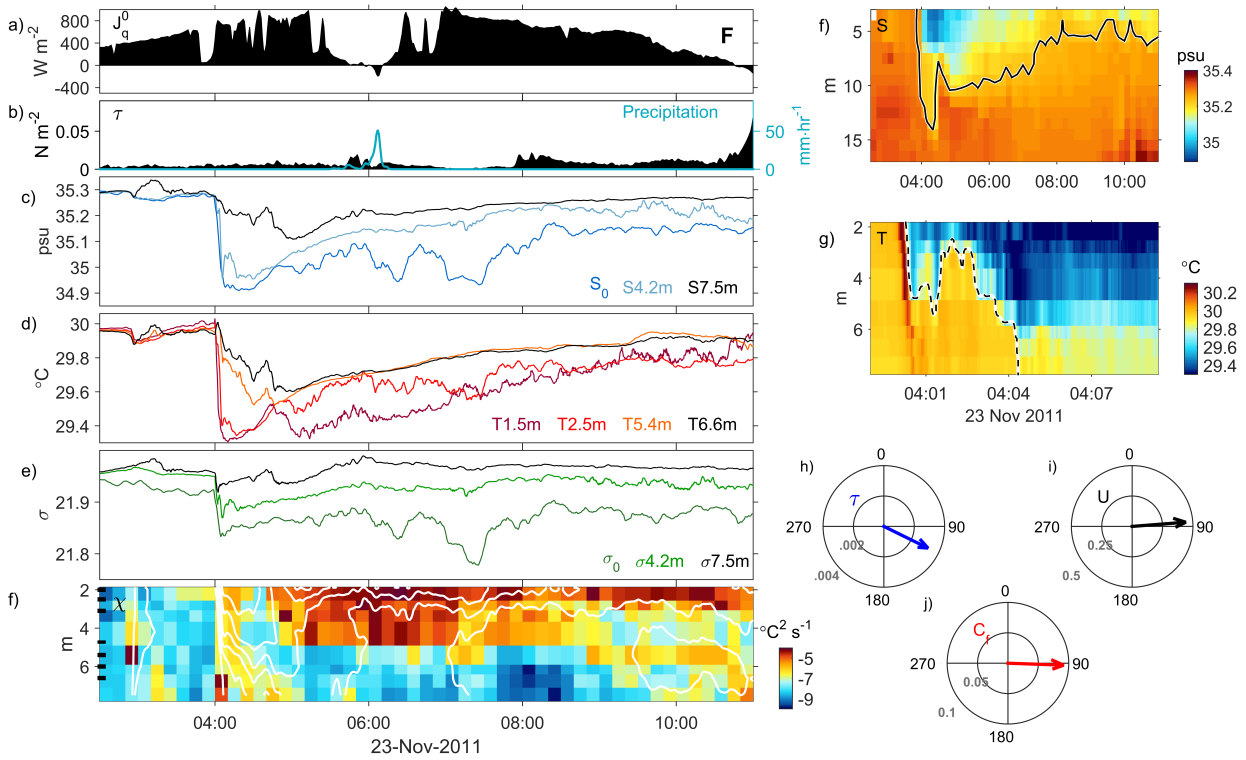

FIGURE 5.5: Structures of lens F (a) Net surface heat flux positive into the ocean ($W\ m^{-2}$); (b) wind stress (black, left axis, $N\ m^{-2}$) and precipitation (blue, right axis, $mm\ hr^{-1}$); (c) Salinity (psu); (d) Temperature (℃); (e) Density (kg m^{-3}); (f) log_{10} of the dissipation of temperature variance, χ (℃$^2 s^{-1}$) overlaid by temperature contours in white; (g) Salinity structure of the upper 17 m; (h) Temperature structure of the upper 8 m; (i) wind stress; (j) current velocity; and (k) front velocity.

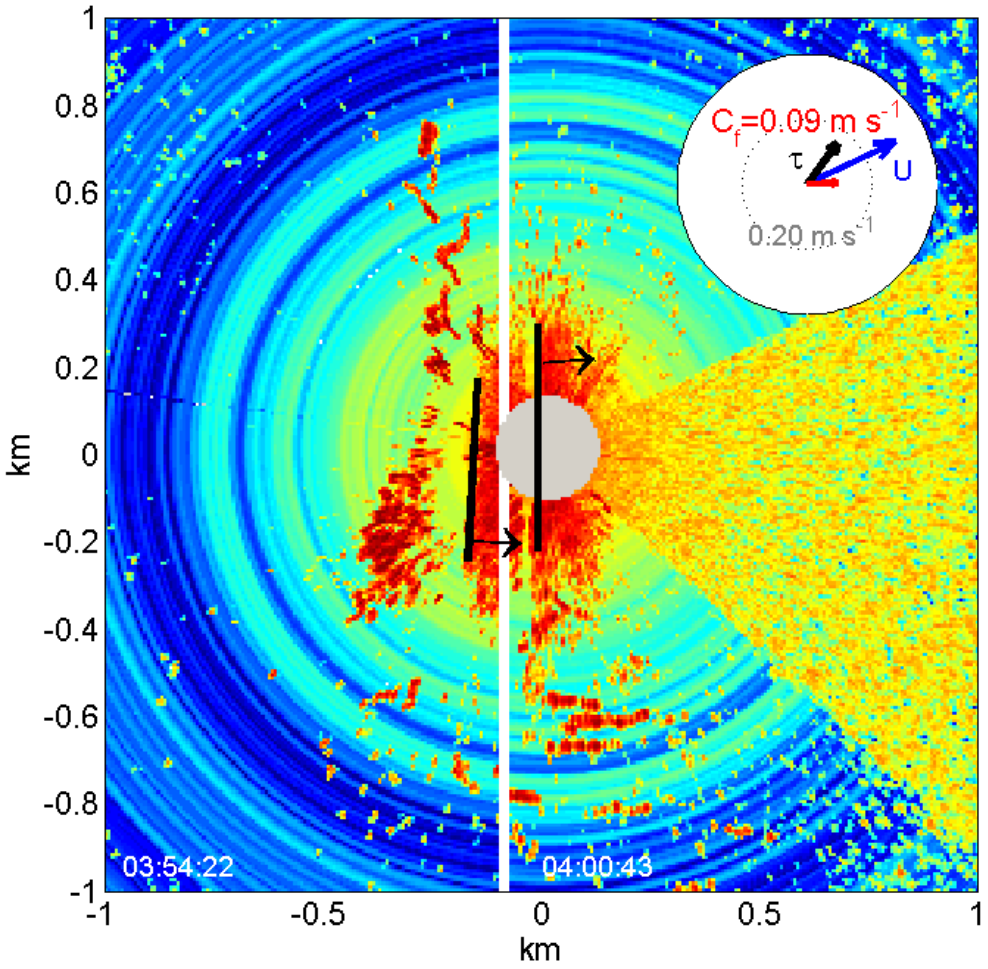

FIGURE 5.6: X-Band radar images of 15-sec variance of sea surface roughness at 03:54:22 (left) and 04:00:43 (right). The thick black lines depict the location of the front from lens F (Figure 5.5) at two different times propagating in the direction of the black arrows. The ship is at the center of the grey circle. The arrival time of the front at the ship coincided with the subsurface measurement of the lens. The wind stress magnitude and direction is shown as a black arrow on the compass in the top right corner, with the ocean velocity in blue and the resulting front velocity and direction in red. The large cone on the right is the shadow of the ship's smoke stack obstructing the radar. Some of the strong target on the left side of the fronts were seen moving quickly in and out the frontal area. They were believed to be fish feeding on plankton possibly trapped at the surface in the convergence zone (therefore supporting the presence of lobes and clefts).

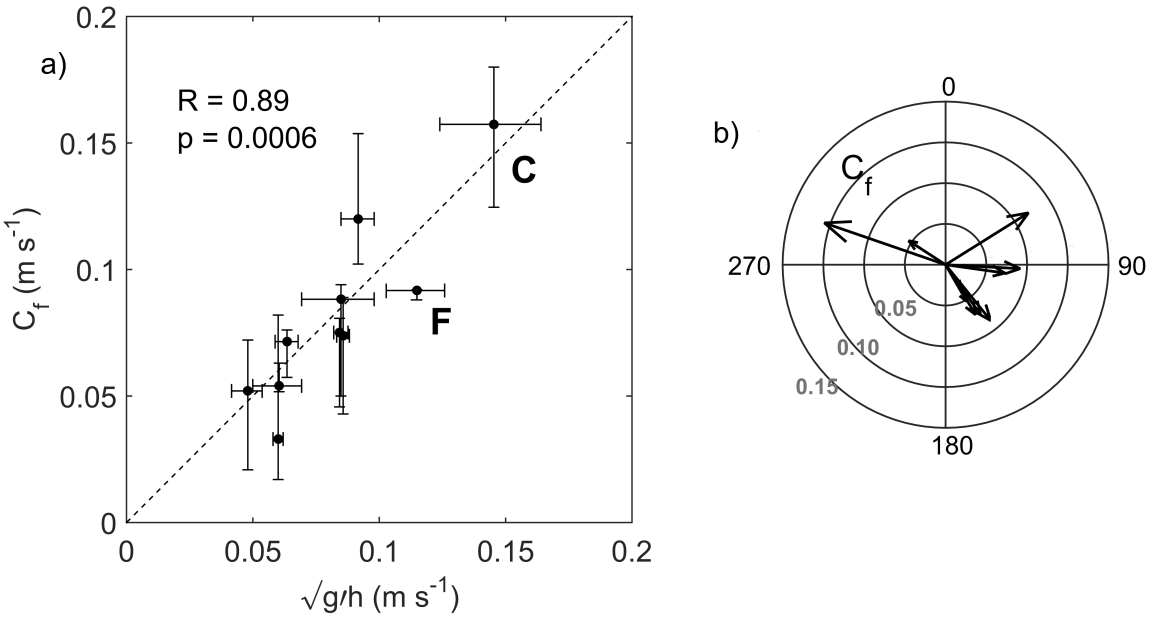

FIGURE 5.7: (a) Scatter plot of the theoretical wave speed fron linear theory, $\sqrt{g'h}$ versus the front velocities measured from X-Band radar images. The error bars result from uncertainties in frontal density and depth, and in the precise location of fronts on radar images. Lenses C (Figure 5.3) and F (Figure 5.5) are indicated. (b) Summary compass diagram of the ten fronts observed propagating on X-Band radar. Direction in degrees and velocity in m s^{-1}

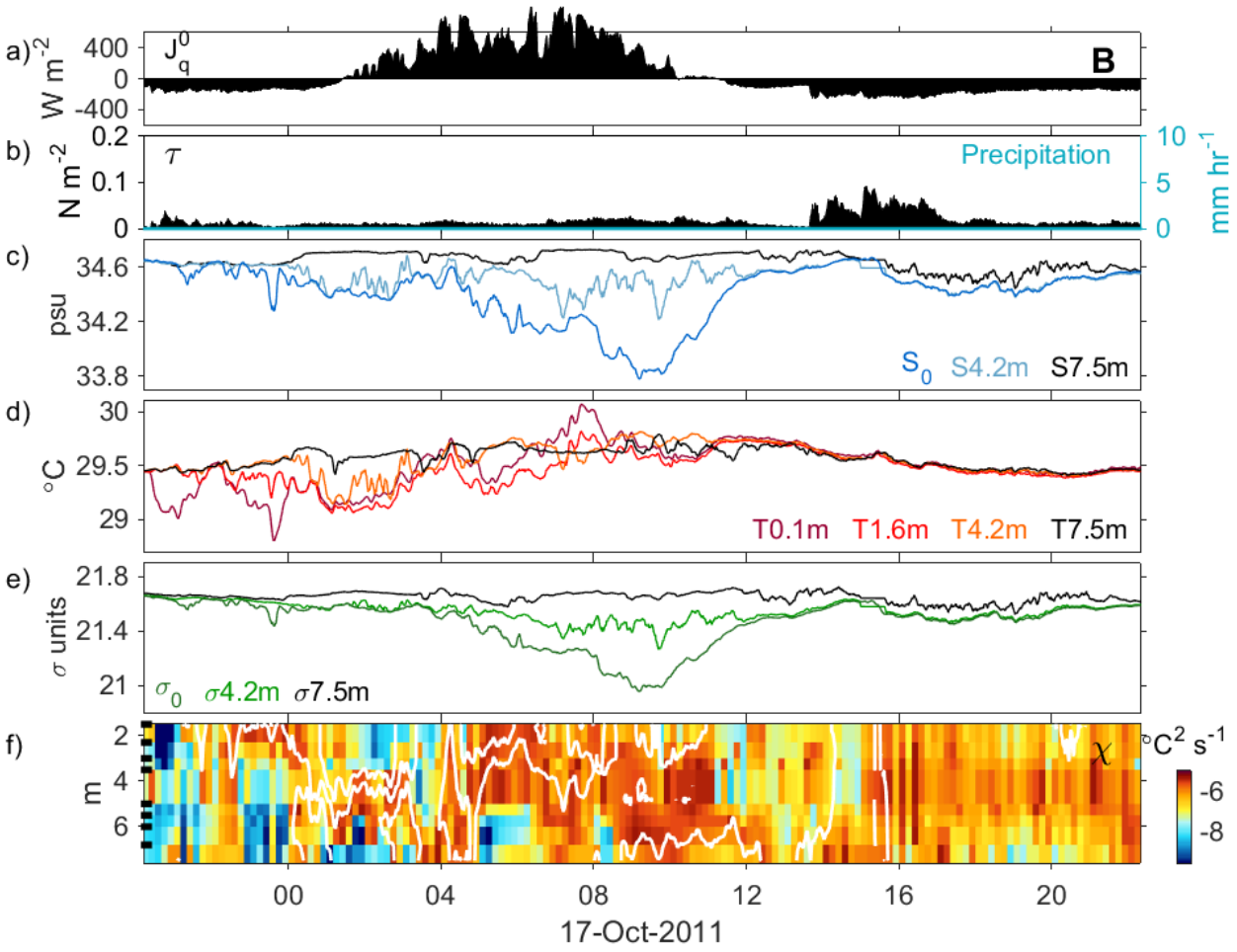

FIGURE 5.8: Structure of lens B. (a) Net surface heat flux positive into the ocean (Wm^{-2}); (b) wind stress (black, left axis, Nm^{-2}) and precipitation (blue, right axis, $mmhr^{-1}$); (c) Salinity (psu); (d) Temperature (°C); (e) Density (kg m^{-3}), and (f) log_{10} of the dissipation of temperature variance, χ (°C$^2 s^{-1}$) overlaid by temperature contours in white.

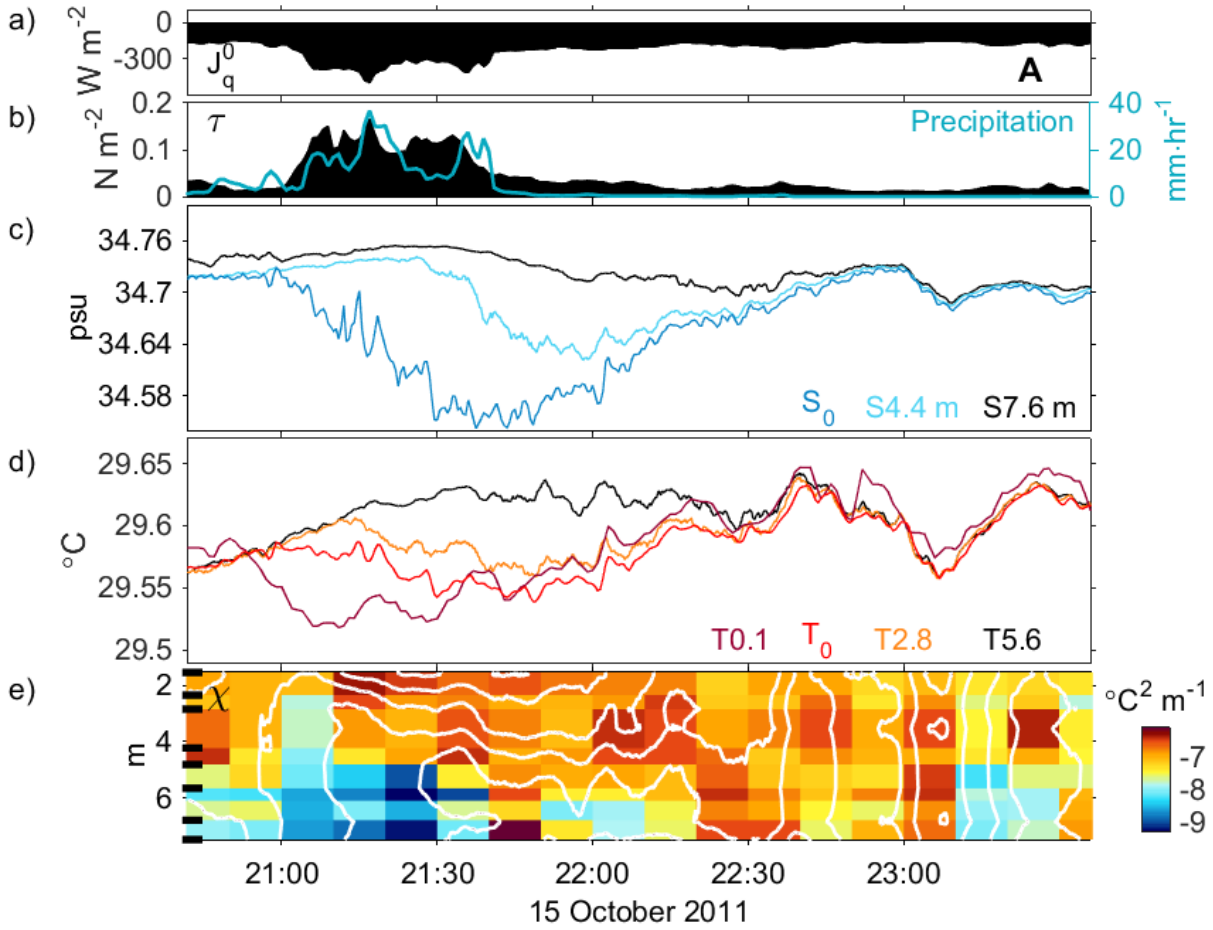

FIGURE 5.9: Characteristics of lens A with (a) Net surface heat flux positive into the ocean ($W\ m^{-2}$); (b) wind stress (black, left axis, $N\ m^{-2}$) and precipitation (blue, right axis, $mm\ hr^{-1}$); (c) Salinity (psu); (d) Temperature (℃), and e) log_{10} Dissipation of temperature variance, χ ($℃^2 s^{-1}$) overlaid by temperature contours in white.

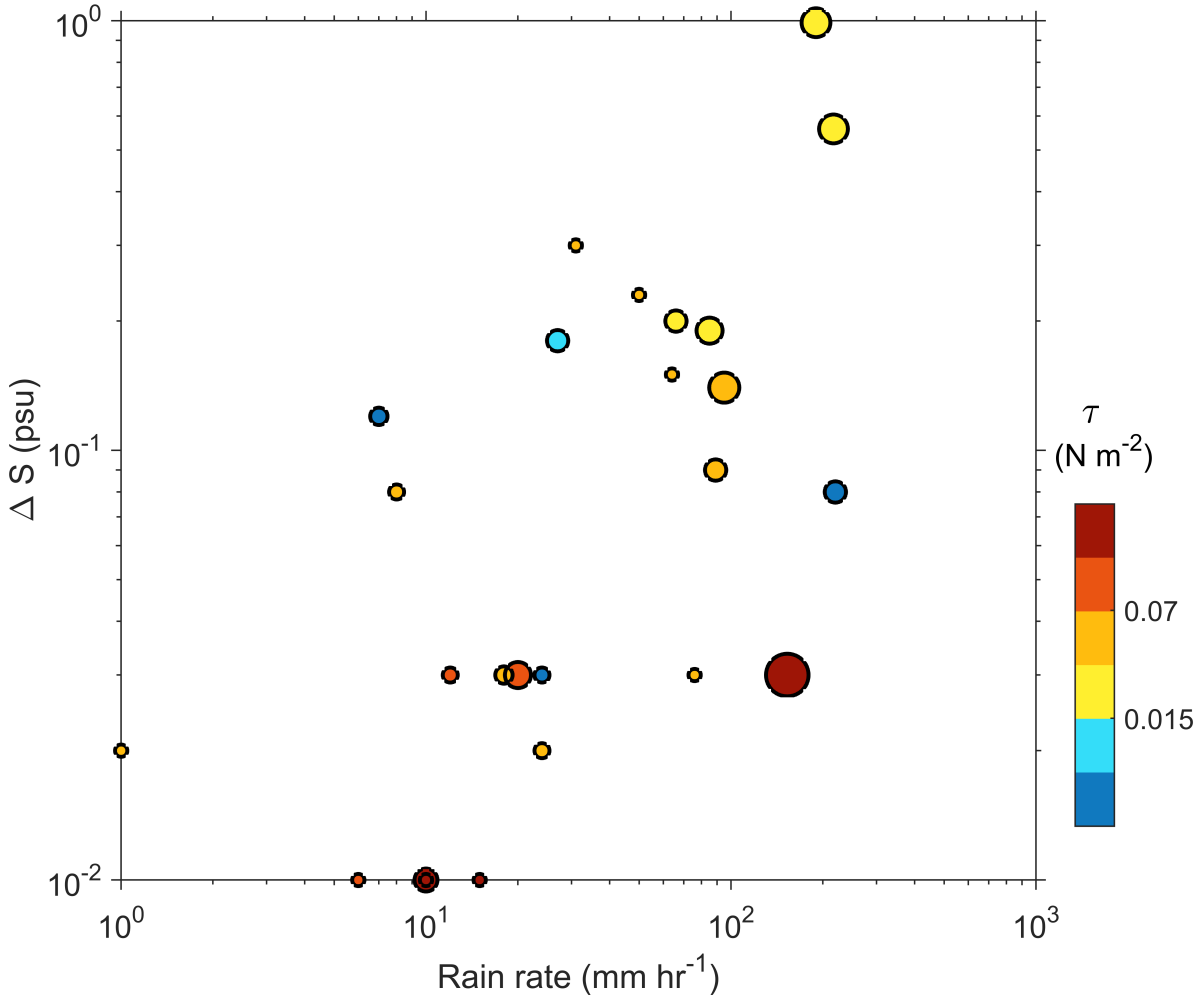

FIGURE 5.10: Scatter plot of rain rate (mm hr^{-1}) observed on the ship versus corresponding salinity anomalies measured from TSG at the end of precipitation events. Marker size reflects the duration of the storm and their color the average wind stress ($log_{10}\tau$) during the storm.

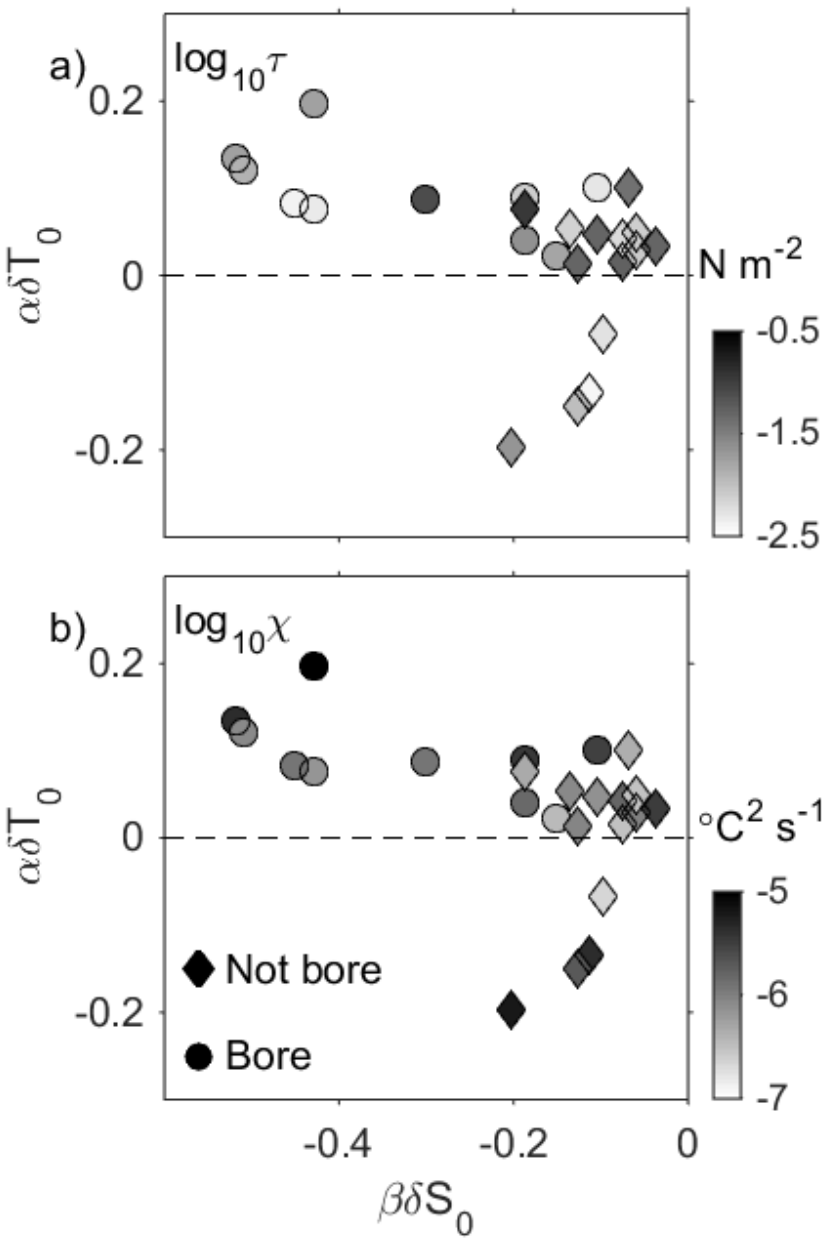

FIGURE 5.11: Scatter plots of the contribution of temperature measured at T_0 and salinity anomalies at S_0 to lens' density anomalies. Circles are bore-like lenses defined by the presence of a turbulent front on mixing estimates, diamonds do not present a turbulent front and are thought not to propagate. Markers are colored according to (a) wind stress ($N\ m^{-2}$), and (b) $log_{10}(\chi)$ $^{\circ}C^2 s^{-1}$.

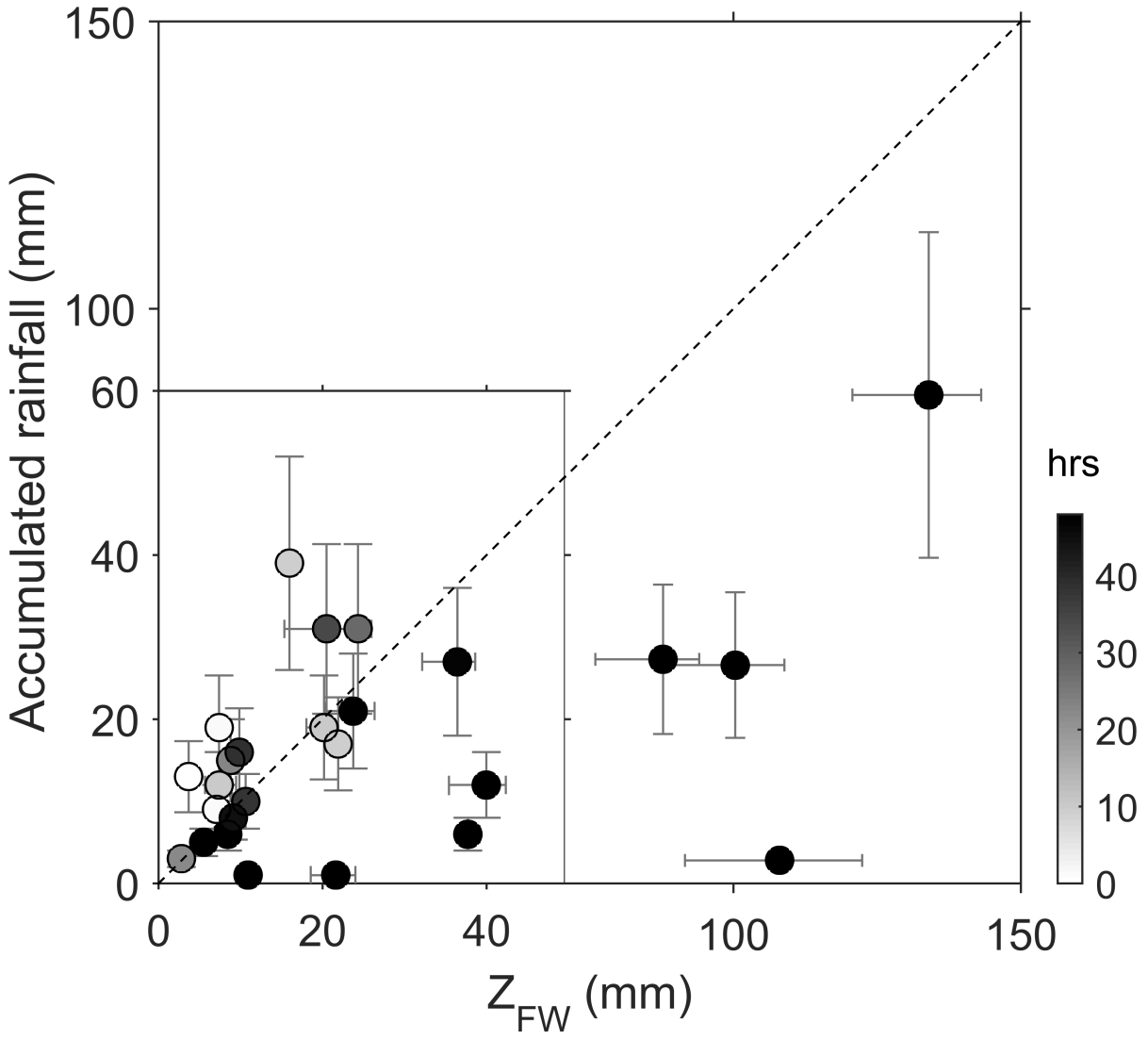

FIGURE 5.12: Scatter plot of the measured thickness of freshwater in lenses (Z_{FW}, mm) versus the accumulated rainfall measured from C-Band radar (mm). The markers are shaded according to their age. Errorbars are based on error on the depth of the isohaline representing 90% recovery of salinity anomalies, and in measurement errors from C-Band radar. The general tendency is for lenses below the 1:1 line to be older than 48 hours and therefore contain more freshwater than could be captured by C-Band radar.

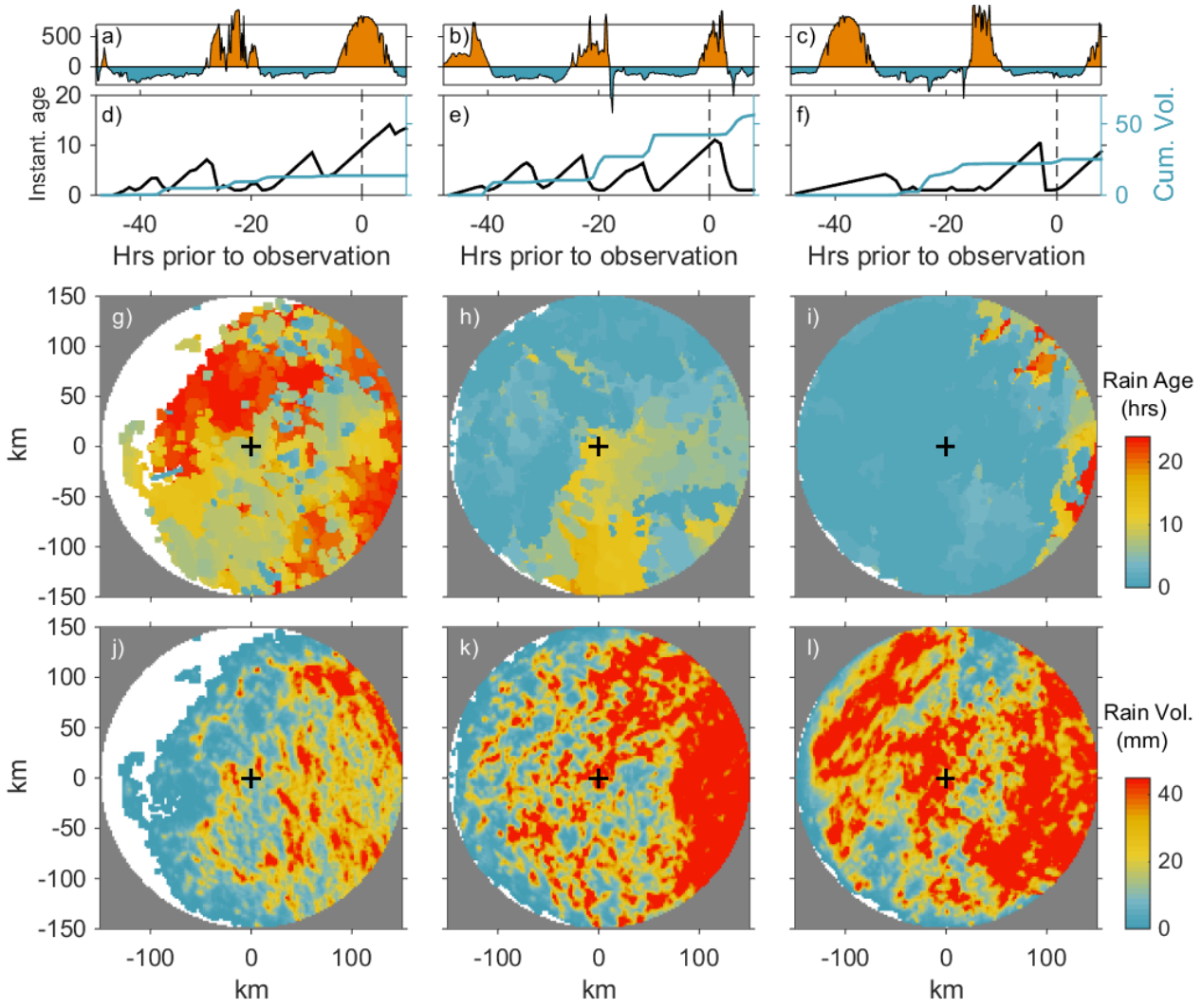

FIGURE 5.13: Comparison of three types of lenses each with a different precipitation history. (a-c) Net surface heat flux (Wm^{-2}); (d-f) 48-hr history and real-time observation of the time (hrs) since the parcel where the lens is located last received precipitation (black, left axis), and cumulative rain volume along the lens's path (blue, right axis, mm); (g-i) map of precipitation age at the time the lens reached the ship (hrs); (j-l) cumulative volume of precipitation over the past 48 hrs (mm). The intersection of dashed lines and curves on panels (d-f) correspond to the value read on maps from panels (g-i) and (j-k) in a 2 km box centered on the cross. Panels on the left represent lenses showing a positive temperature anomaly throughout the entire lens. Center panels represent lenses made of a succession of precipitation and warming time creating warm and cold pockets persisting through nighttime cooling. The particular lens shown is lens D pictured on Figure 5.14. Panels on the right illustrate lenses with a cold anomaly throughout the puddles, i.e. lens C from Figure 5.3. Details of the method used to make the age and volume maps are available in Appendix B

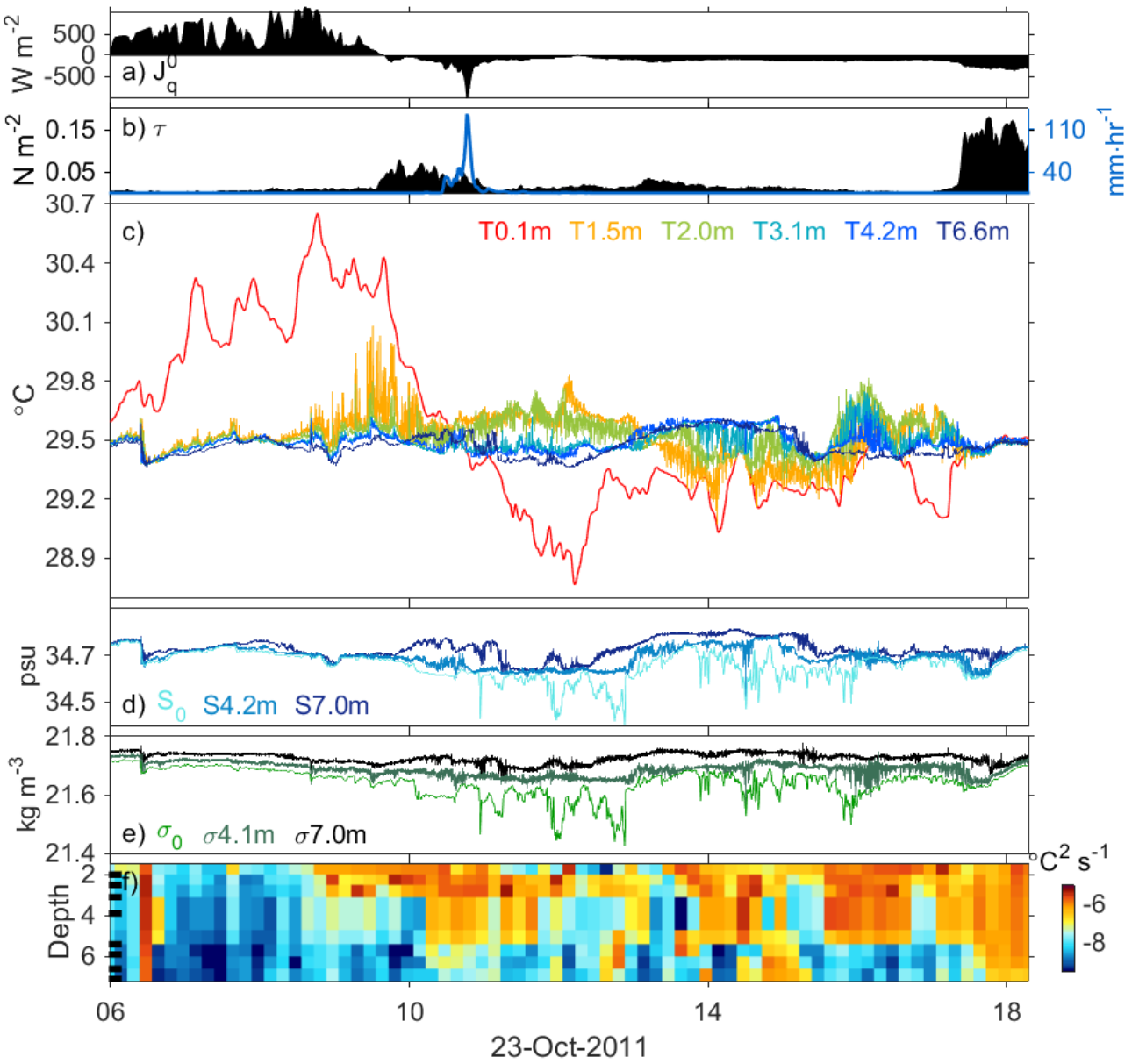

FIGURE 5.14: Characteristics of lens D with (a) Net surface heat flux positive into the ocean ($W\ m^{-2}$); (b) wind stress (black, left axis, $N\ m^{-2}$) and precipitation (blue, right axis, $mm\ hr^{-1}$); (c) Temperature (°C); (d) Salinity (psu); (e) Density (σ units); (f)$log_{10}\chi$ ($°C^2 s^{-1}$).

6. THESIS CONCLUSIONS

Two rich data sets collected at the equator in the Indian and Pacific oceans gave insights into the detailed evolution of temperature in the upper eight meters of the ocean with the deployment of a thermistor chain (T-chain) measuring the undisturbed diurnal warm layer temperature and salinity structure. The novelty of the bulk of the data used in this work necessitated the implementation of a method to obtain quality temperature gradients from discrete observations and to estimate turbulence. Three questions about the evolution of temperature and salinity structure were addressed with these data. Answers are summarized therein.

The daily cycle of turbulence in the upper ten meters was observed, quantified, and explained through a simple balance of the turbulent kinetic energy (TKE) equation. At night TKE dissipation was high from nighttime convective mixing and matched known scalings. Upon sunrise turbulence were abruptly terminated and TKE dissipation (ϵ) decayed at a rate proportional to the local buoyancy frequency. Building stratification in addition to accumulating shear from the wind reversed the trend in ϵ which then rapidly grew proportionally to a time scale based on the Law-of-the-Wall and buoyancy frequency. An equilibrium state was reached in the afternoon when buoyancy and shear production at the surface balanced out TKE dissipation at the base of the mixed layer. More work is needed to put bounds on the constant $\mathcal{C}$ modulating this scaling. The increased turbulence was thought to be generated by Kelvin-Helmholtz instabilities, indicated by the presence of skewed temperature ramps. Turbulence dissipation was higher by an order of magnitude when these temperature ramps were present. Finally these temperature features progressed in space and time over the course of a day: from a small number mostly near the surface in the morning to high occurrence throughout the top eight meters in the early evening.

In cases of moderate and sustained strong wind ϵ scaled relatively well with Law-of-the-Wall scaling in the afternoon. During low wind and strong stratification conditions however, ϵ exceeded this scaling by up to an order of magnitude which was thought to indicate the presence of a slippery diurnal jet.

During high winds, the presence of ramps did not lead to significantly different turbulence dissipation. Waves were higher, stratification weaker, these are conditions ideal for the development of Langmuir circulations. Although we were unable to resolve them with the available data, a clear relationship emerged when comparing ϵ to the temperature gradient. This relationship could suggest that Langmuir cells, Kelvin-Helmholtz instability and quiescent environment not only occupy a distinct log_{10} T_z - $log_{10}\epsilon$ space but also that they co-varied. More work to better quantify these relationships is needed but requires measurement of near surface velocity, something currently not available for these datasets.

The current understanding of diurnal warm layer (DWL) physics is represented in several parameterizations which all have strengths and weaknesses. Price-Weller-Pinkel (PWP) and COARE3.5 algorithms both performed well overall but some features were consistently misrepresented due to the inaccurate modeled shape of the temperature profile. Sea surface temperature was underestimated, the mixed layer depth evolution reasonable but the mixing scheme above inadequate when wind speeds were weak and intense diurnal warming occurred.

The evolution of the DWL near the surface depended on the progression of the turbulence profile previously described. After restratification and decoupling between upper and lower portions of the near surface layer, turbulence was enhanced throughout the day within the mixed layer, while turbulence below decayed. These tendencies persisted over the depth of the T-chain until late afternoon when the deepening mixed layer depth engulfed deeper instruments, then measuring comparable levels of turbulence over the

T-chain depth range.

The collapse of the diurnal warm layer was initiated by the local divergence of net surface cooling and absorbed solar radiation at the very surface mid-afternoon. As the depth where heating and cooling was compensated deepened, cooling from above destabilized the water column. The remaining heat trapped near the surface was mixed down while shear instabilities at the base of the mixed layer continued to entrain fluid, deepening the mixed layer and dissipating heat.

The heat anomalies (excess or deficit) compared to the local divergence of absorbed solar radiation corresponded to depths and times of enhanced turbulence providing an explanation for the anomalies. Large discrepancies existed between observed heat content and heat estimated from either a local or depth integrated budget. Models could be improved by redefining the profile shape resulting from poor mixing scheme fidelity in cases of weak winds.

Lastly, freshwater lenses were observed with different thermohaline and kinematic properties. They ranged from 2 - 40 km across, 2 - 15 m deep and featured temperature and salinity anomalies up to 1℃ and 1 psu. They could display an organized structure with a sharp front on either the leading or training edge (or both). Their convergent front propagated at the internal wave speed $\sqrt{g'h}$. Lenses were formed immediately after onset of precipitation with a progressively deeper temperature and salinity response. There was a weak relationship between rain rate and salinity anomaly when lenses were forming. They correlated poorly with a storm duration and weakly with the wind speed during the precipitating storm. Temperature and salinity of formed lenses were correlated. Small anomalies were found for lenses with highest wind speed and moderate to weak mixing. Lenses propagating as turbulent bores tended to feature more intense anomalies.

The measured freshwater content of lenses corroborated the freshwater volume pre-

cipitated over the lens' path during the last 48 hrs. Lenses with greater freshwater volume than precipitated were older than 48 hours, suggesting a persistence of lenses longer than two days.

The precipitation history of lenses could be reflected in their temperature structure with the observation of warm pockets trapped between salt stratified bases and fresh and cool newer precipitation above.

All the mechanisms defined throughout this work affect the upper ocean heat content by modulating the temperature structure, controlling the sea surface temperature, and affecting air-sea fluxes fueling storms, large and small.

APPENDICES

A Method to derive front propagation velocity from X-band radar images

The relative propagation speed of freshwater lenses front was obtained from X-band radar images. First the total propagation speed U_{tot} and direction U_{dir} was derived from differencing the front position between two frames. The directional components u_{tot} and v_{tot} and then subtracted from the observed current velocity component (u_{curr}, v_{curr}) to obtain the relative front propagation velocity (M. Hoecker-Martínez, personal communication).

$$u_{tot} = U_{tot} * sin(U_{dir}) \tag{A.1}$$

$$v_{tot} = U_{tot} * cos(U_{dir}) \tag{A.2}$$

$$u_{rel} = u_{tot} - u_{tot} * \frac{u_{tot} * u_{curr} + v_{tot} * v_{curr}}{\left(\sqrt{u_{tot}^2 + v_{tot}^2}\right)^2} \tag{A.3}$$

$$v_{rel} = v_{tot} - v_{tot} * \frac{u_{tot} * u_{curr} + v_{tot} * v_{curr}}{\left(\sqrt{u_{tot}^2 + v_{tot}^2}\right)^2} \tag{A.4}$$

A pair of X-band images and resulting front velocity is shown on Figure 0.1.

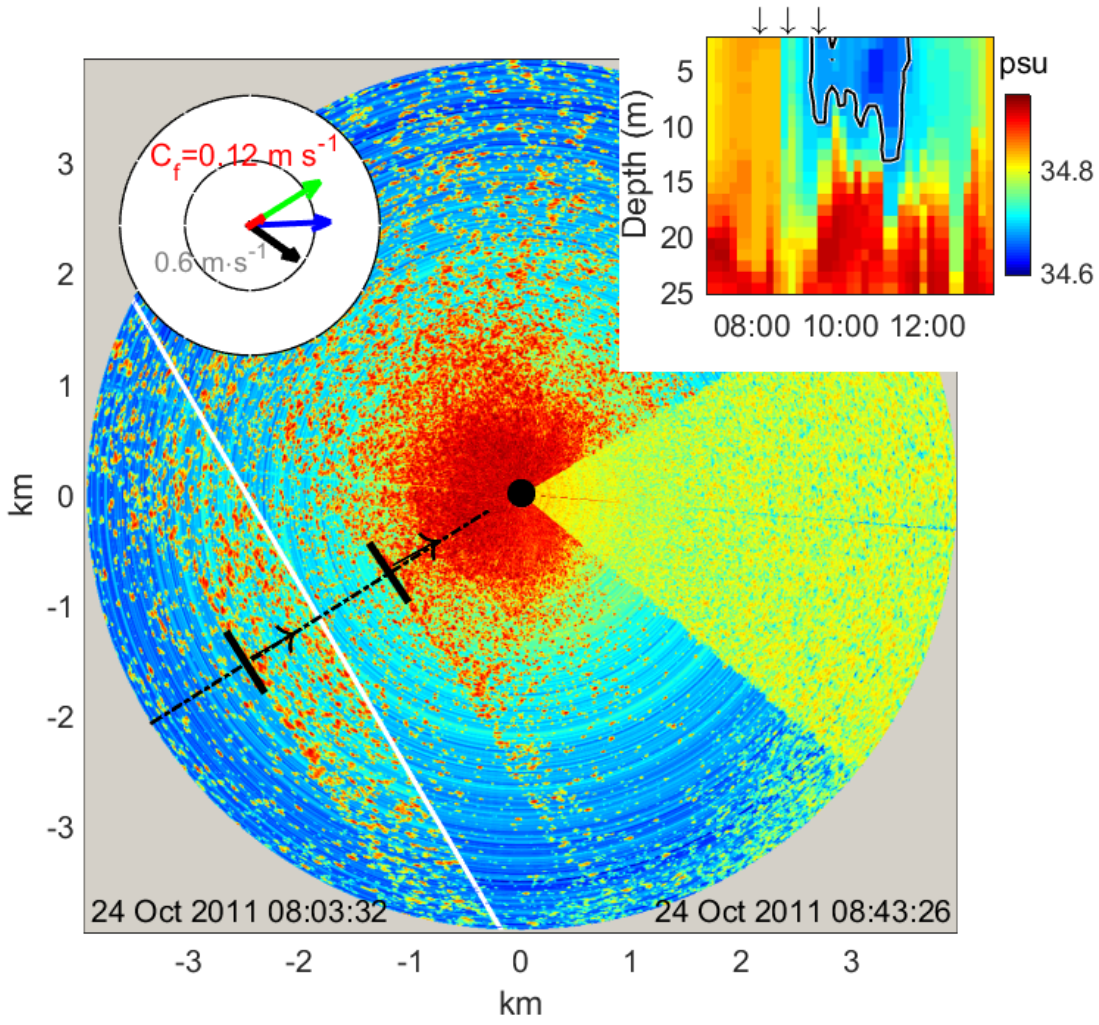

FIGURE 0.1: X-Band radar images of 15-sec variance of sea surface roughness at 08:03:32 (left) and 08:43:26 (right) on 24 October 2011. The thick black lines depict the location of the front from a FWL at two different times propagating in the direction of the black arrows. The ship is at the center of the black circle. The arrival time of the front at the ship coincided with the subsurface measurement of the lens. The wind stress magnitude and direction is shown as a black arrow on the compass in the top left corner, with the ocean velocity in blue, the propagation direction in green, and the resulting front velocity and direction in red. The large cone on the right is the shadow of the ship's smoke stack obstructing the radar.

B Method to derive precipitation history from C-band radar precipitation maps

Using maps of hourly accumulated rainfall compiled from C-Band reflectivity scans (Thompson et al. 2014, in review), ocean surface velocity, and the arrival time of lenses, we were able to reconstruct the cumulative volume, age, and precipitation duration over each lenss location since it entered the radar domain. This method relied on two assumptions, each discussed below, which we know are a source of errors but provide a reasonable guess.

B1 Radar assumption

The precipitation amounts within grid boxes were assumed constant. We know this to be inaccurate as the comparison of a 2-km gridded product showed differences with a 0.5 km product. However the finer resolution product only extended out to 50 km, which corresponded roughly to 17 hours of drifting distance. Moreover, the freshwater content of FWLs was significantly greater than what was forecasted by the finer precipitation maps while the coarser product correlated well. We concluded that FWLs were older than 17 hrs and therefore used the coarser product. The varying current speed led to hourly distances sometimes shorter than the 2-km grid resolution. For this reason the coarse 2-km precipitation data were linearly interpolated onto a 0.1 km grid.

B2 Ocean velocity assumption

The 150 km range from the C-band radar averaged to 48 hrs of drifting time before reaching the ship, considering an average current velocity 0.86 m s^{-1}. The precipitation history was therefore started 48 hrs prior to the arrival of a lens at the ship. It was delayed if u $\gg$0.86 m s^{-1} until the effective distance traveled was $\sim$150 km. The current velocity at any location [x,y] upstream 48 hrs prior to observation at the ship is the velocity measured at the ship 48 hrs later, assuming the velocity remained unchanged in this parcel. The current velocity used to translate gridded precipitation at time t-x hours

before observations was therefore the velocity measured at the ship at t+x hours.

B3 Compilation of age, volume, and precipitation duration

The assumption made about the near surface velocity allowed us to estimate the time and location of a lens when it entered the C-Band radar domain. The average of a 2-km box (on a 0.1 km linearly interpolated grid) centered on this location is used for each of the radar products derived. The 0.1-km grids for age, volume, and duration were initialized to 1, 0, and 0, respectively. At t=-48 hrs when the history is started, the hourly precipitation data were used to change the variables as follows:

- the age of every pixel with zero precipitation is increased by 1, the age of every pixel with non-zero precipitation is changed to 0;
- the volume of precipitation of pixels with non-zero precipitation increases by the hourly volume prescribed in each grid boxes while the volume of pixels receiving zero precipitation remains unchanged;
- the duration of precipitation of pixels with non-zero precipitation is increased by 1 while the pixels receiving no precipitation are unchanged.

Generally, an increase in age means that no precipitation is received, a drop in age means that new precipitation is falling within the 2-km box centered on the ship. An increase in precipitation duration means new rain has fallen. An increase in volume means new precipitation was added.

At t=-47 hrs, the grid which was altered by the precipitation volumes from t=-48 hours is translated according to the current speed and direction observed at the ship at that time. If the current speed is 0.5 m s^{-1} toward 90°, the grid is moved 0.5 m s^{-1} *3600 s = 1800 m east and 0 m north (or south). Eighteen columns of the 0.1 km grid along the eastern edge are eliminated, having moved out of the 150 km range; eighteen columns are added on the western edge, with age, volume, and duration again initialized at 1, 0, and

0 respectively. The precipitation volume from the map at t=-47 hr can then be applied to each grid cell as described above.

This method not only gave us the history of precipitation before the FWL reached the sensors, but also told us how precipitated volume measured by radar translated into subsurface signals as we also know the history of the parcels we are observing as the lenses are drifting by. A series of maps was produced for each lens, starting 48 hours prior to their arrival on subsurface sensors, and continuing over the observation period. An example is provided on Figure 0.2, which corresponds to lens D illustrated on Figure 5.14.

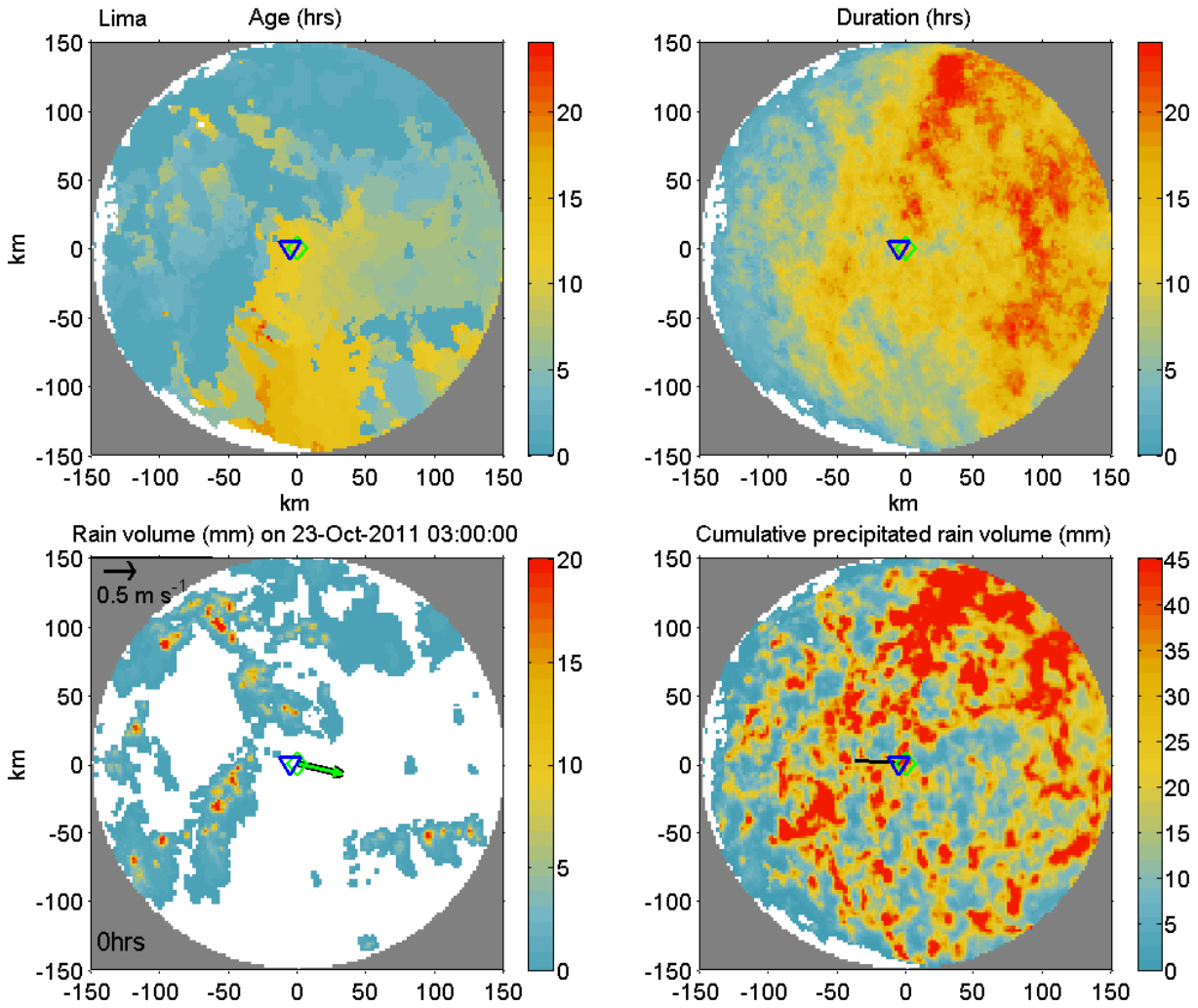

FIGURE 0.2: Frames used to estiamte FWLs rain content and history. a) Instantaneous time since last precipitation on the ocean's surface (hrs); b)Cumulative duration of precipitation (hrs); c) Rain volume (mm) precipitated over the hour starting at the time stamp on top the the panel. The green arrow shows the current velocity and the counter on the bottom left corner is the time prior to a lens arrival at the ship; d) Cumulative precipitated rain volume (mm). The black line represents the section of the map collocated to the length and time of lens Lima's observation. The green diamond represents the ship's position, the blue triangle the hourly position of the lens' leading front. The puddle reaches the ship when the diamond and triangle are superposed. The data are on a 0.1 km grid interpolated from a 2km grid.

BIBLIOGRAPHY

Anderson, J. E. and S. C. Riser, 2014: Near-surface variability of temperature and salinity in the near-tropical ocean: Observation from profiling floats. *Journal of Geophysical Research: Oceans*, **119**, 7433–7448, doi:10.1002/2014JC010112.

Anderson, S. P. and R. A. Weller, 1996: Surface buoyancy forcing and the mixed layer of the western Pacific warm pool: Observation and 1D model results. *Journal of Climate*, **9**, 3056–3085.

Asher, W. E., A. T. Jessup, R. Branch, and D. Clark, 2014: Observation of rain-induced near-surface salinity anomalies. *Journal of Geophysical Research: Oceans*, **119**, 5483–5500, doi:10.1002/2014JC009954.

Baethgen, W. E., M. Carriquiry, and C. Ropelewski, 2009: Tilting the odds in maize yields. *Bulletin of the American Meteorological Society*, 179–183, doi:10.1175/2008BAMS2429.1.

Batchelor, G. K., 1959: Structure variation of convected quantities like temperature in turbulent fluid. *Fluid Mechanics*, **5**, 113–133, doi:10.1017/S002211205900009X.

Bond, N. A. and G. A. Vecchi, 2003: The influence of the Madden-Julian Oscillation on precipitation in Oregon and Washington. *Weather and Forecasting*, **18**, 600–613.

Brainerd, K. E. and M. C. Gregg, 1993a: Diurnal restratification and turbulence in the oceanic surface mixed layer 1. Observations. *Journal of Geophysical Research*, **98**, 22645–22656.

— 1993b: Diurnal restratification and turbulence in the oceanic surface mixed layer 2. Modeling. *Journal of Geophysical Research*, **98**, 22657–22664.

Callaghan, A. H., B. Ward, and J. Vialard, 2014: Influence of surface forcing on near-surface and mixing layer turbulence in the tropical Indian Ocean. *Deep-Sea Research I*, 107–123, doi:10.1016/j.dsr.2014.08.009.

Cantero, M. I., S. Balachandar, and M. H. Garcia, 2007: High-resolution simulation of cylindrical density currents. *Journal of Fluid Mechanics*, **590**, 437–69, doi:10.1017/S002212007008166.

Cantero, M. I., S. Balachandar, M. H. Garcia, and J. P. Ferry, 2006: Direct numerical simulations of planar and cylindrical density currents. *Journal of Applied Mechanics*, **73**, 923–930, doi:10.1115/1.2173671.

Cronin, M. F. and M. J. McPhaden, 1999: Diurnal cycle of rainfall and surface salinity in the western Pacific warm pool. *Geophysical Research Letters*, **26**, 3465–3468.

— 2002: Barrier layer formation during westerly wind bursts. *Journal of Geophysical Research*, **107**, doi:10.1029/2001JC001171.

Dake, J. M. K. and D. R. F. Harleman, 1969: Thermal stratification in lakes: Analytical and laboratory studies. *Water Resources Research*, **5**, 484–495.

Dewar, R. E., 2003: Rainfall variability and subsistence systems in southeast Asia and the western Pacific. *Current Anthropology*, **44**, 369–388.

Dillon, T. M. and D. R. Caldwell, 1980: The Batchelor spectrum and dissipation in the upper ocean. *Journal of Geophysical Research*, **85**, 1910–1916.

Donald, A., H. Meinke, B. Power, A. de H. N. Maia, M. C. Wheeler, N. White, R. C. Stone, and J. Ribbe, 2006: Near-global impact of the Madden-Julian Oscillation on rainfall. *Geophysical Research Letters*, **33**, L09704, doi:10.1029/2005GL025155.

Fairall, C. W., E. F. Bradley, J. S. Godfrey, G. A. Wick, J. B. Edson, and G. S. Young, 1996a: Cool-skin and warm-layer effects on sea surface temperature. *Journal of Geophysical Research*, **101**, 1295–1308.

Fairall, C. W., E. F. Bradley, J. E. Hare, A. A. Grachev, and J. B. Edson, 2003: Bulk parameterization of air-sea fluxes: updates and verification for the COARE algorithm. *Journal of Climate*, **16**, 571–591.

Fairall, C. W., E. F. Bradley, D. P. Rogers, J. B. Edson, and G. S. Young, 1996b: Bulk parameterization of air-sea fluxes for tropical ocean-global atmoshpere coupled-ocean atmosphere response experiment. *Journal of Geophysical Research*, **101**, 3747–3764.

Giannini, A., J. C. H. Chiang, M. A. Cane, Y. Kushnir, and R. Seager, 2001: The ENSO teleconnection to the tropical Atlantic Ocean: Contributions of the remote and local ssts to rainfall variability in the tropical Americas. *Journal of Climate*, **14**, 4530–4544.

Gottschalck, J., P. E. Roundy, C. J. S. III, A. Vintzileos, and C. Zhang, 2013: Large-scale atmospheric and oceanic conditions during the 2011-12 DYNAMO field campaign. *Monthly Weather Review*, **141**, 4173–4196.

Hacker, J., P. Linden, and S. Dalziel, 1996: Mixing in lock-release gravity currents. *Dynamics of Atmospheres and Oceans*, **24**, 183–195.

Hallworth, M. A., J. C. Phillips, H. E. Huppert, and R. S. J. Sparks, 1993: Entrainment in turbulent gravity currents. *Nature*, **362**, 829–831.

Hazel, P., 1972: Numerical studies of the stability of inviscid stratified shear flow. *Journal of Fluid Mechanics*, **51**, 39–61.

Henocq, C., J. Boutin, F. Pettitcolin, G. Reverdin, S. Arnault, and P. Lattes, 2010: Vertical variability and near-surface salinity in the tropics: Consequences for L-Band

radiometer calibration and validation. *Journal of Atmospheric and Oceanic Technology*, **27**, 192–209, doi:10.1175/2009JTECHO670.1.

Hogg, A., M. A. Hallworth, and H. E. Huppert, 2005: On gravity currents driven by constant fluxes of saline and particle laden fluid in the presence of a uniform flow. *J. Fluid Mech.*, **539**, 349–385, doi:10.1017/S002211200500546X.

Katsaros, K. B., L. A. McMurdie, R. J. Lind, and J. E. DeVault, 1985: Albedo of a water surface, spectral variation, effects of atmospheric transmittance, sun angle and wind speed. *Journal of Geophysical Research*, **90**, 7313–7321.

Kudryavtsev, V. N. and A. V. Soloviev, 1990: Slippery near-surface layer of the ocean arising due to daytime solar heating. *Journal of Physical Oceanography*, **20**, 617–628.

Lewis, M. R., M.-E. Carr, G. C. Feldman, W. Esaias, and C. McClain, 1990: Influence of the penetrating solar radiation on the heat budget of the equatorial Pacific Ocean. *Nature*, **347**, 543–545.

Lombardo, C. P. and M. C. Gregg, 1989: Similarity scaling of viscous and thermal dissipation in a convecting surface boundary layer. *Journal of Geophysical Research*, **94**, 6273–6284.

Lukas, R. and E. Lindstrom, 1991: The mixed layer of the western equator pacific ocean. *Journal of Geophysical Research*, **96**, 3343–3357.

Madden, R. A. and P. R. Julian, 1971: Detection of a 40-50 day oscillation in the zonal wind in the tropical Pacific. *Journal of the Atmospheric Sciences*, **28**, 702–708.

— 1972: Description of global-scale circulation cells in the tropics with a 40-50 day period. *Journal of the Atmospheric Sciences*, **29**, 1109–1123.

Matthews, A. J., D. B. Baranowski, K. J. Heywood, P. J. Flatau, and S. Schmidtko, 2014: The surface diurnal warm layer in the Indian ocean during CINDY/DYNAMO. *Journal of Climate*, doi:10.1175/JCLI-D-14-00222.1.

McPhaden, M. J., S. E. Zebiak, and M. H. Glantz, 2006: ENSO as an integrating concept in Earth science. *Science*, **314**, 1740–1745, doi:10.1126/science.1132588.

Morton, J. F., 2007: The impact of climate change on smallholder and subsistence agriculture. *Proceedings of the National Academy of Sciences of the United States of America*, **104**, 19680–19685.

Moum, J. N., 1990: Profiler measurements of vertical velocity fluctuations in the ocean. *Journal of Atmospheric and Oceanic Technology*, **7**, 323–333.

Moum, J. N., M. C. Gregg, R. Lien, and M. E. Carr, 1995: Comparison of turbulence kinetic energy dissipation rate estimates from two ocean microstructure profilers. *Journal of Atmospheric and Oceanic Technology*, **12**, 346–366.

Moum, J. N., J. D. Nash, and W. D. Smyth, 2011: Narrowband oscillations in the upper equatorial ocean. part I: Interpretation as shear instabilities. *Journal of Physical Oceanography*, **41**, 397–411, doi:10.1175/2010JPO4450.1.

Moum, J. N., S. P. D. Szoeke, W. D. Smyth, J. B. Edson, H. L. DeWitt, A. J. Moulin, E. J. Thomson, C. J. Zappa, S. A. Rutledge, R. H. Johnson, and C. W. Fairall, 2014: Air-sea interactions from westerly wind bursts during the november 2011 MJO in the Indian Ocean. *Bulletin of the American Meteorological Society*, 1185–1199, doi:10.1175/BAMS-D-12-00225.1.

Noh, Y., 1996: Dynamics of diurnal thermocline formation in the oceanic mixed layer. *Journal of Physical Oceanography*, 2183–2195.

Ohlmann, J. C., D. A. Siegel, and C. D. Mobley, 2000: Ocean radiant heating. part I: Optical influences. *Journal of Physical Oceanography*, **30**, 1833–1848.

Osborn, T. R., 1980: Estimates of the local rate of vertical diffusion from dissipation measurements. *Journal of Physical Oceanography*, **10**, 83–89.

Osborn, T. R. and C. S. Cox, 1972: Oceanic fine structure. *Geophysical Fluid Dynamics*, **3**, 321–345.

Patterson, M. D., J. E. Simpson, and S. B. Dalziel, 2006: Vortical motion in the head of an axisymmetric gravity current. *Physics of Fluids*, 046601.

Payne, R. E., 1972: Albedo of the sea surface. *Journal of the Atmospheric Sciences*, **29**, 959–970.

Price, J. F., 1979: Observation of a rain-formed mixed layer. *Journal of Physical Oceanography*, **9**, 643–649.

Price, J. F., R. A. Weller, and R. Pinkel, 1986: Diurnal cycling: Observations and model of the upper ocean response to diurnal heating, cooling, and wind mixing. *Journal of Geophysical Research*, **91**, 8411–8427.

Reverdin, G., S. Morisset, J. Boutin, and N. Martin, 2012: Rain-induced variability of near sea-surface T and S from drifter data. *Journal of Geophysical Research*, **117**, doi:10.1029/2011JC007549.

Richardson, L. F., 1920: The supply of energy from and to atmospheric eddies. *Proceedings of the Royal Society of London*, **97**, 354–373.

Rodó, X. and F. A. Comín, 2000: Links between large-scale anomalies, rainfall and wine quality in the Iberian Peninsula during the last three decades. *Global Change Biology*, **6**, 267–273.

Saji, N. H., B. N. Goswami, P. N. Vinayachandran, and T. Yamagata, 1999: A dipole mode in the tropical Indian Ocean. *Nature*, **401**, 360–363.

Schott, F. A. and J. P. McCreary, 2001: The monsoon circulation of the Indian Ocean. *Progress in Oceanography*, **51**, 1–123.

Seo, H., S.-P. Xie, R. Murtugudde, M. Jochum, and A. J. Miller, 2009: Seasonal effects of Indian Ocean freshwater forcing in a regional coupled model. *Journal of Climate*, **22**, 6577–6596, doi:10.1175/2009JCLI2990.1.

Simpson, J. E., 1982: Gravity currents in the laboratory, atmosphere, and ocean. *Ann. Rev. Fluid Mech.*, **14**, 213–234.

— 1997: *Gravity currents in the environment and the laboratory*. Cambridge University Press.

Simpson, J. J. and T. D. Dickey, 1981: Alternative parameterization of downward irradiance and their dynamics significance. *Journal of Physical Oceanography*, **11**, 876–882.

Smyth, W. D., J. N. Moum, L. Li, and S. A. Thorpe, 2013: Diurnal shear instabilities, the decent of the surface shear layer, and the deep cycle of equatorial turbulence. *Journal of Physical Oceanography*, **43**, 2432–2455.

Smyth, W. D., P. Zavialov, and J. N. Moum, 1997: Decay of turbulence in the upper ocean following sudden isolation from surface forcing. *Journal of Physical Oceanography*, **27**, 810–822.

Soloviev, A. and R. Lukas, 1997: Sharp frontal interfaces in the near-surface layer of the ocean in the western equatorial Pacific Warm Pool. *Journal of Physical Oceanography*, **27**, 999–1017.

— 2006: *The Near-Surface Layer of the Ocean*. Springer.

Soloviev, A., R. Lukas, and H. Matsuura, 2002: Sharp frontal interfaces in the near-surface layer of the tropical ocean. *Journal of Marine Systems*, **37**, 47–68.

Soloviev, A. V., S. Matt, and A. Fujimura, 2015: Three-dimensional dynamics of freshwater lenses in the ocean's near-surface layer. *Oceanography*, **28**, 142–149, doi:10.5670/oceanog.2015.14.

Sreenivasan, K. R., 1996: The passive scalar spectrum and the Obukhov-Corrsin constant. *Physics of Fluids*, **8**, 189–196.

Stommel, H., K. Saunders, W. Simmons, and J. Cooper, 1969: Observations of the diurnal thermocline. *Deep-Sea Research*, **16**, 269–284.

Stommel, H. M., 1993: An ocean regulating mechanism for determining the thermohaline structure of the oceanic mixed layer. *Journal of Physical Oceanography*, **23**, 142–148.

Thorpe, S. A., 1978: The near-surface mixing layer in stable heating conditions. *Journal of Geophysical Research*, **83**, 2875–2885.

Thorpe, S. A., M. Curé, and M. White, 1991: The skewness of temperature derivatives in oceanic boundary layers. *Journal of Physical Oceanography*, **21**, 428–433.

Thorpe, S. A. and T. R. Osborn, 2005: Skewness of spatial gradients of turbulent dissipation rate in the mixed layer. *Journal of Physical Oceanography*, 2299–2303.

Thorpe, S. A., T. R. Osborn, J. F. E. Jackson, A. J. Hall, and R. G. Lueck, 2003: Measurements of turbulence in the upper-ocean mixing layer using autosub. *Journal of Physical O*, **33**, 122–145.

Ungarish, M., 2009: The propagation of high-Reynolds-number non-Boussinesq gravity currents in axisymmetric geometry. *Journal of Fluid Mechanics*, **643**, 267–277, doi:10.1017/S0022112009992527.

Ungarish, M. and T. Zemach, 2005: On the slumping of high-Reynolds number gravity currents in two-dimensional and axisymmetric configurations. *European Journal of Mechanics B / Fluids*, **24**, 71–90, doi:10.1016/j.euromechflu.2004.05.006.

Vinayachandran, P. N., P. A. Francis, and S. A. Rao, 2009: Indian Ocean Dipole: Processes and impacts. *Current Trends in Science*, 569–589.

Wang, B. and X. Xie, 1998: Coupled modes of the warm pool climate system. part I: The role of air-sea interaction in maintaining Madden-Julian oscillation. *Journal of Climate*, **11**, 2116–2135.

Wijesekera, H. W. and M. C. Gregg, 1996: Surface layer response to weak wind, westerly bursts, and rain squalls in the Western Pacific warm pool. *Journal of Geophysical Research*, **101**, 977–997.

Wijesekera, H. W., C. . A. Paulson, and A. Huyer, 1999: The effect of rainfall on the sea surface layer during a westerly wind burst in the western equatorial Pacific. *Journal of Physical Oceanography*, **29**, 612–632, doi:10.1175/1520-0485(1999)029¡0612:TEOROT¿2.0CO;2.

Wijesekera, H. W., C. A. Paulson, and E. D. Skyllingstad, 2003: Modeling the evolution of a fresh sea surface anomaly produced by tropical rainfall. *Journal of Geophysical Research*, **108**, doi:10.1029/2002JC001408.

— 2004: Scaled temperature spectrum in the unstable oceanic surface layer. *Journal of Geophysical Research*, **109**, doi:10.1029/2003JC002066.

Woods, J. D., 1968: Diurnal behaviour of the summer thermocline off Malta. *Deutsche Hydrographische Zeitschrift*.

Wyrtki, K., 1973: An equatorial jet in the Indian Ocean. *Science*, **181**, 262–264, doi:10.1126/science.181.4096.262, article behind paywall.

Yoneyama, K., C. Zhang, and C. N. Long, 2013: Tracking pulses of the Madden-Julian oscillation. *Bulletin of the American Meteorological Society*, **94**, 1871–1981.

Zhang, C., 2005: Madden-Julian oscillation. *Reviews of Geophysics*, **43**, doi:10.1029/2004RG000158.

— 2013: Madden-Julian oscillation, bridging weather and climate. *Bulletin of the American Meteorological Society*, 1849–1870, doi:10.1175/BAMS-D-12-00026.1.

Zhang, Y. and J. N. Moum, 2010: Inertial-convective subrange estimates of thermal variance dissipation rate from moored temperature measurements. *Journal of Atmospheric and Oceanic Technology*, **27**, 1950–1959.